

**Possible Seismic Effects of Geochemical  
Processes of Injection of Carbon Dioxide in  
Carbonate Reservoirs.**

Master Thesis

**Helene Olafsen Sjøstad**



Department of Earth Science

University of Bergen

Bergen 2017



## **Abstract**

The seismic effect of geochemical reactions caused by rock-fluid interactions have been investigated throughout this thesis. Seismic attributes can provide valuable information about rock properties. As a result, rock physics models are important to link geological and seismic parameters.

Traditional fluid substitution models only consider the rock's response to variations in pore fluid. However, fabric alterations are not evaluated. Carbonate rocks hold a rock fabric highly prone to geochemically induced alterations. Research on revealing possible geochemical effects from CO<sub>2</sub> injections in carbonates, display a variety of textural alterations following rock-fluid interaction. As porosity and pore-shape affect the seismic properties, alterations in the rock fabric may induce large variations in the seismic response.

By performing rock physics modelling, the effect of various geochemical processes has been evaluated. Fluid substitution models display the effect of pore fluids on the seismic properties of a porous reservoir. Based on experimental research, scenarios describing possible fabric alterations following rock-fluid interactions are defined. The results reveal that fabric alterations mainly occur in the pore space, either altering the pore volume or pore geometry.

Trough implementation of forward rock physics modelling, the effects of pore geometry and pore volume on the seismic properties are investigated. The variations in seismic velocities and elastic properties are larger than those estimated when considering only the fluid effects. In addition, forward seismic modeling reveals the effect of fabric alterations on the amplitude versus incident-angle response. Evaluations of the results show that the seismic effects of pore-shape are different than the effects of pore volume.

By including the effect of pore-pressure and compaction, mechanical deformation is incorporated into the final stage of the modelling. This effect has however not displayed significant alterations in the seismic response of the carbonate rock model.

The work has demonstrated the importance of evaluating alterations occurring in the rock frame following rock-fluid interactions, in addition to the effect of fluids.





## **Acknowledgements**

First of all, I would like to give a special thanks to my supervisor Tor Arne Johansen for guidance throughout the course of this thesis. Your input has been greatly appreciated.

I wish to express my gratitude to my co-supervisor Erling Hugo Jensen and Åsmund Drotning for providing the MATLAB scripts used in this thesis. I also wish to thank you both for your guidance and motivation over the last year. Your help and positive attitude have been important to me.

To my friends and my boyfriend – these five years would not have not have been the same without you. Thank you for making my time as a student in Bergen so much fun!

Finally, I would like to thank my family for always supporting and guiding me.



# Table of Content

<b>1</b>	<b>Introduction.....</b>	<b>1</b>
1.1	Motivation.....	1
1.2	Objectives .....	2
1.3	Outline of Thesis.....	2
<b>2</b>	<b>Geology of Carbonate Rocks.....</b>	<b>5</b>
2.1	Carbonate Rocks .....	5
2.2	Depositional Environments.....	7
2.3	Carbonate Rock Fabric .....	11
2.4	Summary .....	15
<b>3</b>	<b>Rock Physics Modelling and Seismic Data Analysis.....</b>	<b>17</b>
3.1	Seismic Velocities.....	17
3.2	Seismic Reflections.....	18
3.3	Elastic Moduli.....	18
3.4	Rock Physics Models.....	21
3.5	Factors Controlling the Seismic Velocity .....	29
3.6	Seismic Data and Seismic Analysis.....	30
3.7	The Physical Properties of CO <sub>2</sub> .....	35
3.8	Summary .....	40
<b>4</b>	<b>Geochemical Alterations in Carbonate Rocks .....</b>	<b>41</b>
4.1	Carbonate Reactivity.....	41
4.2	Geochemically Induced Alterations in Rock Fabric .....	42
4.3	Dissolution of Carbonate Minerals .....	44
4.4	Precipitation of Carbonate Minerals .....	47
4.5	Summary .....	48
<b>5</b>	<b>Data Calibration and Modelling Methods.....</b>	<b>51</b>
5.1	Data Preparations .....	51
5.2	Modelling the Effects of Geochemical Interactions .....	55
5.3	Amplitude Versus Angle Modelling.....	58
5.4	Applicability of the Various Rock Physics Models.....	59
<b>6</b>	<b>Results and Analysis .....</b>	<b>61</b>
6.1	The Effect of Porosity, Pore Shape and Saturation on the Seismic Properties.....	61
6.2	Scenario Zero: The Effect of Fluid Substitution.....	62
6.3	Scenario One: The Effect of Altered Pore Geometries.....	71
6.4	Scenario Two: The Effect of Increased Porosity .....	83
6.5	Scenario Three: The Effect of Reduced Porosity .....	95
<b>7</b>	<b>Discussion .....</b>	<b>107</b>
7.1	Saturation Effects on Seismic Properties.....	107
7.2	Effect of Porosity and Pore Shape on Seismic Properties .....	107
7.3	Compaction Effects on the Seismic Properties.....	109
7.4	Amplitude Versus Angle Response .....	110
7.5	Wavelet Effect on Synthetic Seismic Data .....	112
7.6	Reliability of the Results.....	113

<b>8</b>	<b>Conclusions.....</b>	<b>115</b>
8.1	Carbonate Rocks.....	115
8.2	Pore Fluid.....	115
8.3	Pore Geometry and Porosity.....	115
8.4	Pore-Pressure and Compaction.....	115
8.5	The Wavelet Effect.....	116
8.6	Further Work.....	116
<b>9</b>	<b>References.....</b>	<b>117</b>
<b>Appendix A.....</b>		<b>123</b>
	DEM: definition of $P^*$ and $Q^*$ .....	123
	CCT: definition of $S_n$ and $S_\tau$ .....	123

# 1 Introduction

## 1.1 Motivation

With a constantly growing population and increasing energy demand, the consumption of oil and coal is expected to increase until 2040 (IEA, 2016). Burning of fossil fuels is believed to be one of the main sources of atmospheric CO<sub>2</sub> (Lumley, 2010). Anthropogenic emissions of greenhouse gasses, such as CO<sub>2</sub>, enhance the natural greenhouse effect, increasing the average temperature on Earth (Gunter et al., 1997). Over the last decades, concerns regarding the long term effects of this global warming have been raised.

Subsurface sequestration of CO<sub>2</sub> has been proposed as a possible solution to the future efforts of reducing the concentration of greenhouse gasses in the atmosphere (Metz et al., 2005). Secure storage is dependent on detecting possible leakage from the injected fields, obtaining long term disposal. Seismic monitoring may as a result become increasingly important. 4D seismic surveys are often applied to monitor the variations in pore fluids and saturation in oil and gas reservoirs (Lumley, 2010). This technique can be transferred to monitor subsurface CO<sub>2</sub> injections. Rock physics modelling provide useful information about the expected seismic response of the injected reservoir, and can thus serve as an additional tool for fluid detection. However, conventional fluid substitution modelling, such as Gassmann, only consider the saturation effects and might thus hold certain limitations (Berryman, 1999).

Time-lapse monitoring of CO<sub>2</sub> injections in subsurface reservoirs reveals variations in P- and S-wave velocities that are too large to be explained by Gassmann alone (Grombacher et al., 2012; McCrank and Lawton, 2009). Experimental data demonstrate a highly chemically reactive surface when carbonate reservoirs are exposed to CO<sub>2</sub>. These geochemical reactions can induce rapid alterations in the rock texture that cannot be accounted for using traditional fluid substitution models (Grombacher et al., 2012; Vanorio et al., 2011; Vanorio, 2015). The fabric modifications may affect the seismic response of the fluid saturated reservoir. If not considered, consequences as misinterpretations of the fluid location or saturation can occur. For this reason, it is of interest to investigate whether geochemical effects will affect the seismic signature of a carbonate reservoir exposed to CO<sub>2</sub> injections.

## 1.2 Objectives

The aim of this study is to address the possible time-lapse seismic response following CO<sub>2</sub> injections in carbonate reservoirs. Based on experimental studies, various plausible alterations in the rock fabric as a response to CO<sub>2</sub> injections are evaluated (Grombacher et al., 2012; Vanorio, 2015; Vanorio et al., 2011).

Next, four different scenarios will be created based on the presented experimental results. Using this information, a synthetic carbonate rock model is generated for each scenario. The model is based on the provided North Sea well data of a carbonate reservoir. Fluid substitution will be modelled using the Gassmann equation, whilst the altered rock frame is modelled using the Kite model (Avseth et al., 2014).

The goal is to understand how the effective rock properties are altered following rock-fluid interactions, and how these alterations are expected to affect the seismic signature of the rock. In addition to evaluating the elastic properties and seismic velocities of the modelled reservoir, tools as amplitude-versus-angle and rock physics templates will be utilized.

### 1.2.1 Programs Used for Modelling and Visualization

Hampson-Russel software from CGGVeritas will be applied to create the AVA models and plots. The rest of the data is modelled using MATLAB, where all applied scripts are provided by Erling Hugo Jensen and Åsmund Drottning (Rock Physics Technologies). The modelling is based on these scripts, where pre-defined input parameters describing the rock and pore fluid will be needed.

## 1.3 Outline of Thesis

**Chapter 1:** provides the motivation and objectives of this thesis.

**Chapter 2:** introduce theory on carbonate sediments and rocks.

**Chapter 3:** introduces applied rock physics theories, a brief evaluation of their applicability to carbonate rocks and an overview of the physical properties of CO<sub>2</sub>. These topics are important in relation to seismic modelling of the reservoirs.

**Chapter 4:** present the geochemical alterations occurring in the rock frame as a result of rock-fluid interaction.

**Chapter 5:** present the methods and data that have been applied in this thesis.

**Chapter 6:** presents the modelling results

**Chapter 7:** provides the discussion section. Here the results presented in chapter 6 will be compared to theory presented in the earlier chapters.

**Chapter 8:** gives the final conclusions of the modelling results.





## 2 Geology of Carbonate Rocks

Carbonate rocks distinguish themselves from siliciclastic rocks by their depositional setting. While siliciclastic sediments are well sorted and re-worked through transportation mechanisms, carbonate sediments are formed *in-situ*.

Carbonate sediments are formed through organic or geochemical processes, and hold large textural variations compared to siliciclastic rocks. This chapter will provide a brief introduction to carbonate rocks, describing the deposition, preservation and variations in the rock fabric itself.

### 2.1 Carbonate Rocks

#### 2.1.1 Formation of Carbonate Sediments

Over 90% of the world's carbonate deposits are biological in origin, and form under marine conditions (Moore, 2001). The deposits are composed of skeletal material from marine organisms and pelagic material (Palaz and Marfurt, 1997).

Carbonate production is largely controlled by organisms extracting calcium carbonate ( $\text{CaCO}_3$ ) from sea water, to build shells and skeletal structures. Through biological activities such as feeding or bioturbation, skeletal fragments may be deposited as carbonate sediments (Boggs Jr., 2014).

$\text{CaCO}_3$  can precipitate in seawater through biological processes, or through inorganic precipitation. Processes as algal photosynthesizes are important for  $\text{CaCO}_3$  precipitation. In general, the algal  $\text{CaCO}_3$  production is largest at shallow depths of 10-15 meters (Wilson, 1975).

In addition to depth, the productivity of carbonate sediments is dependent on geotectonic and climate. Geotectonic controls the content of siliciclastic sediments in the carbonate environment (Tucker and Wright, 2009). The turbidity caused by clay and silt in suspension constrains the production of carbonate sediments by limiting the penetration of light, which restrains growth of carbonate platforms or reef development (Wilson, 1975). In addition to creating barriers for siliciclastic sediments, geotectonic and climate are important controlling factors of the sea level. Together they have proven to be an important factor controlling carbonate production.

As carbonate sediments are deposited where they are created, carbonate rocks are formed *in-situ* due to cementation and binding of the carbonate sediments. This is a large

contrast to deposition of siliciclastic sediments, which is controlled by sediment transportation and water energy. The local deposition of carbonate sediments results in a large heterogeneity of sediment grains, as the sediments are not sorted by water currents or waves.

### 2.1.2 Mineralogy of Carbonate Rocks

Carbonates, described by the formula  $MCO_3$ , are composed of metallic cations ( $M^{2+}$ ) and the carbonate anion ( $CO_3^{2-}$ ). The carbonate group is a polyatomic anion with strong polar covalent binding, and spans the space with a trigonal geometry (Figure 2.1)(Rayner-Canham and Overton, 2010).

When exposed to acidic solutions, the carbonate group will break down. For this reason, carbonate rocks are highly prone to chemically induced alterations. This topic will be discussed in chapter 4.

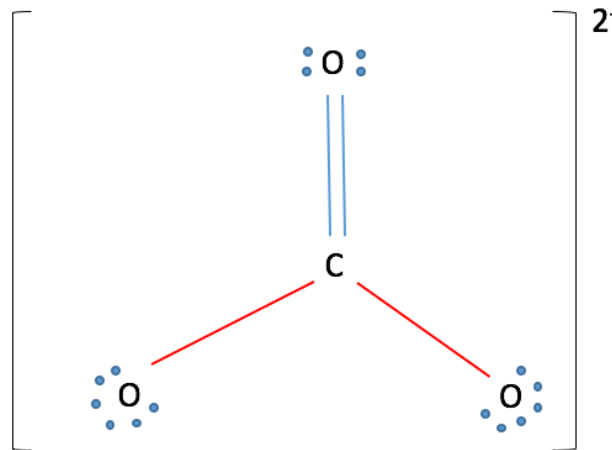


**Figure 2.1.** The figure is showing the carbonate ion. Modified from Rayner-Canham and Overton, (2010).

The most common carbonate minerals are calcite carbonate ( $CaCO_3$ ), dolomite ( $CaMg(CO_3)_2$ ) and aragonite ( $CaCO_3$ ). The chemical stability of the carbonate minerals is dependent on the crystal lattice.

Calcite and dolomite have a rhombohedral crystal system, but structural differences induce dissimilarities between the two. Calcite is the most chemically stable mineral, consisting of alternating layers of Ca-atoms and  $CO_3$  groups, where each  $CO_3$  group in one layer has one common orientation (Tucker and Wright, 2009). The solubility of calcium carbonate depends on temperature, pH and carbon dioxide content in the sea water (Ahr, 2008)

The dolomite structure is ideally described by substitution of Mg atoms into the Ca layers of the calcite crystal structure (Tucker and Wright, 2009). Ideal dolomite consist of equal

ratios of  $\text{CaCO}_3$  and  $\text{MgCO}_3$  (Moore, 2001). However, the substitution of Ca by Mg induces a change in the strength of the atom bonds in dolomite, leading to a lower degree of inner symmetry. The small size of the magnesium ions compared to the calcium ions cause a change in the dolomite lattice, leading to decreased solubility (Ahr, 2008). If dolomite exist in ideal composition (equal ratios of  $\text{CaCO}_3$  and  $\text{MgCO}_3$ ), it is chemically stable over a wide range of pressure and temperatures (Moore, 2011).

Aragonite, although having the same composition as calcium carbonates, is 1.5 times more soluble and consist of an orthorhombic crystal system (Moore, 2001). Aragonite is common in modern carbonate deposits as it precipitates form seawater. However, due to the chemical instability of the mineral, aragonite dominated sediments will, over time, convert to calcium carbonates (Ahr, 2008).

## 2.2 Depositional Environments

### 2.2.1 Geographical Distribution and Preservation of Carbonate Sediments

The geographical distribution and preservation of carbonate sediments are largely controlled by water temperature, salinity, substrate and the presence of siliciclastic sediments. The carbonate production is most efficient in tropical waters, as carbonate producers thrive in these environments (Moore, 2001).

Carbonate sediments are generated along slopes, platforms or margins, and the deposits can extend for hundreds of km. Deposition is generally restricted to warm, shallow waters (Palaz and Marfurt, 1997). However, deep marine deposits of carbonate sediments can form in cold waters through settling of pelagic particles and shell remains. This occurs where the ocean floor lies above the carbonate compensation depth (CCD).

The carbonate compensation depth is defined as “*the water depth at which the rate of supply of calcium carbonate from the subsurface is equal to the rate of dissolution*” (Burton, 1998). The position of CCD changes in modern oceans, and thus control where deep ocean carbonates are deposited. Typically, the sea floor near mid ocean ridges lie above the CCD, leading to deposition and preservation of deep ocean carbonates. Figure 2.2 illustrates the global distribution of carbonate sediments.

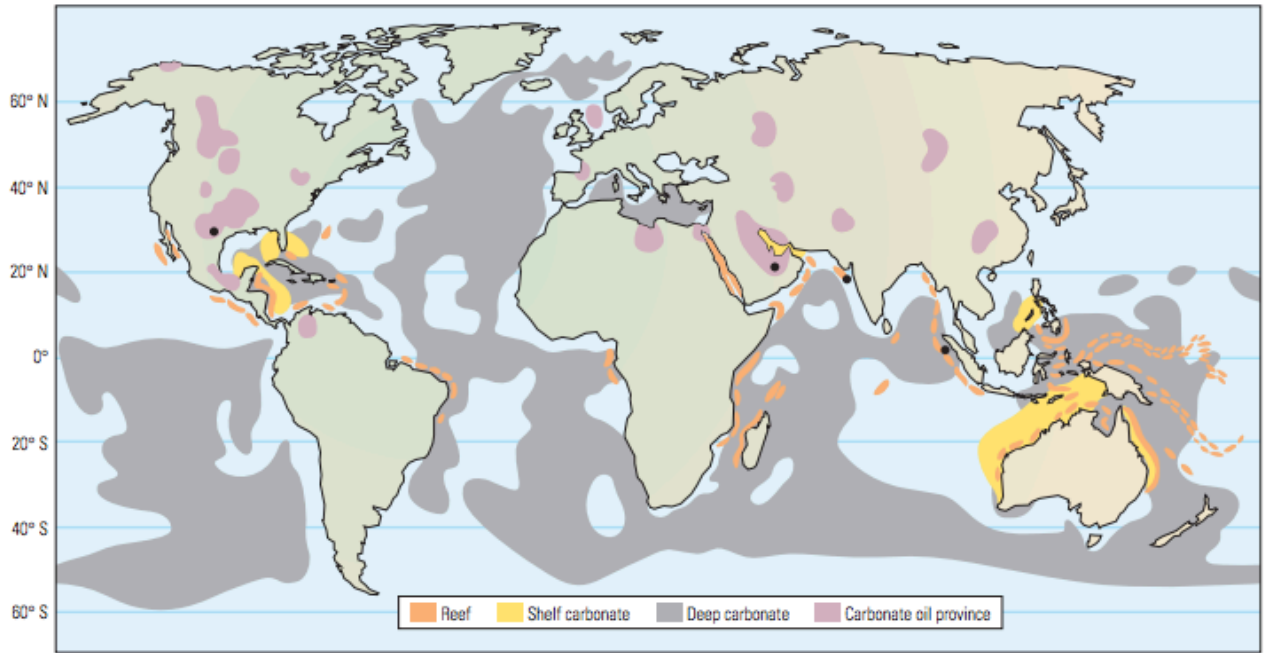


**Figure 2.2.** The figure is showing the global distribution of carbonate sediments (Akbar et al., 2000).

**2.2.2 Carbonate Facies (Wilson Rimmed Platform Model)**

Sedimentary facies is defined as the sum of the lithological and biological characteristics of a sedimentological deposit (Dercourt and Paquet, 1985). This means that each facies can be recognized as a lateral sequence of sediments with similar depositional environment, structural and biological characteristics. Wilson (1975) defined a rimmed platform facies model, characterizing depositional environments, textures and sedimentary structures. The facies model describes the depositional pattern of a platform with an abrupt shelf margin and gently sloping shelf (Wilson, 1975, 1997), as illustrated in Figure 2.3. The model is sub-divided into nine carbonate facies. A brief summary of the facies model will be described in this section:

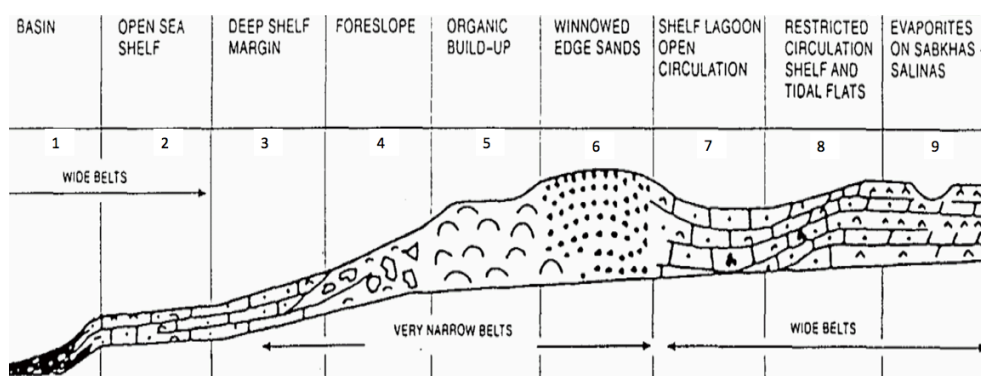


**Figure 2.3.** The figure illustrates the rimmed platform facies, presented by 1-9 by Wilson (1997).

### *1. Basin facies (starved or filled basin)*

Basin deposits are dominated by pelagic sediments that are deposited above CCD. The deposits are characterized by parallel lamina consisting of thin layers of lime mud interbedded with thicker layers of less compacted carbonates.

The sediments can contain large amounts of organic material, giving them good source rock potential. Due to the low permeability and porosity of the fine grained layers, basin sediments usually serve as good seals to petroleum reservoirs.

### *2. Shelf facies*

The shelf environment is characterized by water depth ranging from ten to a couple of hundred meters in depth. Due to normal water salinity and good current circulation, the fauna in this environment is varied. The water is generally well oxygenated.

The shelf facies are often characterized by fossiliferous limestone interbedded with marl. Due to the high organic concentration, the shelf deposits may have good source rock potential. As the porosity of these deposits generally are low, they rarely serve as good reservoirs.

### *3. Basin margin or deep shelf margin facies*

The deep shelf margin deposits usually consist of re-sedimented sediments, deposited by debris flow or turbidite currents. In addition, sediments formed directly in the water column above are deposited through pelagic rain. Texturally, the sediments vary between fine grained clay and coarser carbonate sediments. These deposits may contain reservoir permeability and porosity if large voids between clasts of debris flow only is partially cemented, or if preferential solution and dolomitization occurs.

### *4. Foreslope facies of carbonate platform*

Foreslope deposits have many of the same characteristics as deep shelf margin deposits, however foreslope sediments contain more fossils. The sediments are mostly deposited by gravitational forces, as the foreslope environment can be as steep as 30°. As a result, the layers are thick and irregular. Due to high porosity and good permeability, the foreslope deposits are good reservoirs.

### 5. *Organic reef of platform margin*

The ecologic character of reef deposits depends on the water energy, steepness of the slope and organic productivity. The deposits consist of large amounts of calcium carbonate framework. Initially organic reefs have high porosity, that may be enhanced in the meteoric regime and by dolomitization. As the reef framework is rigid, the structure is prone to fracture when stress is applied, increasing the porosities. When the pore space is not cemented or filled with sediments, organic reefs are good reservoirs.

### 6. *Winnowed platform edge sand*

The depositional setting of winnowed sediments are beaches, spits, barrier reefs or dune islands. The sediments are deposited as marginal sands. The environment is strongly affected by tidal currents, reflected in both the sedimentary structure and well sorted grains. The dominating structure is cross bedding of lime sand. The variations in grain size give extremely high porosities of 75-80%. However, due to tidal currents, the sediments are sorted, reducing the porosities to 40%. These sediments serve as good petroleum reservoirs, containing 45% of the world's hydrocarbon reservoirs.

### 7. *Open marine platform facies*

Depositional environments are located in open lagoons and bays behind the outer platform edge, with shallow water depths and normal water salinity. Due to the normal water salinity, the environment has a rich fauna, making burrows and trace fossils the dominant sedimentary texture. As the porosity and permeability is low, open marine facies rarely make good petroleum reservoirs.

### 8. *Facies of restricted circulation on marine platform*

The restricted circulation environment exists on the inner platform. Due to tidal dominated sedimentation, the sedimentary structures are dominated by tidal channels, levees, ponds or stromatolites. Good reservoirs can exist in the coarser parts of the channel deposits.

### 9. *Platform evaporite facies*

Evaporite facies develop in supratidal and inland ponds, in an evaporative climate. The environment is characterized by intense heat and aridity, with sporadic events of water flooding. The sedimentary facies is dominated by irregular laminated anhydrite and dolomite on salt flats.

The deposits lack biota, except stromatolite algae, and does not have source rock potential. Due to the low porosity and permeability, evaporite deposits form excellent seals.

## 2.3 Carbonate Rock Fabric

### 2.3.1 Diagenetic Processes

Due to the chemically unstable nature of carbonate sediments, carbonate rocks are subjected to diagenetic processes (Boggs Jr., 2014). Diagenesis is defined by Wilson (1997) as “*the low-temperature rock-fluid reactions under overburden load, excluding the higher temperature and pressure of metamorphism*”. The diagenetic processes lead to alterations in porosity, mineralogy and chemistry (Boggs Jr., 2014).

There are three regimes that may cause diagenetic alterations in carbonate rock fabric; shallow-marine, meteoric and post burial diagenesis. The marine and meteoric regime is on or near the surface, and is marked by the presence of pore fluids. The sub-surface regime is characterized by mixtures of marine-meteoric waters or complex basinal-derived brines (Moore, 2001). Figure 2.4 provides an illustration of the diagenetic environments.

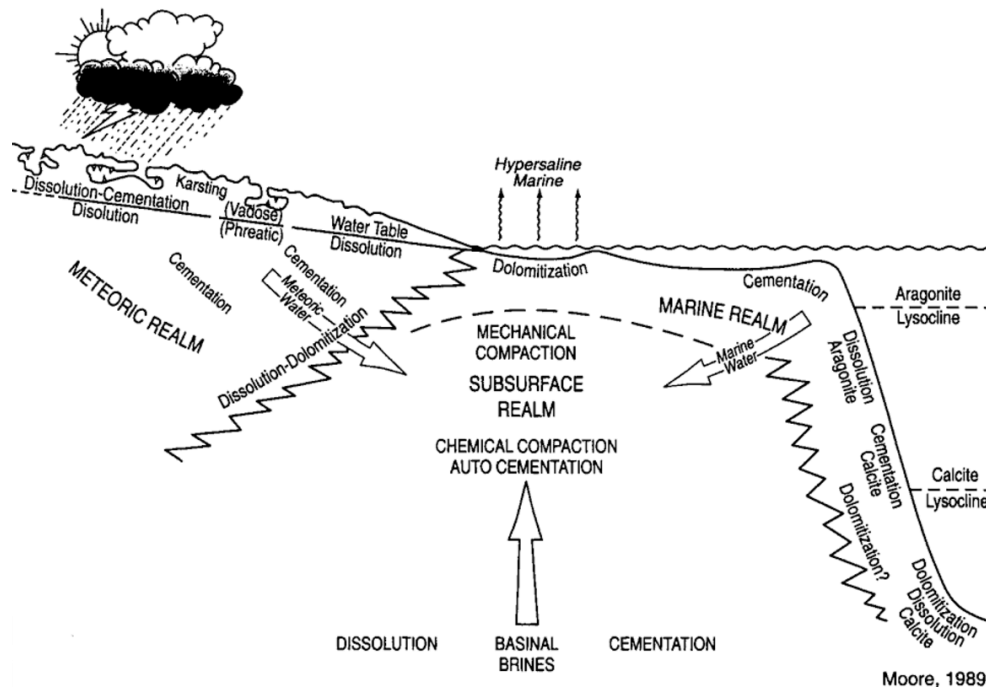


**Figure 2.4.** The figure is showing a diagram of the common diagenetic environments and diagenetic processes (Moore, 2001).

### ***The marine regime***

In the marine diagenetic regime, the alterations start in loose carbonate sediments, and continues down to the seafloor and shallow substrate (Wilson, 1997). Due to circulation of supersaturated water with respect to carbonate minerals, the marine environment is dominated by intensive porosity destruction (Moore, 2001).

The distribution of marine cementation is controlled by the amount of fluid circulating in the pore system, and is therefore dependent on permeability and depositional environment. When marine water is flushed through carbonate rocks, dolomitization may lead to the formation of secondary porosities (Moore, 2001).

### ***The meteoric regime***

The meteoric diagenetic regime is characterized by subaerial exposure and the presence of dilute waters that are undersaturated or supersaturated with carbonate minerals. Meteoric water tends to be highly acidic due to high concentrations of dissolved CO<sub>2</sub> in the circulating water. In the case where both aragonite and calcite is present in the meteoric water, dissolution of aragonite will lead the mineral system towards a more stable, less soluble calcite dominated phase. This process leads to supersaturation of calcium carbonate, and precipitation of calcite cement (Boggs Jr., 2014; Moore, 2001). As a result, both dissolution and precipitation are the main diagenetic processes in the meteoric regime (Boggs Jr., 2014).

### ***The subsurface regime***

The subsurface regime occurs after the sediments are buried. The environment is characterized by pore fluids composed of marine and meteoric water. Due to rock-water interaction, the circulating water tend to be supersaturated with carbonate minerals (Moore, 2001).

As pressure increases, carbonate grains are packed more tightly, and may deform by brittle deformation. The chemical compaction starts at burial depths of 200-1500 meters. Due to high pressure, the grains are dissolved at the grain contacts, resulting in cement formation through mineral precipitation. This process can form fine grained stylolite seams, that are characterized by fine clay minerals accumulating as carbonate minerals are dissolved. These seams of stylolites cause a significant loss in porosity and thinning of beds (Boggs Jr., 2014).

Secondary porosity can develop locally in the subsurface regime through thermal degradation of hydrocarbons, leaving the water undersaturated with respect to carbonate minerals. The process leads to dissolution, and porosity enhancement (Moore, 2001).



### 2.3.2 Carbonate Porosities

Carbonate rocks have a highly complex texture, due to the in-situ deposition of the sediments and the high chemical reactivity of the rock frame. Porosities and pore types can be characterized as primary and secondary, depending on when and how the pore space is created. Moore (2001) defines primary porosity as any porosity present at the time of depositional termination, and can form before or during sediment deposition. Secondary porosity is developed at a time after the sediments are deposited (Moore, 2001).

Due to the in-situ and biological origin of carbonate rocks, the pore systems are much more complex than for those of siliciclastics. The pore structures are further complicated as a result of the high chemical reactivity of carbonates and the formation of secondary porosities through diagenetic alterations (Wilson, 1997).

Choquette and Pray classified carbonate porosities based on fabric selectivity (Moore, 2001). The following description of carbonate porosities is based on the classification by Choquette and Pray from 1970 (Moore, 2001; Wang, 1997). Figure 2.5 provides an illustration of each pore type:

#### *Interparticle and intercrystalline porosities*

Intraparticle porosities occur between particles of any size, whereas intercrystalline porosities occur between crystals of approximately equal size. These porosities are generally primary of origin, and form at the time of deposition due to mud-free carbonate sediments. However, the formation of interparticle porosities can occasionally be of secondary origin (Moore, 2001).

#### *Moldic porosities*

Moldic porosities are created through selective solution of fragments in the carbonate rock, such as shells or grains of aragonite. Moldic pores usually have regular shape, and is of secondary origin.

#### *Intraparticle and intracrystalline porosities*

Intraparticle and intracrystalline porosities are pore space within grains, particles or crystals. These pore types are one of the fundamental differences between carbonate and siliciclastic porosities. Intraparticle/crystalline pores can be of secondary or primary origin. Secondary intraparticle/crystalline pores are created by solution and borings. Primary intraparticle/crystalline pores mostly occur as internal chambers within the constituents of carbonate rocks.

*Vuggy porosities*

Vuggy pores are classified as large (diameter  $> 1/6$  mm) pores of approximately equant size, with no fabric selectivity. Vugs are of secondary origin, and are usually formed by solution, occasionally due to enlargement of more fabric selective pores, such as molds.

*Channel porosities*

Channel porosities are defined by their elongated shape, and form through solution along fractures.

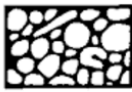


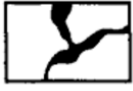
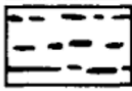
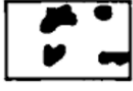





*Framework and fenestral porosities*

Framework porosities form within frame-builders such as corals or sponges, and are of primary origin. The pores tend to be filled with sediments during early reef development.

Fenestral porosities are defined as voids that are larger than the grain-supported openings. Fenestral pores are of secondary origin. They usually form due to decay of sediment covered algal mats, shrinking during dying and accumulation of gas or water pockets after deposition.

*Fracture porosities*

Fracture porosities are formed during fracturing of the rock. Due to the brittle nature of carbonate reservoirs, fractures are a common feature. In carbonate rocks, fractures are commonly filled with a variety of mineral species such as calcite and dolomite.

BASIC POROSITY TYPES								
FABRIC SELECTIVE		NOT FABRIC SELECTIVE						
PRIMARY		INTERPARTICLE	BP		FRACTURE	FR		
		INTRAPARTICLE	WP			CHANNEL*	CH	
		FENESTRAL	FE				VUG*	VUG
		SHELTER	SH					CAVERN*
		GROWTH-FRAMEWORK	GF			*Cavern applies to man-sized or larger pores of channel or vug shapes.		
SECONDARY		INTERCRYSTAL	BC					
		MOLDIC	MO					

**Figure 2.5.** The figure is displaying the various pore types in carbonate rocks (Moore, 2001).

## 2.4 Summary

The deposition of carbonate sediments is strongly dependent on climate and tectonic environment in the depositional area. As a result, the global distribution of carbonate deposits is mainly restricted to the southern hemisphere, although carbonate deposits can form in cold waters.

The origin of carbonate sediments and the in-situ sediment deposition leaves a highly complex rock, that consist of more irregularly shaped particles compared to those of a siliciclastic rock. Carbonates consist of a variety of porosities and pore sizes that contribute to the complexity of carbonate rocks. As a result of the mineralogical composition, carbonate rocks are highly prone to diagenetic alterations, leading to the formation of secondary porosities, or precipitation and porosity reduction. These diagenetic processes complicate the rock fabric further.



### 3 Rock Physics Modelling and Seismic Data Analysis

Carbonates have a more complex structure than siliciclastic rocks. As a result, not all rock physics models are applicable. Rock physics provides a link between the physical properties of a rock and their seismic response. The relationship between velocities and densities with the rock's elastic properties are established through such models.

Seismic data can provide valuable information of the subsurface. With additional data analysis tools based on rock physics models, the interpreter is able to distinguish between different lithologies or fluid saturation effects. In this chapter a brief introduction to some of the rock physics models is provided. In addition, some data analysis tools will be presented.

#### 3.1 Seismic Velocities

The seismic velocity describes the propagation of an elastic wave in an elastic medium. When assessing seismic velocities, P- and S-waves are considered.

P-waves are curl-free, meaning that the deformation caused by wave propagation through a medium is compressional. These compressional waves can travel through all materials. The P-wave velocity,  $v_p$ , is described by:

$$v_p = \sqrt{\frac{K + \frac{4}{3}\mu}{\rho}}, \quad (3.1)$$

where  $K$  is the bulk modulus and  $\mu$  is the shear modulus of the rock. The density  $\rho$ , is defined as the mass over total rock volume:

$$\rho = \frac{M}{V}, \quad (3.2)$$

where  $M$  is the rock mass and  $V$  is the rock volume.

S-waves are divergence-free, indicating that only rotation or shear take place. Shear waves only travel through solid material, meaning that there is no propagation of S-waves in fluids. The S-wave velocity,  $v_s$ , is described by:

$$v_s = \sqrt{\frac{\mu}{\rho}} \quad (3.3)$$

### 3.2 Seismic Reflections

Seismic reflections are caused by contrasts in acoustic impedance. The acoustic impedance ( $AI$ ) is defined as the product of seismic velocity ( $v$ ) and the density ( $\rho$ ) of the rock:

$$AI = \rho v. \quad (3.4)$$

Some of the seismic energy is reflected, whereas some is transmitted. The amplitude of the reflected wave is described by the reflection coefficient,  $R$ :

$$R = \frac{AI_2 - AI_1}{AI_2 + AI_1}, \quad (3.5)$$

where  $AI_1$  is the acoustic impedance of layer 1 and  $AI_2$  is the acoustic impedance of layer 2. Strong seismic reflections indicate large contrast between two layers; e.g. a hard rock overlying a softer layer

The amplitude of the transmitted wave is defined by the transmission coefficient,  $T$ . As the sum of the reflected and transmitted amplitude is equal to that of the incident wave, the transmission coefficient can be calculated by subtracting  $R$  from 1 (Castagna and Chopra, 2014):

$$T = 1 - R = \frac{2AI_1}{AI_2 + AI_1}. \quad (3.6)$$

Carbonate rocks are generally characterized by strong reflections in the seismic image. This is caused by the high velocity and density in carbonates. However, when overlain by another carbonate layer, the reflectivity between the two formations is relatively low (Palaz and Marfurt, 1997).

### 3.3 Elastic Moduli

The elastic moduli of a rock describe the rock's response to applied stress. The elastic moduli used in the equations for seismic velocities are bulk and shear modulus. Bulk modulus, or the

incompressibility, describes the medium's resistance to volume change when subjected to hydrostatic pressure (Figure 3.1a) (Kearey et al., 2002):

$$K = \frac{\text{volume stress } P}{\text{volume strain } \Delta V/V}, \quad (3.7)$$

where  $P$  is the applied hydrostatic pressure and  $\Delta V/V$  is the relative change in volume.

The shear modulus is defined as the ratio of shear stress to shear strain (Figure 3.1b) (Kearey et al., 2002):

$$\mu = \frac{\text{shear stress } \tau}{\text{shear strain } \tan\theta}, \quad (3.8)$$

where  $\tau$  is the applied shear stress and  $\theta$  is the angle of strain.

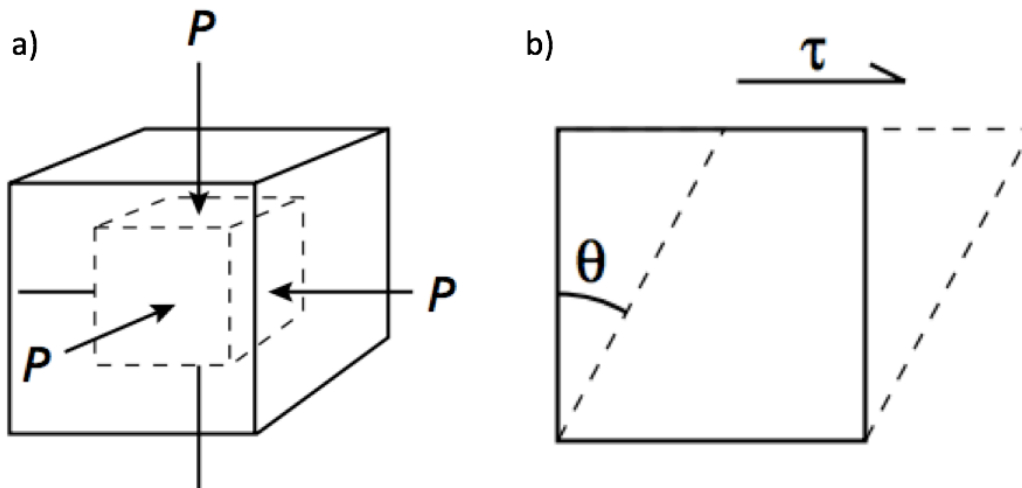


**Figure 3.1.** The figure is illustrating a) volume changes used to define the bulk modulus,  $K$ , and b) shear deformation used to describe the shear modulus,  $\mu$  (Kearey et al., 2002).

### 3.3.1 Elastic Moduli of a Multi-Constituent Material

Rocks are heterogeneous materials, consisting of more than one mineral phase. The elastic properties of an ideal rock are described using the classical approximation. Such a rock is statistically homogeneous, and the effective moduli is defined by Hooke's law (Guéguen and Palciauskas, 1994):

$$M^* = \frac{\bar{\sigma}}{\bar{\varepsilon}}, \quad (3.9)$$

where  $M^*$  is the effective elastic moduli, and  $\bar{\sigma}$  and  $\bar{\varepsilon}$  are the average stress and strain respectively.

In the case of a heterogeneous medium consisting of more than one phase, Hill's average gives a good approximation for the effective elastic moduli (Smith et al., 2003). Hill uses the average of Reuss and Voigt approximation to determine the effective elastic moduli. The Reuss model describes the elastic properties in the case of soft material composites, and refers to the *iso-stress* model. The model gives the ratio between average stress to the average strain when all constituents are assumed to have the same stress (Mavko et al., 2009). The effective elastic moduli are then described as:

$$M_R = \left[ \sum_{i=1}^n \frac{V_i}{M_i} \right]^{-1}, \quad (3.10)$$

where  $M_R$  the elastic modulus,  $V_i$  is the volume fraction of each constituent, and  $M_i$  is the elastic moduli of the individual phases.

The Voigt model describes the elastic properties in the case of stiff rock composites, and refers to the *iso-strain* model. This model gives the ratio between average stress to the average strain when all constituents are assumed to have the same strain (Mavko et al. 2009). The effective elastic moduli are then described as:

$$M_V = \sum_{i=1}^n V_i M_i, \quad (3.11)$$

where  $M_V$  is the elastic modulus,  $V_i$  is the volume fraction of each constituent, and  $M_i$  is the elastic moduli of the individual phases.

The Hill average thus calculates the arithmetic average of the upper Voigt, and the lower Reuss estimate. This translates into:



$$M_H = \frac{M_V + M_R}{2}, \quad (3.12)$$

where  $M_H$  is the Hill elastic modulus and  $M_V$  and  $M_R$  are the elastic moduli calculated using Voigt and Reuss, respectively.

### 3.4 Rock Physics Models

The seismic properties of a porous rock are affected by factors such as mineralogy, temperature, pressure, porosity, fluid saturation and pore shape. For this reason, it is often of interest to study the effect of variations in one or several of these parameters of the rock properties. These predictions may be obtained through theoretical models of the effective rock (Wang, 2001).

Having the appropriate rock physics model is a key element for time lapse seismic monitoring of the subsurface. Such models are useful in order to convert the detected changes in seismic properties into the properties of reservoir rocks (Mavko et al., 2015).

#### 3.4.1 Gassmann Model for Fluid Substitution

Gassmann's model for fluid substitution is commonly applied to estimate the fluid effect on the effective bulk modulus of a rock (Gassmann, 1951; Smith et al., 2003) :

$$K_{sat} = K_d + \frac{(1 - \frac{K_d}{K_s})^2}{\frac{\phi}{K_f} + \frac{1 - \phi}{K_s} - \frac{K_d}{K_s^2}}, \quad (3.13)$$

where  $K_{sat}$ ,  $K_d$ ,  $K_s$ ,  $K_f$  is the effective bulk moduli of the saturated, dry, solid frame and fluids respectively, and  $\phi$  is the porosity.

The equation relates the elastic moduli of the rock to its porosity and pore filling fluids. Equation 3.13 can be used when the dry rock modulus is measured. Commonly, the saturated bulk modulus is the one that is measured through seismic surveys. In this case, the dry rock properties can be calculated (Mavko et al., 2009):

$$K_d = \frac{K_{sat} \left( \frac{\phi K_s}{K_f} + 1 - \phi \right) - K_s}{\frac{\phi K_s}{K_f} + \frac{K_{sat}}{K_s} - 1 - \phi}. \quad (3.14)$$

When performing Gassmann modeling for fluid substitution, the effective shear modulus of the saturated rock is equal to the shear modulus of the dry rock (Berryman, 1999):

$$\mu_{sat} = \mu_{dry} , \quad (3.15)$$

where  $\mu_{sat}$  and  $\mu_{dry}$  is the saturated and dry shear moduli, respectively.

This follows Berryman's (1999) analysis of Gassmann results, and implies that there is no alteration in the shear modulus of the rock when fluid substitution is performed. By defining the saturated rock's density, the seismic velocities of a saturated rock can be obtained:

$$\rho_{sat} = \phi \rho_f + (1 - \phi) \rho_s , \quad (3.16)$$

where  $\rho_{sat}$ ,  $\rho_f$  and  $\rho_s$  are the densities for the saturated rock, the fluid and the solid, and  $\phi$  is the porosity. Hence, the seismic velocities for a saturated rock can be acquired:

$$v_{pSat} = \sqrt{\frac{K_{sat} + \frac{4}{3}\mu_{sat}}{\rho_{sat}}} , \quad (3.17)$$

$$v_{sSat} = \sqrt{\frac{\mu_{sat}}{\rho_{sat}}} . \quad (3.18)$$

### **Gassmann assumptions**

The derivation of Gassmann model is based on a set of assumptions (Adam et al., 2006; Castagna and Chopra, 2014; Mavko et al., 2009):

1. The rock is isotropic, homogeneous and saturated with one single fluid.
2. The pore fluids are homogeneously distributed within the rock.
3. The system is assumed to be closed, meaning there is no fluid flow in or out of the system.
4. The pores are connected.

5. The equations are only valid for low frequencies, so that the induced pore pressures are equilibrated throughout the pore space.
6. Gassmann model assumes that there is no interaction between the rock and the pore-fluid.

### **Gassmann and carbonate rocks**

Although being widely used, the application of the Gassmann model on carbonate rocks have been discussed by several authors (Rossebø et al., 2005; Sørnes and Brevik, 2000; Vega et al., 2007). Due to the complexity of carbonate rocks, the assumptions behind the model makes the applicability on carbonate reservoirs questionable. Carbonate rocks hold a large variety of porosities, often consisting of large, isolated pores. In addition to this, the mineralogical composition of carbonates makes the rock highly chemically reactive when exposed to acidic solutions (Vanorio et al., 2007). For these reasons, it has been debated whether the assumptions regarding connected pores and no rock-fluid interactions make the Gassmann model inappropriate to use on carbonate rocks (Rossebø et al., 2005).

Studies performed on carbonate rocks show that saturation effects lead to both strengthening and weakening of the rock fabric, indicating both rock-fluid interactions as well as alterations in the shear moduli (Baechle et al., 2005; Grombacher et al., 2012). These alterations in shear moduli violates Gassmann's result of constant shear modulus. Adam et al. (2006) show that weakening of the shear modulus occurs at low frequencies (100 Hz), whereas strengthening occur at high frequencies (0.8 MHz).

Another limitation related to the use of Gassmann model on carbonate rocks is that pore geometry is not considered (Smith et al., 2003). Carbonate rocks typically hold pores of various shapes, which have proven to be an important contributor to variations in the elastic properties (Wang, 1997). Vanorio et al. (2007) investigated the deviation in saturated elastic moduli for values calculated by both self-consistent approximation (taking pore geometry into account) and the Gassmann model. It was established that for ellipsoidal pores, the deviation between saturated and Gassmann calculated moduli is greater than for spherical pores. Here, it is also suggested that the hidden heterogeneities in carbonate rocks are the main challenge for fluid substitution modelling using the Gassmann model.

### 3.4.2 Differential Effective Medium Modelling

With the challenges associated with the application of Gassmann modelling on carbonate rocks, there exist a line of modelling schemes assuming that pores are isolated rather than connected. These models are based upon scattering of internal reflections from inclusions within the rock. The scattering of reflected P- and S-waves occurs due to stress deviation as the strain of the inclusion is different than the strain of the surroundings (Gelius and Johansen, 2012). Differential Effective Medium (DEM) modelling is an example of a commonly used scattering model. The effective elastic parameters are found by a set of differential equations formulated by Berryman (1992):

$$(1 - \phi) \frac{d}{d\phi} [K_{DEM}(\phi)] = [K_f - K_{DEM}(\phi)] P^*, \quad (3.19)$$

$$(1 - \phi) \frac{d}{d\phi} [\mu_{DEM}(\phi)] = -\mu_{DEM}(\phi) Q^*, \quad (3.20)$$

where  $K_{DEM}(\phi)$  and  $\mu_{DEM}(\phi)$  are the effective bulk and shear modulus at a given porosity,  $K_f$  is the fluid bulk modulus, and  $P^*$  and  $Q^*$  are geometrical factors taking the aspect ratio into consideration (for more detail see Appendix A), and  $\phi$  is the porosity.

DEM modelling is performed in steps, by gradually adding a concentration of pores to the matrix. By using Kuster-Toksöz (KT) model, the new effective elastic properties are calculated, consisting of the original matrix and the added pore space. These new elastic properties now represent the new matrix to be used in the DEM modelling. A new set of pores are then embedded into the matrix, and KT-modelling is again used to calculate the new effective properties. The procedure is continued until the desired porosity value is reached (Gelius and Johansen, 2007). A schematic of the process is presented in Figure 3.2.

In contrast to Gassmann, DEM-modelling take the pore geometry into consideration when calculating the effective elastic properties. This is done by including information about the aspect ratio and aspect concentration into the equations. The aspect ratio,  $\alpha$ , is defined as the ratio between the short and the long axis. The aspect concentration,  $(\alpha_n)$  is the fractional concentration of each aspect ratio  $(\alpha_n)$ :

$$\sum_{n=1}^N c(\alpha_n) = \phi . \quad (3.21)$$

DEM modelling is asymmetric, indicating that there is a preferred matrix- and inclusion phase (Mavko et al. 2009). The modelling scheme take pore-to-pore interaction into account by incorporating higher order scattering into the calculations. It is assumed that the matrix is affected by the added pores. As a new matrix value is calculated using the previously added inclusions, pore-to-pore interaction is incorporated in the model (Gelius and Johansen, 2007). The assumptions underlying this model is that the rock in question is isotropic, linear and elastic with idealized ellipsoidal inclusions. In addition to this, there is no fluid flow between the pore space (Mavko et al. 2009).

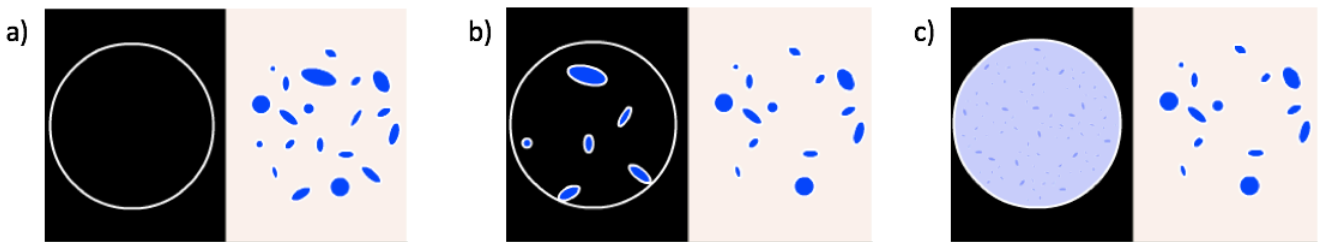


**Figure 3.2.** The figure shows a schematic of the DEM procedure. a) shows the initial rock volume and inclusions to be embedded, b) shows the embedded and remaining inclusions, c) shows the new rock volume, consisting of the properties of the embedded inclusions and the initial rock properties. Modified from Gelius and Johansen (2007).

### 3.4.3 The Kite-model

The Kite model is proposed by Avseth et al. (2014) to provide a rock physics model that considers the burial history of the sediments. By doing so, the effect of mechanical and chemical compaction on the elastic properties is taken into consideration. The modelling scheme is divided into low- and high porosity sections, as illustrated in Figure 3.3. The two end-members are connected through Hashin-Shtrikman upper bounds.

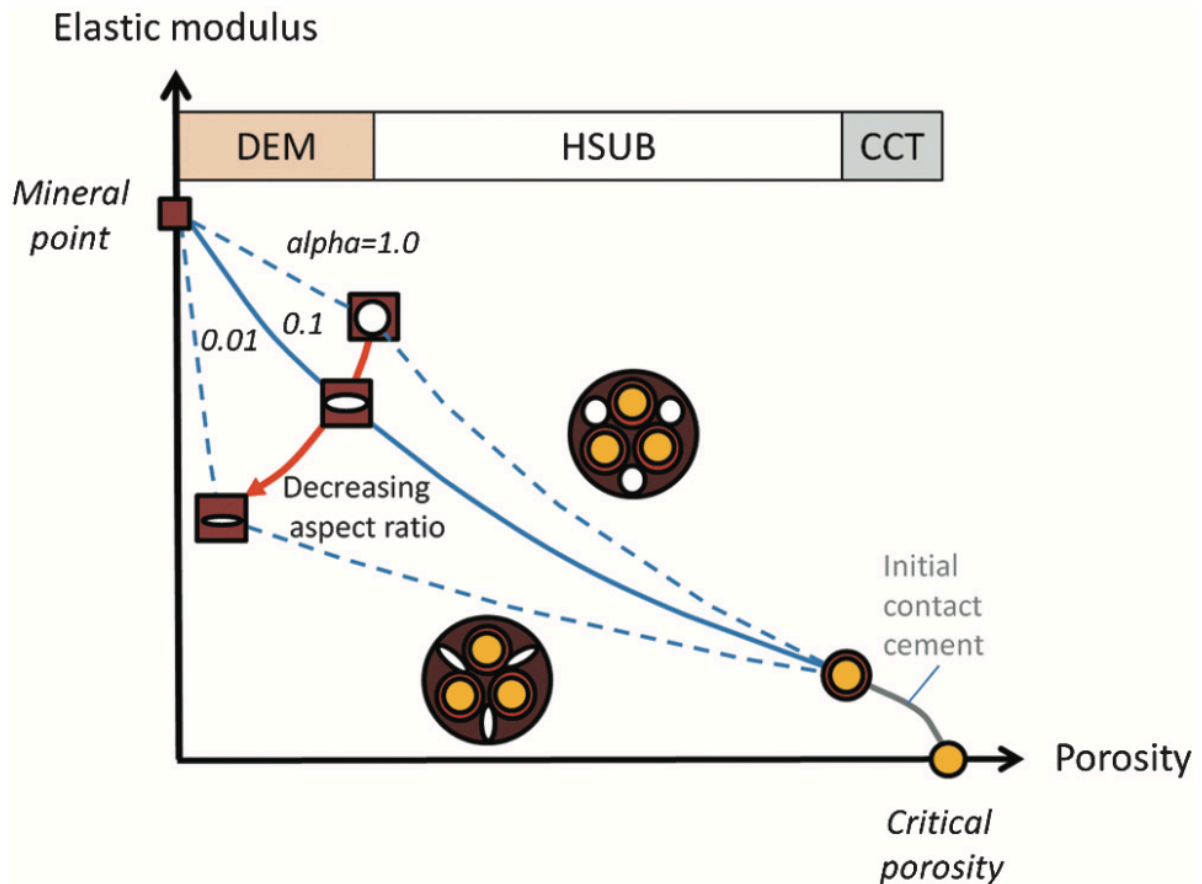


**Figure 3.3.** The figure is illustrating the variations in elastic properties using the Kite-model. The effect of pore geometries is included in the figure. The figure demonstrates the various rock physics models applied for the different porosity zones (Avseth et al., 2014).

For high porosity rocks (higher than 20%), contact models are applied. In the Kite-model, Contact Cement Theory (CCT) is used to approximate the effective elastic properties in the high porosity zone. In these models, the localization of the cement within the grain structure are of great importance, as well as the coordination number ( $n$ ). The coordination number describes the number of contact points per grain. Further, the modelling of bulk and shear modulus depend on the P-wave bulk modulus ( $M_C$ ) and the shear modulus of the cementing material ( $\mu_C$ ). Here,  $\phi_{CCT}$ , is the porosity value at the maximum porosity point. Additional information regarding the fraction of cement porosity of the unconsolidated material ( $S_C$ ) and the normal ( $S_n$ ) and shear stiffness ( $S_\tau$ ) is needed (see Appendix A for more details). The effective elastic moduli are defined as (Avseth et al., 2014):

$$K_{CCT} = \frac{n[1 - \phi_{CCT}/(1 - S_c)]}{6} M_c S_n, \quad (3.22)$$

$$\mu_{CCT} = \frac{1}{5} K_{CCT} + \frac{3n[1 - \phi_{CCT}/(1 - S_c)]}{20} \mu_c S_\tau. \quad (3.23)$$

Due to slip and/or torsion, the shear modulus calculated using CCT is generally too high. Therefore, the calculated shear modulus is multiplied by a shear relaxation factor, between 0 and 1 (Avseth et al., 2014).

In low porosity rocks however, the elastic properties are modelled using inclusion model. In the Kite-model, DEM is applied to approximate the elastic properties in the low porosity zone. Here, the models depend more on the pore structure, than on the actual porosity. This means that the effect of pore geometries is largest in the low-porosity interval, as illustrated in Figure 3.3.

To predict the elastic properties between low- and high porosity regimes, bound models are applied. These models are valuable mixing laws that accurately interpolate sorting and cementing trends (Avseth et al., 2010). Hashin-Shtrikman Upper Bound ( $HS^+$ ) is applied in the Kite model. Here, the stiff component represents the cement whose elastic properties are calculated by DEM from the low porosity interval. The soft components are defined at the maximum porosity point using CCT. When using  $HS^+$ , one assumes that the elastic moduli of the low porosity point is higher than that of the high porosity point. The elastic moduli computed using Hashin-Shtrikman upper bound is defined as (Mavko et al., 2009):

$$K^{HS+} = K_1 + \frac{f_2}{(K_2 - K_1)^{-1} + f_1(K_1 + \frac{4}{3}\mu_1)^{-1}}, \quad (3.24)$$

$$\mu^{HS+} = \mu_1 + \frac{f_2}{(\mu_2 - \mu_1)^{-1} + 2f_1(K_1 + 2\mu_1)/\left[5\mu_1(K_1 + \frac{4}{3}\mu_1)\right]}, \quad (3.25)$$

where  $K_1$  and  $K_2$  are the bulk modulus of the individual phases,  $\mu_1$  and  $\mu_2$  are the shear modulus of the individual phases and  $f_1$  and  $f_2$  are the volume fraction of the individual phases. When considering the upper Hashin-Shtrikman bound, the stiffest component is phase 1, and the

softest component is phase 2. In the case of the Kite model, the stiffest component is from DEM, and the softest component defined from CCT.

### 3.4.4 Friable Sand Model

The friable sand model describes the porosity-velocity relationship due to deteriorating sorting (Dvorkin and Nur, 1996). This theoretical model assumes that the porosity decrease from an initial value due to deposition of solid material away from the grain contacts (Dvorkin and Nur, 2000).

As for the Kite-model, the Friable sand model connects two end-points of the relationship between porosity and elastic properties. The first end-point is at critical porosity, where the elastic properties are assumed to be the same as that of spherical grains subjected to confining pressure. These elastic moduli are described by the Hertz-Mindlin theory, where information regarding the Poisson's ratio ( $\nu$ ), coordination number ( $n$ ) and critical porosity ( $\phi_c$ ) is needed. In addition, the shear modulus ( $\mu$ ) of the material and the confining pressure ( $P$ ) is used in the modelling of the effective elastic rock properties:

$$K_{HM} = \left[ \frac{n^2(1 - \phi_c)^2 \mu^2}{18\pi^2(1 - \nu)^2} P \right]^{\frac{1}{3}}, \quad (3.26)$$

$$\mu_{HM} = \frac{5 - 4\nu}{5(2 - \nu)} \left[ \frac{3n^2(1 - \phi_c)^2 \mu^2}{2\pi^2(1 - \nu)^2} P \right]^{\frac{1}{3}}. \quad (3.27)$$

Poisson's ratio is defined as (Guéguen and Palciauskas, 1994):

$$\nu = \frac{3K - 2\mu}{3K + \mu}, \quad (3.28)$$

where  $K$  and  $\mu$  are the bulk and shear modulus respectively.

At the zero-porosity end-point, the elastic properties are the effective elastic moduli of the rock forming minerals. The two end points of zero porosity and critical porosity is connected through the elastic properties described by Hashin-Shtrikman lower bounds (see Equations 3.24 and 2.25). Here, the effective elastic properties found by Hertz-Mindlin represent the less stiff



component (phase 1), and the mineral properties form the stiff component (phase 2). The effect of increasing pressure is included by incorporation of the Hertz-Mindlin model.

### **3.4.5 Limitations of Rock Physics Models**

When using rock physics models, one has to keep in mind that rocks are much more complicated than what can be incorporated into models. Rock physics models are simplifications of the real rock.

Firstly, all models hold certain assumptions that limits its application. For this reason, not all models are appropriate for all rock types. As discussed in section 1.3.1, the application of Gassmann is questionable with regards to carbonate rocks. However, the Gassmann model holds the fewest input parameters of the models discussed above. Models containing more input parameters to describe the rock are usually more complicated to use (Wang, 1997).

The application of the DEM model includes pore-to-pore interaction in the estimation of effective elastic properties. However, the model requires information about the aspect ratio and the fractional distribution of the inclusions. This information can be difficult to obtain (Kumar and Han, 2005).

The models discussed in this chapter does not simulate the effect of the whole frequency range. While Gassmann modelling simulates the low-frequency behavior of a fluid saturated rock, DEM model simulates high-frequency saturated rock behavior (Mavko et al., 2009).

## **3.5 Factors Controlling the Seismic Velocity**

The elastic properties, and thus the velocity of a rock are affected by various factors. Increased porosity reduces the stiffness of the rock, subsequently the shear and bulk modulus. As a result, a reduction in velocity is observed at increasing porosities.

However, large variations in velocity is observed over the same porosity values. Wang (1997) suggests that these differences are caused by the large variation in pore geometries in the rock. Pores with low aspect ratios reduce the stiffness of the rock, as they are easier to deform. High aspect ratio pores, on the contrary, have higher incompressibility and will as a result lead to a stiffer structure and higher elastic properties (Russel and Smith, 2007).

Also, the density is a factor controlling the seismic velocity of a rock. In theory, a reduction in velocity is to be expected as the density of the rock increases. However, this observation is rarely made. This follows that the elastic moduli increases with the density (Wang, 1997).

In addition to these intrinsic parameters, factors as differential pressure will affect the velocity. At increasing pressure pores collapse, making the rock better compacted. As a result, the rock becomes stiffer and the seismic velocity is expected to increase. Low-aspect ratio pores collapse under lower pressure compared to spherical pores. Thus, the velocity sensitivity to pressure is controlled by the pore shape (Wang, 1997). This results in elastic properties that may differ from the constituent mineral values due to variations in porosity, pore geometry and density.

### 3.6 Seismic Data and Seismic Analysis

Seismic reflection data can provide valuable information of the subsurface. Information like lithology, fluid content and petrophysical properties as porosity can be determined from seismic data.

AVA analysis can be used as an additional tool for fluid detection, whereas rock physics templates can be used for lithological characterization, porosity prediction or fluid identification. This section will briefly present some tools used in seismic analysis. AVA theory will be presented, and the applicability on carbonates will be evaluated. In addition, the effect of wave frequency on the seismic resolution, and problems related to resolution will be briefly discussed.

#### 3.6.1 Seismic Resolution

By definition, seismic resolution is the ability to separate two features that are close together. The vertical resolution is controlled by the *tuning thickness*, defined as one quarter of the seismic wavelength. The wavelength,  $\lambda$ , is defined as:

$$\lambda = \frac{v}{f}, \quad (3.29)$$

where  $v$  is the seismic velocity and  $f$  is the dominant frequency. Thus, the higher the frequency, the thinner layers can be detected. However, the attenuation effects are more dominating for higher frequencies, making it difficult to map the subsurface at greater depths.

The horizontal resolution is defined as the width of the reflection zone of which the incident seismic waves are reflected. This zone is referred to as the Fresnel zone, whose radius is defined as (Gelius and Johansen, 2012):

$$R_f = \sqrt{\frac{vz}{2f}}, \quad (3.30)$$

where  $z$  is the depth down to the target.

### 3.6.2 AVA Analysis

Amplitude-versus-angle (AVA) analysis can be used as an additional tool in seismic monitoring of reservoir fluids. This analysis uses the variations in seismic amplitudes as a function of incident angle to map the changes in reservoir fluid content. The procedure is relevant in monitoring of CO<sub>2</sub> injections, as the fluid substitution process leads to alterations in the AVA parameters. As a result, the technique may provide a more sensitive discriminator for the presence of CO<sub>2</sub> than standard geophysical methods (Brown et al., 2007).

The angle dependency of amplitudes, is described by AVA. The analysis studies the variations in amplitudes along a reflector as a function of offset or incident angle. Information about the P- and S-wave velocities are obtained through a simplified expression for  $R_{PP}$  (Gelius and Johansen, 2012):

$$R_{PP} = \frac{P_{refl}}{P_{inc}}, \quad (3.31)$$

where  $P_{refl}$  and  $P_{inc}$  are the reflected and incident P-waves respectively. As the incident P-wave hits the target reflector, it is converted to transmitted and reflected P-and S-waves, illustrated by Figure 3.4. Thus,  $R_{PP}$  indirectly contains information about both compressional and shear waves (Mavko et al., 2009).

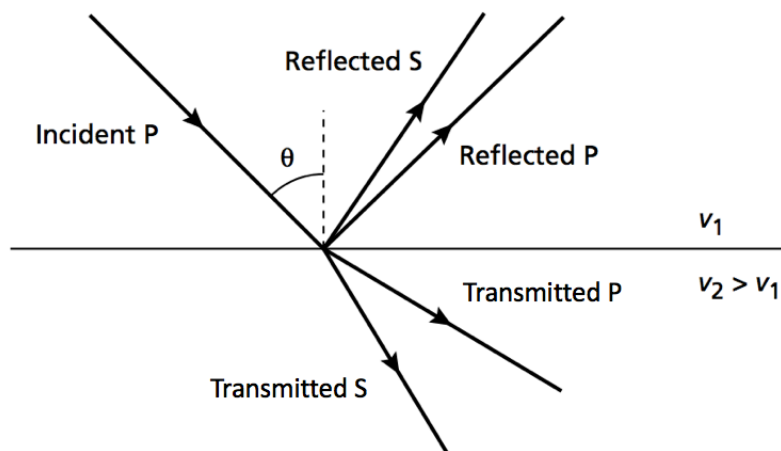


**Figure 3.4** The figure illustrates the reflection and transmission of an incident P-wave. Modified from Kearey et al. (2002).

More specifically, through AVA one analyzes the variations in seismic energy reflected from a reservoir. It represents the contrast in acoustic impedance between the target zone and the overburden. AVA uses information obtained from both P- and S-wave velocities. It should as a result be more sensitive to variations in reservoir fluids than conventional 4D seismic that only uses information from P-wave velocity (Brown et al., 2007).

### The Zoeppritz Equation and Wiggins Approximation

The Zoeppritz equations describe the reflection and transmission coefficients as a function of angle and three independent elastic parameters on each side of the reflecting interface (Castagna and Chopra, 2014). The equations are however quite complex, and give little room for physical interpretation of how the amplitude is related to the various seismic parameters. Over the years, several approximations to the Zoeppritz equations have been developed to provide a more informative description of the amplitude behavior.

Wiggins or Gelfand approximation offer a more insightful interpretation of the Zoeppritz equation. This approximation assumes small angles and  $v_p/v_s = 2$  (Gelfand et al., 1988):

$$R(\theta) = R_p + G \sin^2 \theta, \quad (3.32)$$

where

$$G = R_p - 2R_s, \quad (3.33)$$

and  $R_p$  is the AVO intercept,  $G$  is the AVO gradient and  $\theta$  is the angle of incidence.

$$R_p = \frac{1}{2} \left[ \frac{\Delta v_p}{v_p} + \frac{\Delta \rho}{\rho} \right], \quad (3.34)$$

$$R_s = \frac{1}{2} \left[ \frac{\Delta v_s}{v_s} + \frac{\Delta \rho}{\rho} \right], \quad (3.35)$$

where  $\Delta v_p$  and  $\Delta v_s$  is the P- and S-wave velocity contrast between two interfaces and  $\Delta \rho$  is the density contrast between two interfaces. Further  $v_p$  and  $v_s$  is the velocity of the lower layer, and  $\rho$  is the density of the lower layer.

When the intercept ( $R_p$ ) and gradient ( $G$ ) is of opposite signs, the reflection magnitude will decrease with angle. Equal signs will induce increasing reflection magnitude with angle (Castagna and Chopra, 2014).

### **AVA and carbonate rocks**

Due to the stiff frame of the carbonate rock, it is believed that the fluid effect poses a small contribution to the seismic properties. This indicates that the AVA response in carbonate rocks might be more subtle than in siliciclastic rocks (Castagna and Chopra, 2014). Experiments performed on a dataset from the Wilson basin (carbonates) show that at zero offset, the amplitude is an attribute that can be used to separate brine and gas saturated data (Li et al., 2003). However, it has been questioned whether the complex pore geometry of carbonates can produce the same elastic effects as the pore fluids at zero-offset.

Li et al. (2003) establish the presence of all four carbonate classes when examining the AVA response of a carbonate reservoir. Originally, three AVA-classes were defined for gas-sands (Rutherford and Williams, 1989). Later, a fourth class was added by Castagna et al. (1998). Figure 3.5 provides an illustration of the four AVA classes. Class 1 has high impedance, and a positive reflection coefficient at zero-offset. The AVA gradient is negative, meaning that the amplitude decreases with increasing angle. Class 2 has a small contrast in acoustic impedance and a strongly negative AVA gradient. The reflection coefficient can be either positive, resulting in reduced amplitudes, or negative, resulting in increased amplitudes. Class 3 has lower acoustic impedance than the encasing medium, resulting in a negative reflection coefficient. As the AVA gradient is negative, the amplitude becomes more negative at increasing offset. Class 4 represents low impedance sand with a negative reflection coefficient at zero-offset, and a negative gradient. This means that the amplitude will increase with increasing angle. In carbonate rocks, class 1 AVO response represents tight reservoirs whereas class 4 response represents good reservoirs (Li et al., 2003).

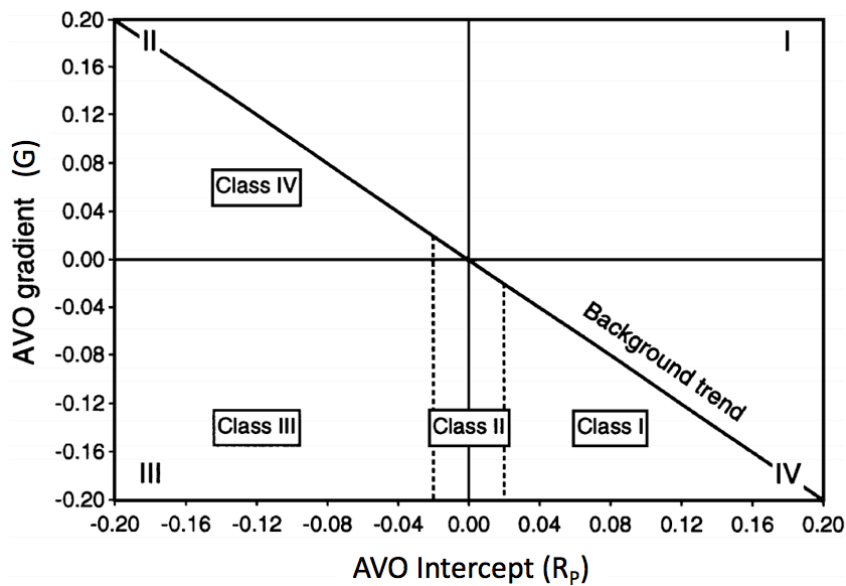


**Figure 3.5** The figure is displaying the AVO intercept ( $R_p$ ) versus gradient ( $G$ ) cross-plot, showing the four different AVO classes (Castagna et al., 1998).

### 3.6.3 The Rock Physics Template

Rock physics modelling is an important part of quantitative seismic data analysis. Avseth and Ødegaard (2004) present the rock physics template as an additional tool for interpretation of well data.

The rock physics template is based on theoretical rock physics trends for different lithologies. Various rock physics models are utilized to include the effect of pressure, saturating pore fluids etc. when determining the elastic properties of a rock. From this information, the velocity and density can be used to determine both the velocity ratio and acoustic impedance (Avseth and Ødegaard, 2004).

Figure 3.6 shows a rock physics template (RPT) including the trends for various geologic parameters in sandstones and shales. Similar templates for carbonate rocks are difficult to find in literature. Carbonates display a complex pore structure and velocity-porosity relation. Thus, one may not expect the same seismic trend as the one described in the figure below.

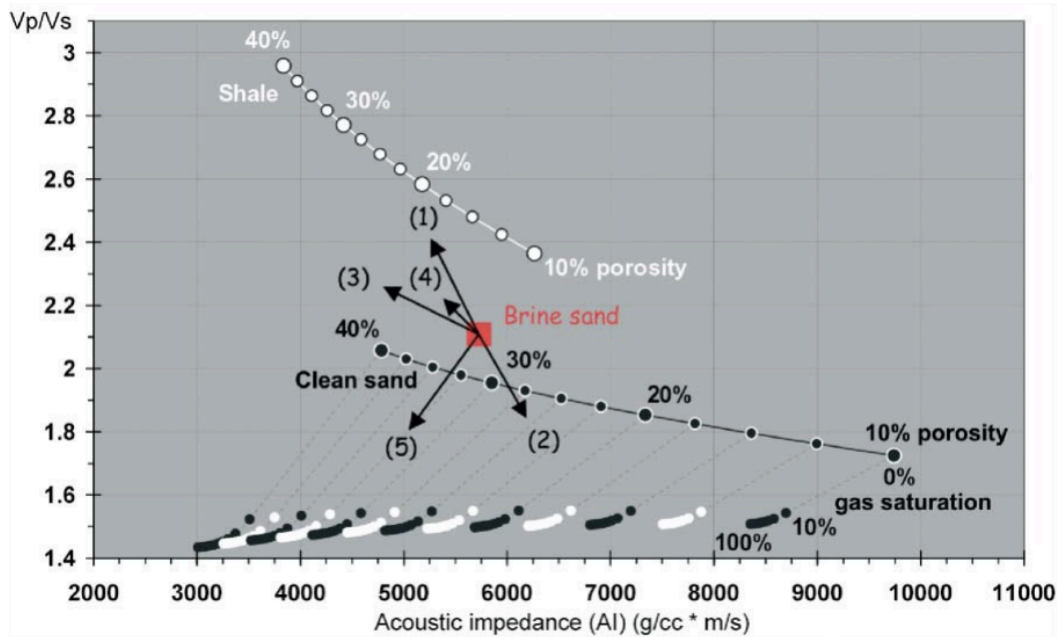


**Figure 3.6.** The figure shows the rock physics template of sandstones and shales. The template includes porosity, saturation and lithology effects. The black arrows show various geological trends: 1) increasing shaliness, 2) increasing cement volume, 3) increasing porosity, 4) decreasing effective pressure and 5) increasing gas saturation (Avseth and Odegaard, 2004).

### 3.7 The Physical Properties of CO<sub>2</sub>

Subsurface injections of CO<sub>2</sub> have been proposed as an alternative to reduce the concentration of CO<sub>2</sub> in the atmosphere (Metz et al., 2005). In order to successfully monitor the injected fluids, the properties of CO<sub>2</sub> should be evaluated and included in the modelling scheme.

By modelling the elastic properties of the injected CO<sub>2</sub>, one could investigate the movement and potential leakage of the injected fluids. To perform such a modelling, it is important to understand how the fluid properties are affected by extrinsic parameters such as pressure and temperature.

This section will provide a short evaluation of factors controlling the physical properties of CO<sub>2</sub>, and how this will affect the seismic response of a CO<sub>2</sub> saturated reservoir.

#### 3.7.1 Carbon Dioxide (CO<sub>2</sub>)

Carbon dioxide is a chemical compound, consisting of two elements; carbon and oxygen. The CO<sub>2</sub> molecule consists of one carbon atom and two oxygen atoms. The ratio is thus 1:2. CO<sub>2</sub> occurs naturally in the atmosphere, and plays an important role in controlling the Earth's environment (Metz et al., 2005). Because it does not condense and precipitate from the atmosphere at current climate temperatures, CO<sub>2</sub> contributes to controlling the atmospheric

temperature (Lacis et al., 2010). Examples of natural CO<sub>2</sub> sources are human breathing or volcanic activity. However, over the last decades, the atmospheric concentration has increased due to anthropogenic activities, such as burning of fossil fuels (Freund et al., 2003).

### 3.7.2 Physical Properties of CO<sub>2</sub>

In general, CO<sub>2</sub> has dramatically different properties than oil or brine. The phase properties of CO<sub>2</sub> are affected by variations in pressure and temperature (Freund et al., 2003). Figure 3.7 provides an illustration of the variation in CO<sub>2</sub> properties. At super critical state, CO<sub>2</sub> can change into liquid or gaseous phase without phase boundaries (Pruess, 2004). This stage occurs at temperatures above 31°C and pressure of more than 7.38 MPa. Above the critical temperature, CO<sub>2</sub> behaves like a gas. Below the critical temperature and above the critical pressure, CO<sub>2</sub> is a liquid (Wang et al., 1998).

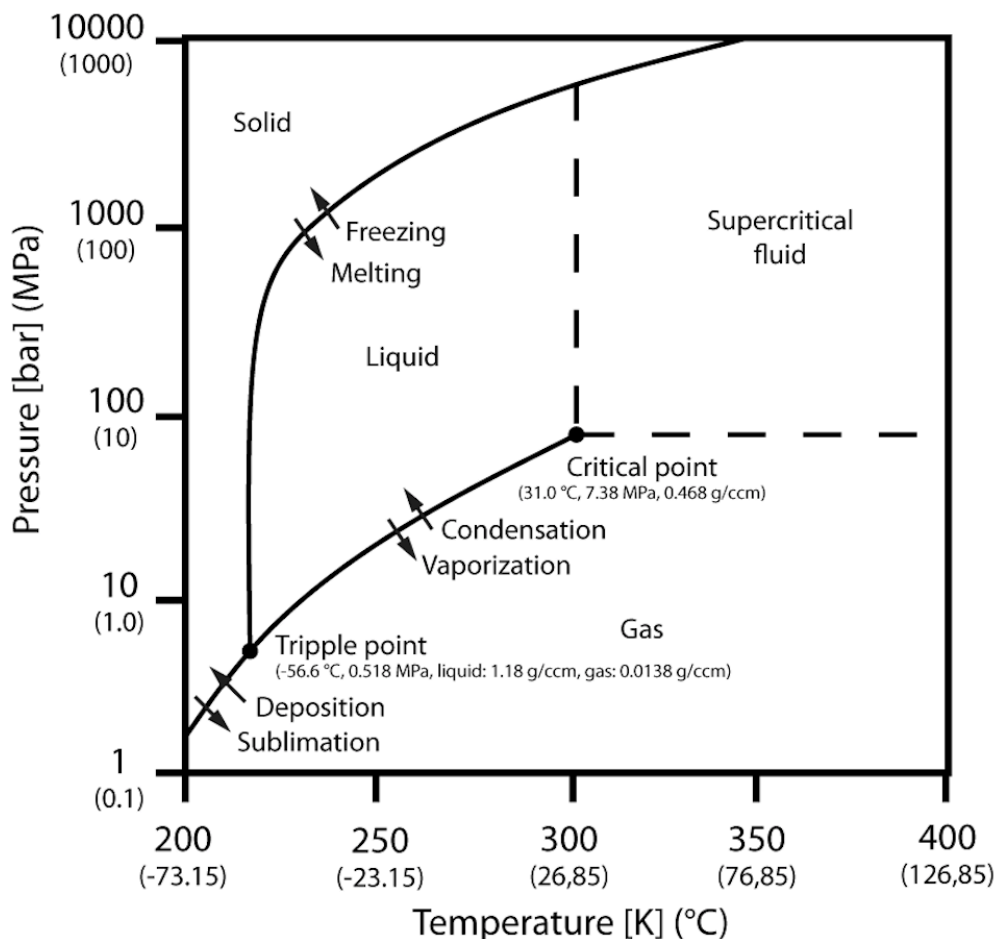


**Figure 3.7.** The figure is showing the phase diagram for CO<sub>2</sub> at various pressure and temperatures (curtesy of Erling Hugo Jensen).

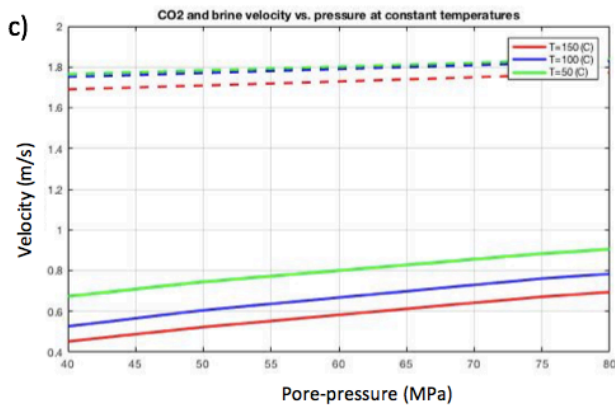
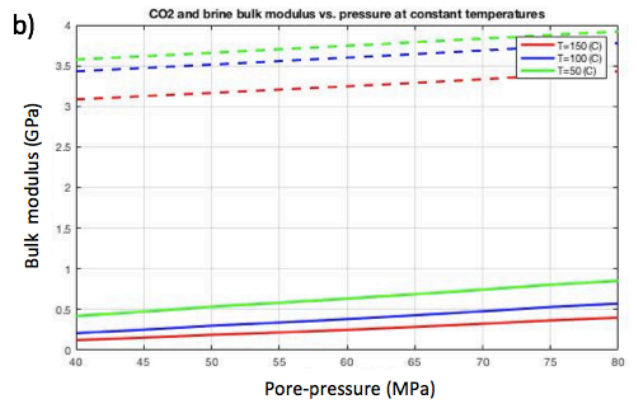
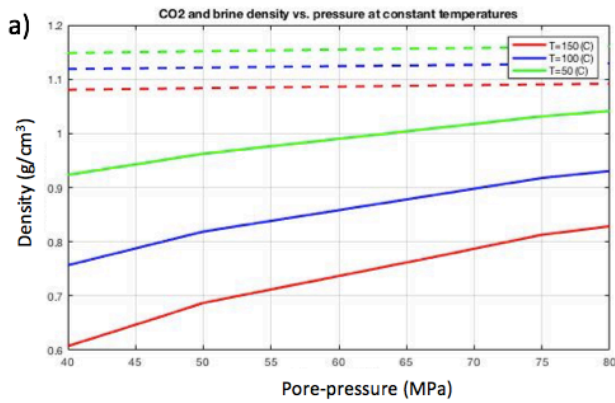


### 3.7.3 CO<sub>2</sub> Properties as a Function of Temperature and Pore-Pressure

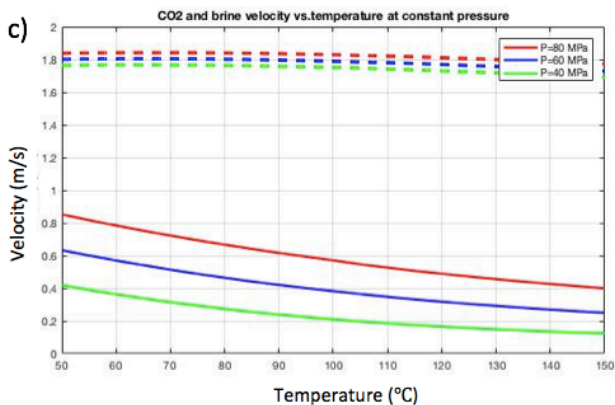
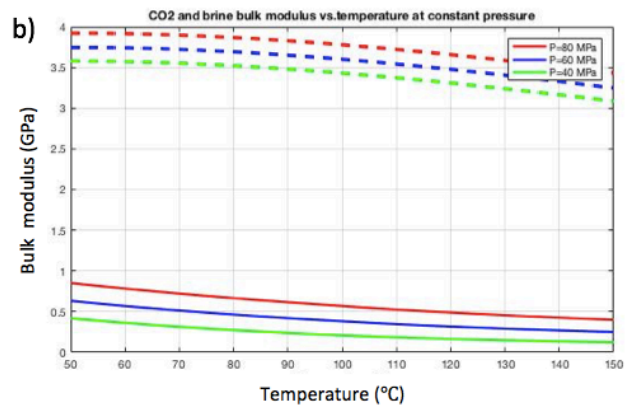
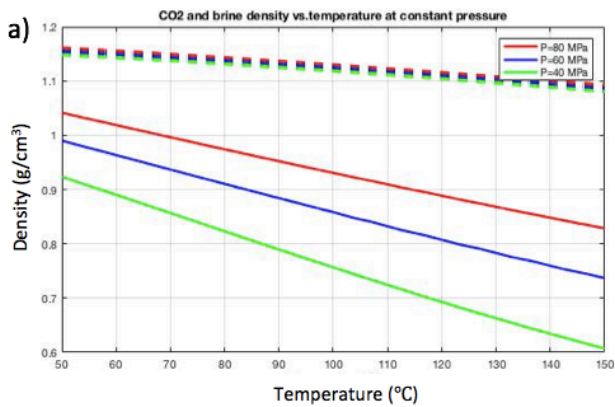
The equation of state describes the phase properties of CO<sub>2</sub> at various pore-pressure and temperatures (Span and Wagner, 1996). The dotted and solid lines in Figures 3.8 and 3.9 represent the properties of brine and CO<sub>2</sub> respectively. Comparing the bulk modulus and density of CO<sub>2</sub> and brine reveals a large contrast between the two.

Figure 3.8 describes the properties of brine and CO<sub>2</sub> at increasing pore-pressure and constant temperatures. The properties display a proportional relationship with pore-pressure; increasing the pore-pressure induce increasing property values. Also, a sensitivity pattern is revealed. The density is more sensitive to pressure at high temperatures. The bulk modulus will on the other hand reveal an opposite trend, with higher pore-pressure sensitivity at lower temperatures. To perform accurate rock-physics modelling, the variations in the fluid properties has to be accounted for.

Figure 3.9 describes the properties of CO<sub>2</sub> and brine at increasing temperature and constant pore-pressure. The properties display an inversely proportional relationship to the temperature; increasing the temperature induce a reduction in the property values. A sensitivity pattern for the temperature dependency is revealed as the pore-pressure value is varied. The effect of temperature on density is largest at low pore-pressure, whereas the bulk modulus shows largest reduction due to temperature at high pore-pressure. These parameters play a major control on the seismic velocity of the fluids



**Figure 3.8.** The figure is showing the pressure dependency of CO<sub>2</sub> - a) density, b) bulk modulus and c) P-wave velocity at fixed temperature values. Red line represents 150°C, blue line represents 100°C and green line represents 50°C.



**Figure 3.9.** The figure is showing the temperature dependency of CO<sub>2</sub> - a) density, b) bulk modulus and c) P-wave velocity at fixed pressure values. Red line represents 80 MPa, blue line represents 60 MPa and green line represents 40 MPa.

### 3.7.4 The Effect of Pore-Pressure and Temperature on Acoustic Impedance

The acoustic impedance, AI, controls the reflectivity of the reservoir. Figure 3.10 demonstrates how both pore-pressure and temperature affect the acoustic impedance of CO<sub>2</sub> and brine. This information is valuable because it provides an estimate of the expected seismic response of the reservoir fluids.

Figure 3.10a demonstrates the effect of increasing the temperature on the acoustic impedance. A reduction is expected, which also correspond well to the observations described in Figure 3.9. In addition, there appears to be little variations in the temperature sensitivity due to pore-pressure.

Figure 3.10b demonstrates the effect of increasing the pore-pressure on the acoustic impedance. An increase is expected, which correlates well with the observations in Figure 3.8. There is a large contrast in the acoustic impedance from the lowest pore-pressure/temperature value to the highest. Also, the contrast in acoustic impedance between brine and CO<sub>2</sub> is of significance. This underlines the importance of including these extrinsic parameters in the modelling procedure.

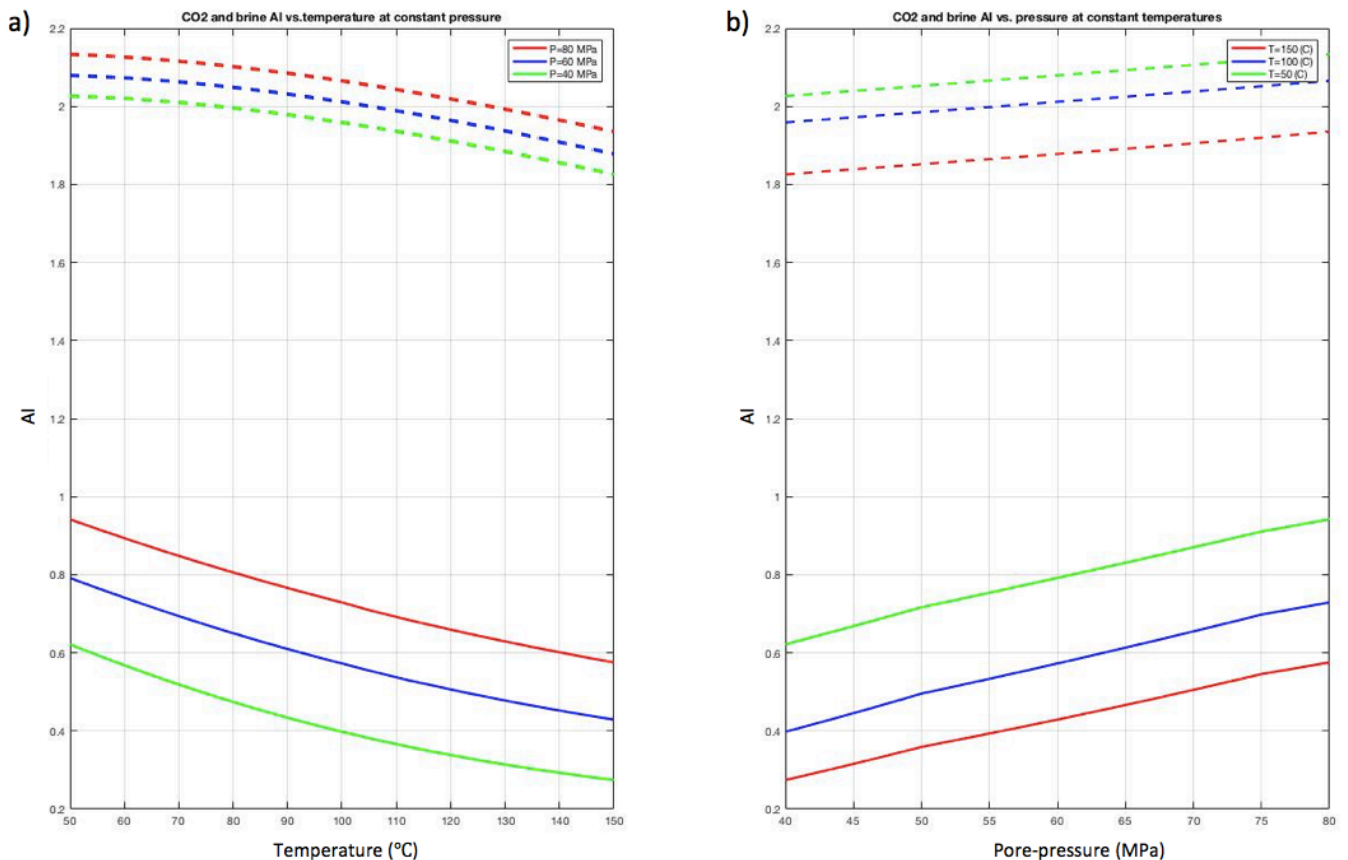


**Figure 3.10.** The figure is showing the variation in acoustic impedance as a function of a) temperature and b) pore-pressure.

### 3.8 Summary

The seismic velocity in a rock is controlled by its elastic properties and density. The rock density is controlled by the rock forming minerals. However, elastic properties are affected by factors as porosity, pore-shape or pressure.

The complexity of carbonates in terms of pore type and pore shape, makes rock physics modelling somewhat difficult, and rise questions to the applicability of existing rock models. Limitations in the existing models compromise the accuracy of the results. Whereas the Gassmann model seems like the easiest model to use, the assumptions underlying the equations makes the application on carbonates questionable. Using the differential effective medium modelling, pore geometry and pore-to-pore interaction is taken into consideration. Models as the Kite-model includes the effect of burial and compaction, providing what may seem like a more realistic model of the rock properties. The effect of different pore fluids on the rock properties can be incorporated into the Kite model using the Gassmann equation. It is apparent that considerations are needed before selecting the appropriate model to represent the carbonate rock.

With regards to pore fluids, it is clear that knowledge regarding the properties of CO<sub>2</sub> is important to perform accurate modelling. The seismic properties of CO<sub>2</sub> exhibit large variations due to both pore-pressure and temperatures. The magnitude of these alterations as a result of increasing pore-pressure also depend on temperature, and vice versa. As a result, information about these parameters should be included to the modelling, as they will affect the seismic response of a CO<sub>2</sub> saturated reservoir.

The variations in seismic properties and velocities will cause different seismic signatures, which are important to keep in mind when performing rock physics modelling. The expected contrast between brine and CO<sub>2</sub> is important to evaluate, as it can provide valuable information regarding the expected alterations caused by fluid substitution.

## 4 Geochemical Alterations in Carbonate Rocks

Carbonate rocks are chemically reactive. When exposed to acidic solutions, the rock is prone to chemically induced alterations. These alterations may affect the pore shape or porosity due to dissolution or precipitation of carbonate minerals. The seismic attributes of the carbonate rocks are affected by these alterations.

By seismic monitoring of carbonate reservoirs exposed to CO<sub>2</sub> injections, it is suggested that the observed reductions in both P- and S-wave velocities are too large to be explained by fluid substitution alone (Grombacher et al., 2012). It is therefore an interesting topic to look at how injections of CO<sub>2</sub> will affect the elastic properties of the rock. This chapter will provide an overview over possible alterations occurring in the fabric of carbonate rocks due to geochemical reactions.

### 4.1 Carbonate Reactivity

The injection of a chemically reactive fluid into deep carbonate reservoirs will lead to disequilibrium between fluid and host rock. CO<sub>2</sub> is normally injected into the reservoir at a supercritical state (Nordbotten et al., 2005). When injections are performed in brine saturated reservoirs, supercritical CO<sub>2</sub> will react with the reservoir fluid, generating an acidic solution (André et al., 2007):



Separation of this carbonic acid leads to the formation of bicarbonate ions:



Geochemical modelling suggests that supercritical CO<sub>2</sub> in contact with brine should hold a pH of approximately 3. At this pH level, the reservoir fluid should be undersaturated carbonate minerals. However, samples obtained from observation wells in areas where CO<sub>2</sub> is injected, show reduced pH values and high concentration of carbonate minerals. It is suggested that the reduction in pH is restrained by the dissolution of carbonate minerals (Grombacher et al., 2012).

## 4.2 Geochemically Induced Alterations in Rock Fabric

When applying the Gassmann fluid substitution model, one assumes that there are no rock-fluid interactions (Adam et al., 2006). As discussed in previous sections, carbonates are highly exposed to fabric alterations following rock-fluid interactions. The Gassmann model is thus in danger of miscalculating the elastic properties of the carbonate rocks facing CO<sub>2</sub> injections.

Vanorio et al. (2011) suggest five possible scenarios which can occur upon substituting brine with CO<sub>2</sub>, illustrated in Figure 4.1. The first scenario demonstrates the expected alterations in elastic moduli using Gassmann equation assuming an unaltered rock-frame. The bulk modulus is reduced, whereas the shear modulus is left unaltered (blue line).

The remaining four scenarios illustrate the effect of Gassmann fluid substitution performed on an altered rock frame. The effect of increased porosity due to dissolution is illustrated by the solid, red line. The red, dashed line demonstrates the modelled effect of cement removal and mineral dissolution. These processes lead to reduced rock stiffness in addition to enhanced porosity. The dotted red lines illustrate the effect of cement removal alone. All of these processes lead to reductions in both bulk and shear modulus. This latter effect is a clear violation of Gassmann's results.

The green line indicates the effect of precipitation followed by reduced porosities. The alterations are expected to lead to a slightly reduced bulk modulus, and an increased shear modulus.

The results presented by Vanorio et al. (2011) demonstrate the importance of considering rock-fluid interactions when modelling the effects of fluids on rock properties.

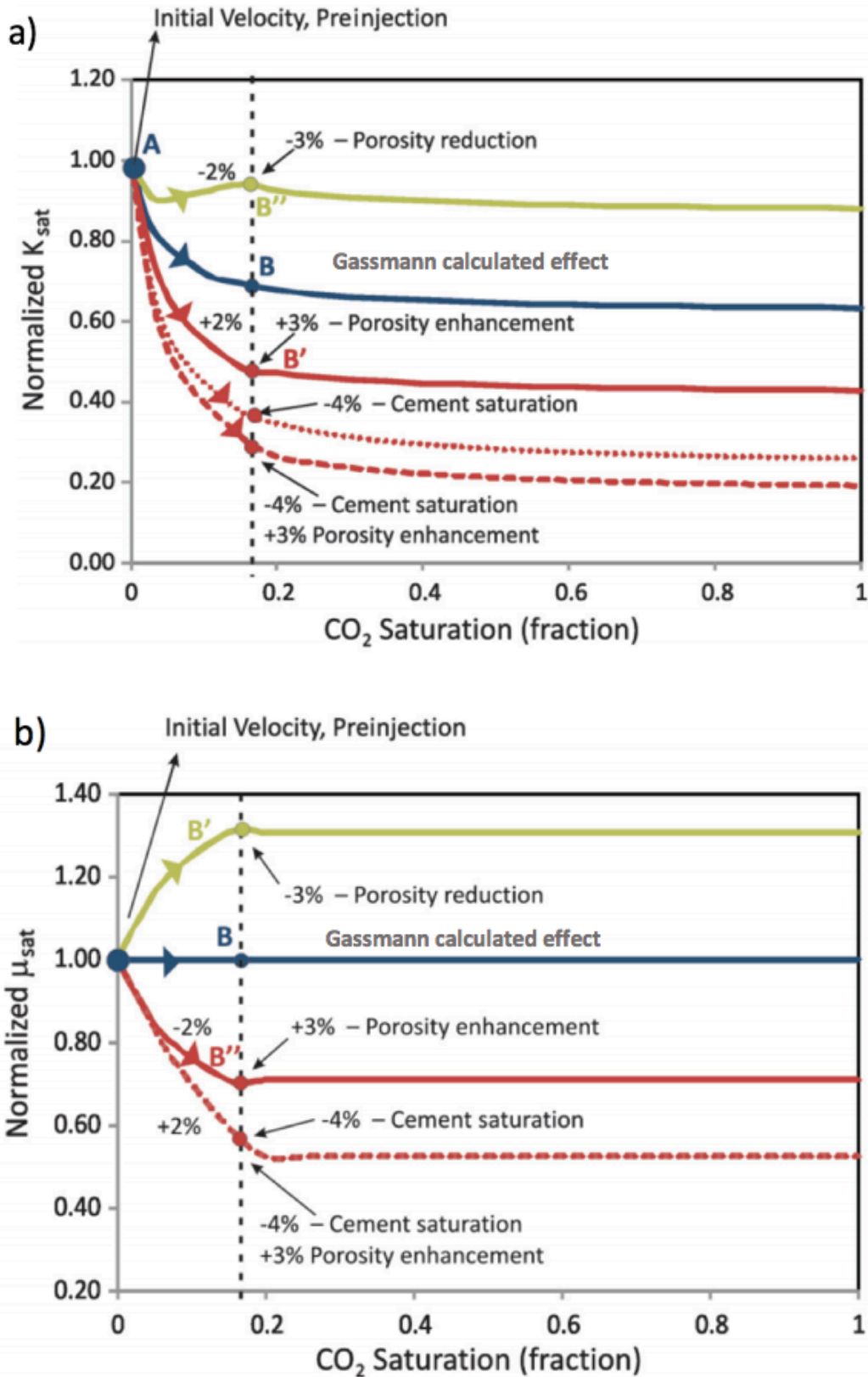
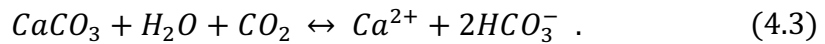


**Figure 4.1.** The figure illustrates the expected alterations in a) bulk modulus and b) shear modulus as a result of geochemical interactions between fluid and rock (Vanorio et al., 2011).

### 4.3 Dissolution of Carbonate Minerals

When calcite rich carbonate rocks (chalks) are exposed to CO<sub>2</sub>, the resulting dissolution of calcite can be represented by the following equation (Vialle and Vanorio, 2011):



Dissolution of CO<sub>2</sub> into the formation brine leads to a thermodynamic state of disequilibrium that drives the dissolution of carbonate minerals. This process releases cations, that form a buffer to the acidic solution resulting from CO<sub>2</sub> injections in brine reservoirs (Eq.4.1 and 4.2) (Nogues et al., 2013). Dissolution target the porosity, pore geometry and the stiffness of the carbonate rock, affecting its elastic properties. Alterations in the elastic properties may cause large variations in seismic velocities and the seismic signature of the injected rock. These variations may be different from the changes predicted by Gassmann model, leading to misinterpretations regarding the location of the injected fluids (Grombacher et al., 2012).

#### 4.3.1 Dissolution Effects on Porosities

Several experimental studies have been performed to investigate the effect of CO<sub>2</sub> injections on the seismic properties of carbonate rocks (Grombacher et al., 2012; Vanorio et al., 2011; Vanorio, 2015).

Vanorio (2015) evaluated how the physical properties of the rock frame itself changes upon injection of an CO<sub>2</sub> aqueous solution. By considering a sample of tight mudstone and granular packstone, the effect of the initial rock fabric is included in the experiment. It is established that the initial fabric is an important factor controlling the effect of dissolution on the pore space. A general reduction of the overall bulk and shear modulus is measured as a response to the CO<sub>2</sub> injections (Vanorio, 2015).

When considering the dry rock frame of a mudstone, Vanorio (2015) suggests that the reduction in the elastic moduli is caused by increased pore compliance as a result of reduced aspect ratio. The increased compliance follows the enhancement of microcracks (Vanorio, 2015).

In more granular rocks, such as packstone, dissolution targets the microcrystalline matrix leading to increased pore volume. In this case the pore geometry is left unaltered (Vanorio, 2015). Figures 4.2 and 4.3 illustrate the effect of dissolution in mudstone and packstone respectively.



Grombacher et al. (2012) explored the alterations occurring in the microstructure of carbonate samples following CO<sub>2</sub> injections. A pattern of dissolution targeting pores with microcrystalline matrix was revealed. This selective dissolution leads to the formation of crack-like pores with low aspect ratios, as illustrated in Figure 4.4 (Grombacher et al., 2012). From these experiments, Vanorio (2015) and Grombacher et al. (2012) establish the control of the initial rock fabric on the dissolution effects.

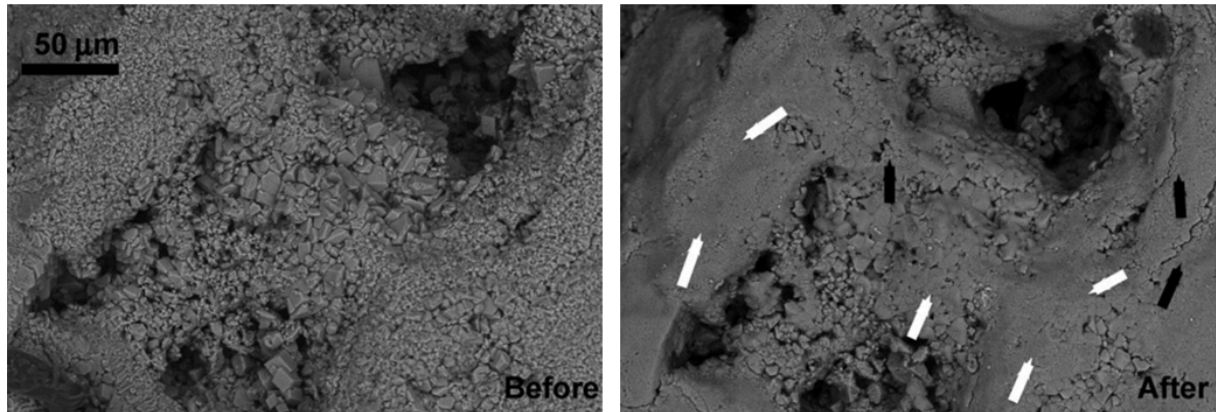


**Figure 4.2.** The figure provides an illustration of the changes in microstructure in mudstone due to formation of cracks, indicated by black arrows (Vanorio, 2015). The left-side figure displays the rock fabric prior to injections, the right-side figure displays the rock fabric post injection (SEM images).

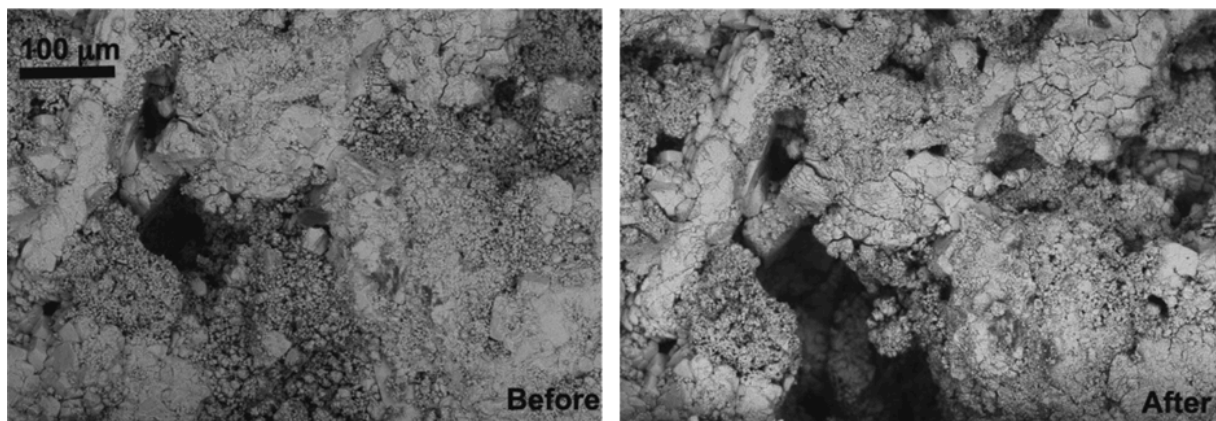


**Figure 4.3.** The figure provides an illustration of the changes in microstructure of granular rocks due to dissolution of microcrystalline matrix (Vanorio, 2015). The left-side figure displays the rock fabric prior to injections, the right-side figure displays the rock fabric post injection (SEM images).

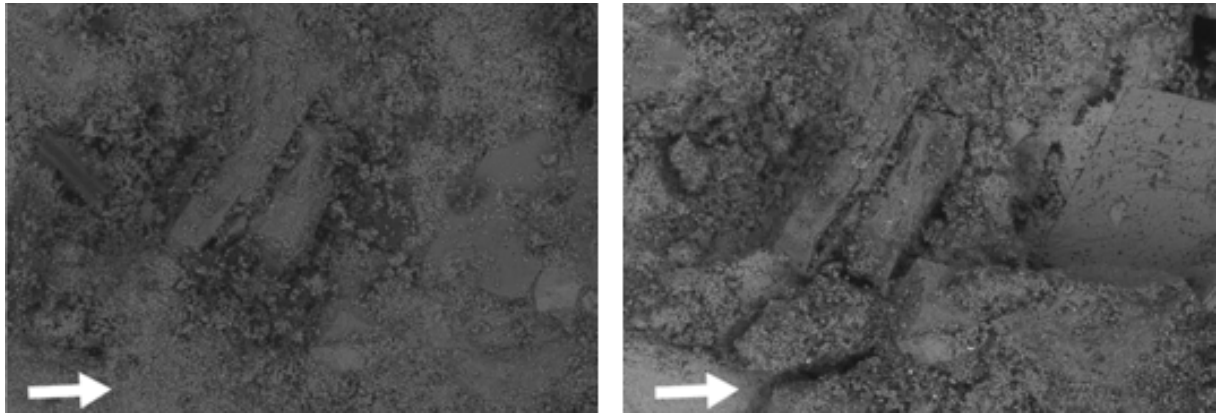


**Figure 4.4.** The figure provides an illustration of the formation of crack-like pores due to dissolution of microcrystalline matrix (Grombacher et al., 2012). The left-side figure displays the rock fabric prior to injections, the right-side figure displays the rock fabric post injection (SEM images).

### 4.3.2 Pressure Effects due to Dissolution

When assessing the alterations in the seismic signature of carbonate rocks subjected to CO<sub>2</sub> injections, the effect of compaction and pressure should be evaluated. As discussed in the previous section, dissolution of carbonate minerals leads to the formation of pores with low aspect ratios that deforms more easily than spherical pores.

The following equation describes the changes in crack aperture as a result of differential pressure,  $P$  (Guéguen and Palciauskas, 1994):

$$a = a_0 \left[ 1 - \frac{2(1-\nu^2)}{\alpha E} P \right], \quad (4.4)$$

where  $a$  is the crack aperture, meaning the shortest axis of the crack or pore,  $a_0$  is the zero-pressure aperture,  $\nu$  is Poisson's ratio (Eq.3.28),  $E$  is Young's modulus and  $\alpha$  is the aspect ratio (defined in section 3.4.2).

Wang (1997) illustrates the effect of pore shape on velocity alterations due to increasing pressure. Carbonate rocks dominated by moldic porosity generally show a low velocity sensitivity to increasing pressure. This is explained by the stiff structure of the pores, making them less affected by increasing overburden pressure. Cracks, on the contrary, show increased sensitivity to pressure due to the compliant structure of cracks. Figure 4.5 illustrates the effect of increasing pressure on the seismic velocity in rocks dominated by crack like- and spherical pores.

When the rock fabric is altered following dissolution processes, the overburden pressure may thus lead to continuing compaction and alteration of the pore geometry of the rock.

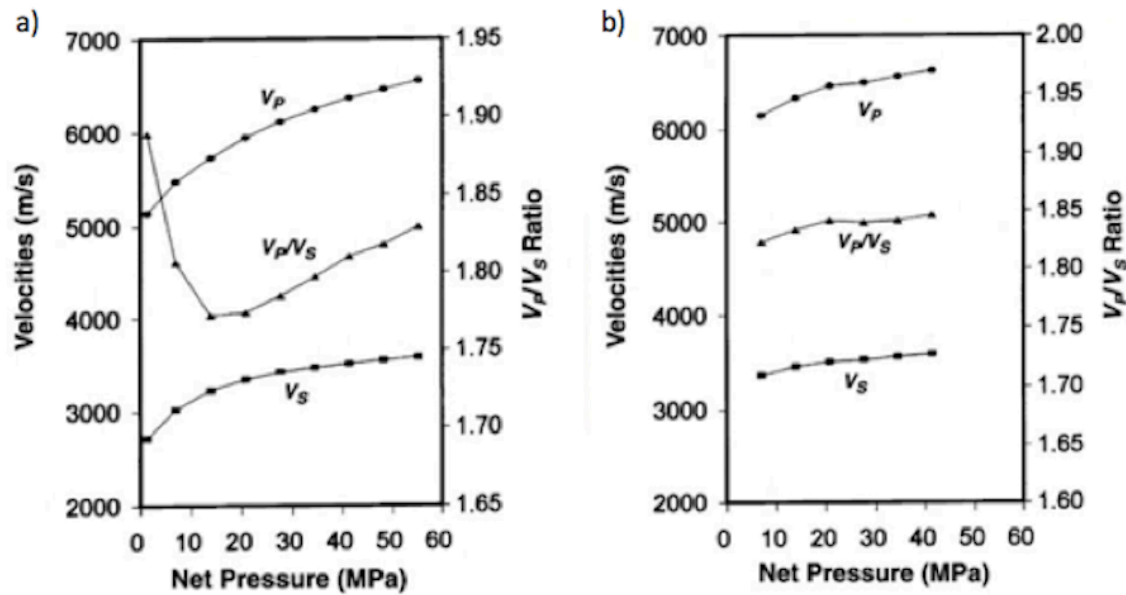


**Figure 4.5.** The figure is displaying the relationship between velocity and pressure for a) carbonate rocks dominated by crack-like pores, b) carbonate rocks dominated by moldic pores (Wang, 1997).

#### 4.4 Precipitation of Carbonate Minerals

When  $\text{CO}_2$  dissolves into the formation water, the pH of the water is reduced to a value of approximately 3 (section 4.1). Due to the acidic nature of the water, dissolution of carbonate minerals occurs. The formation water becomes oversaturated in bicarbonate and carbonate minerals. As a result, precipitation of carbonate minerals can follow along the margins of the injected  $\text{CO}_2$  plume as time progresses. Precipitation of calcium carbonates is a common geochemical reaction, leading to porosity reductions (Zhang et al., 2010). De-dolomitization occurs as a result of the high dissolution rate of gypsum. This phenomenon considers the increased concentration of calcite in the reservoir fluid following gypsum dissolution. Precipitation of calcite is thereby promoted. This process gives a stiff pore structure (Vanorio et al., 2008)

Experiments performed on injecting  $\text{CO}_2$ -water enriched in calcite show that precipitation occurs in the pore-throats of the injected sample. Figure 4.6 illustrates the precipitation of magnesium-calcite on an oolite surface (Luquot and Gouze, 2009). Precipitation occurs as the pressure decreases, and the solubility of the carbonate minerals is

reduced. The resulting reductions in porosity and clogging of the pore-throats reduces the fluid mobility, and thus the rock-fluid interaction may be curbed. The creation of isolated inclusions leads to a violation of Gassmann's assumption of connected pores. In addition, the reduced porosity may affect the seismic attributes of the injected reservoir, leading to increased velocities (Anselmetti and Eberli, 1997).

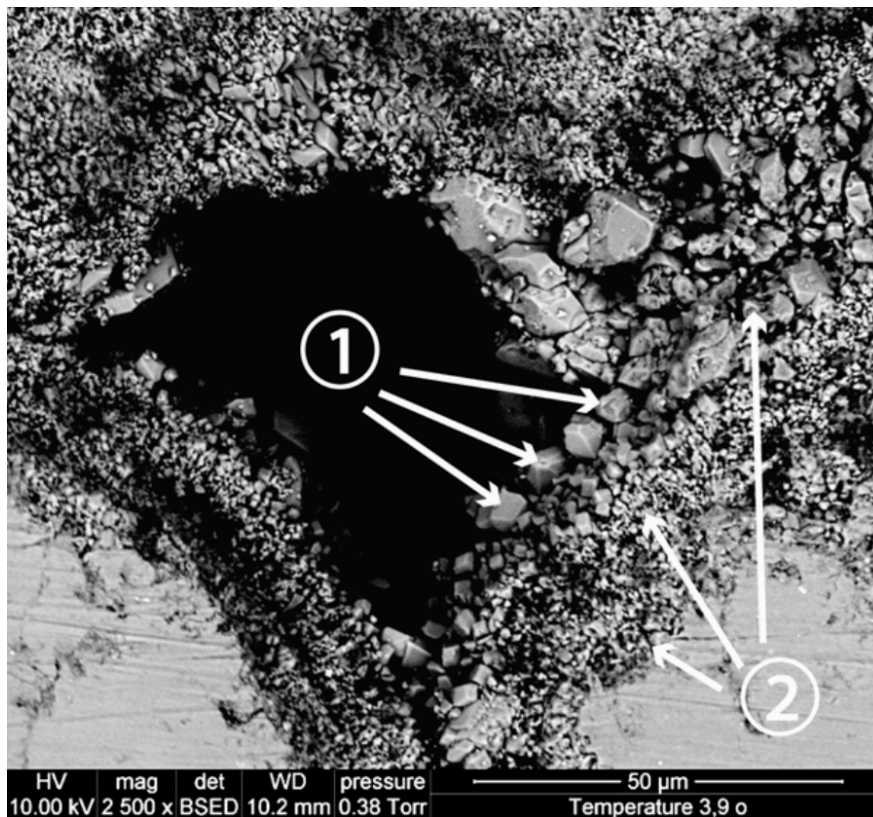


**Figure 4.6.** The figure provides an illustration of precipitation of magnesium-calcite on an oolite surface (Luquot and Gouze, 2009).

#### 4.5 Summary

When  $\text{CO}_2$  is dissolved into the formation brine, the solution becomes acidic. As a result, the rock-fluid system reaches a state of thermodynamic disequilibrium. Due to the disequilibrium, dissolution of carbonate minerals leads to alterations of the initial rock fabric. The pore space is altered, leading to the formation of crack-like pores or increased pore volumes. These effects reduce the stiffness of the rock, thus altering the dry elastic properties.

The microstructure has however proven to be an important contributor to how the rock fabric responds to dissolution and pressure. In tight carbonate rocks, dissolution leads to the formation of crack-like pores. As the pressure increase, the porosity is reduced due to closure of the more elongated pores. In more granular carbonates, dissolution leads to increased

porosity. The seismic properties of carbonate rocks dominated by spherical pores show little response to increasing pressure.

Reductions in porosity due to precipitation can occur when the pressure is reduced and the formation water is oversaturated with carbonate minerals. The reduced solubility of carbonate minerals leads to precipitation and clogging of pore throats.

All of these effects contribute to variations in the seismic signature of the reservoir. When performing rock-physics modelling on rocks where fabric alterations is likely to occur, these effects should at least be evaluated.



## 5 Data Calibration and Modelling Methods

The dataset used for the seismic modelling in this thesis is collected in the North Sea. The logs are illustrated in Figure 5.1. The blue square represents the area of which the modelling is performed. The interval of interest is a chalky reservoir zone, mainly consisting of calcite. This provides a good basis for modelling the seismic properties of a carbonate reservoir, as the mineralogy is fairly clean.

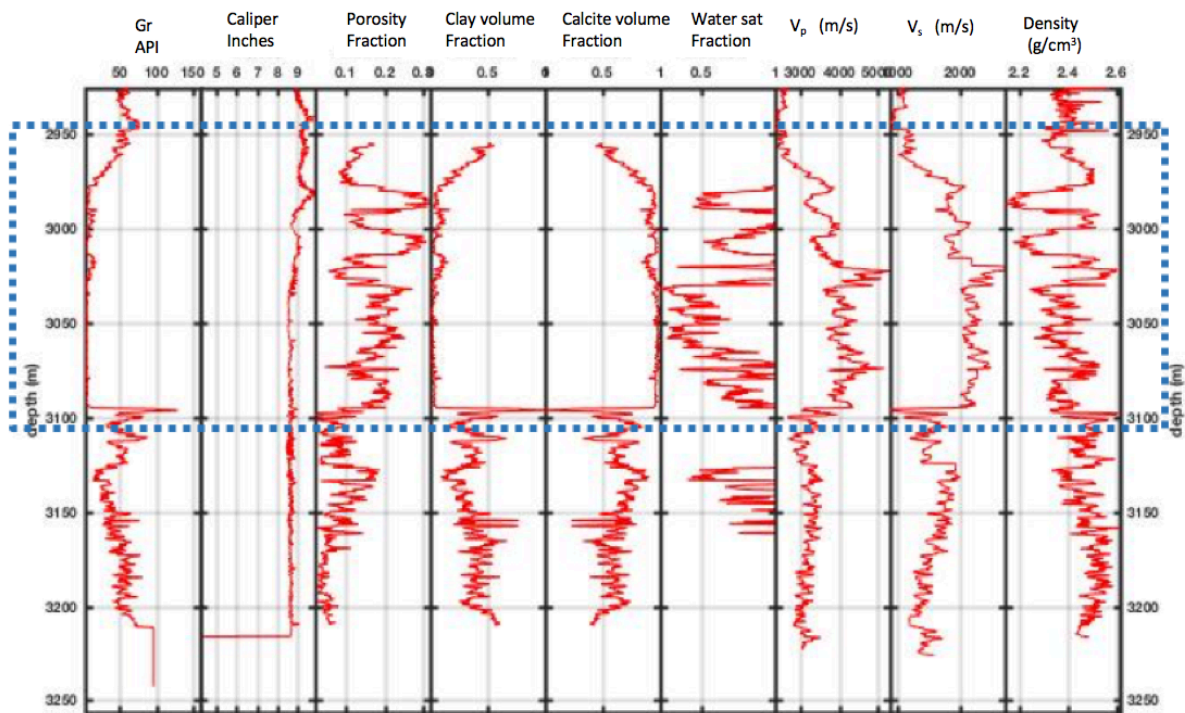


**Figure 5.1.** The figure is showing logs from a well in the North Sea. The blue stippled zone represents a chalky reservoir interval.

### 5.1 Data Preparations

Calibrations of the model parameters against the provided data set is performed in to ensure good correlation between the well data and the input parameters used in the modelling. The calibrations are performed on the density, bulk modulus and shear modulus of the reservoir. These parameters are sufficient to describe the seismic properties of the reservoir zone.

### 5.1.1 Fabric Properties

The input parameters describing the properties of the constituent minerals are calculated using rock physics models. The values are adapted to fit the well data through calibrations. Figure 5.2 illustrates the calibration results through a cross-plot between data and model properties.

The density of a rock is the arithmetic average of the constituent mineral densities. In preparation for the modelling, the density is calibrated using the friable sand model. Calibration of the bulk and shear modulus depend on the composition of the rock and general reservoir properties as pressure and temperature. The Kite-model is applied to calculate the modelled elastic moduli to be compared with the well data. This model combines both cement and crack modelling (Avseth et al., 2014).

The density, bulk and shear modulus of the mineralogical properties are adapted from Japsen et al. (2004), which considers a chalk field in the North Sea. They are calibrated to ensure the best possible fit to the provided well data. As the reservoir zone is pure calcite, the clay values are not of great importance in this modelling. The clay values are adapted from Mavko et al. (2009).

A pore geometry model is created, describing the initial rock fabric. The aspect ratios used in the modelling are defined by Xu and Payne (2009). Cracks are represented as pores with aspect ratio 0.02, intergranular pores with aspect ratio 0.15 and spherical pores with aspect ratio 0.80. The aspect concentration of the initial rock is defined through calibrations. Table 5.1 provides an overview over the values used in the modelling.

### 5.1.2 Pore-pressure and Temperature

Temperature and pore-pressure are reservoir parameters included in the modelling. They are especially important in relation to the fluid properties. The temperature at the target depth is calculated using an approximate geothermal gradient of 30°C/km (Harper, 1971). The reservoir zone is at approximately 3 km depth, giving a temperature of 90°C.

The pore-pressure is assumed to be normal, meaning that it is equal to the hydrostatic pressure. This assumption indicates that the pore space is open, and the fluids can flow freely. The pore-pressure is calculated using the brine density ( $\rho_b$ ), gravitational acceleration ( $g$ ) and depth ( $z$ ) of the reservoir:

$$P_p = \rho_b g z , \quad (5.1)$$



Using a brine density of  $1100 \text{ kg/m}^3$ , gravitational acceleration of 10 (for simplicity) and depth of 3000 meters gives an hydrostatic pressure of 33 MPa (Thomas Hantschel and Kauerauf, 2009). The water salinity at this density and temperature is set to approximately 0.2 (Oldenburg and Rinaldi, 2011).

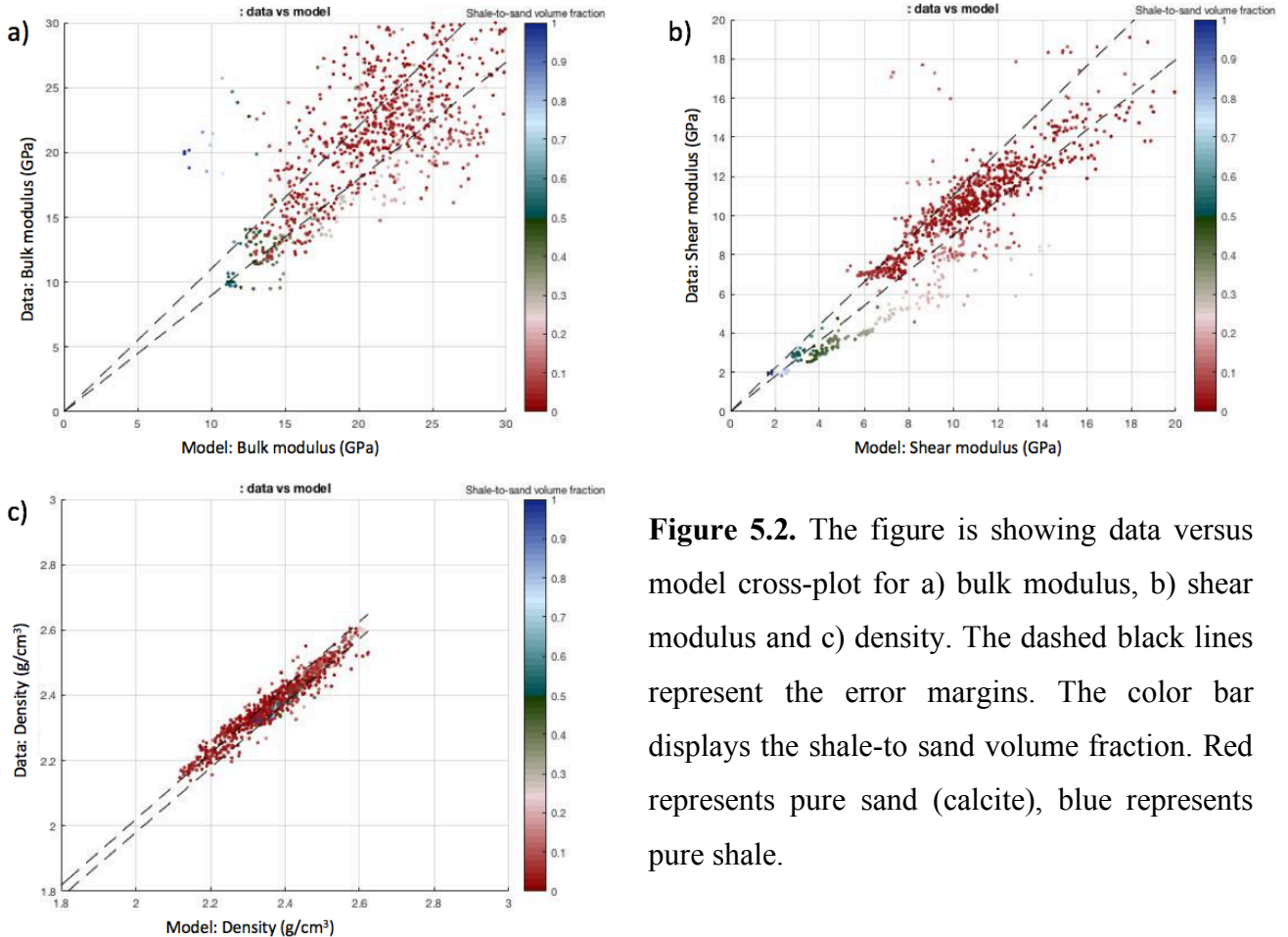


**Figure 5.2.** The figure is showing data versus model cross-plot for a) bulk modulus, b) shear modulus and c) density. The dashed black lines represent the error margins. The color bar displays the shale-to sand volume fraction. Red represents pure sand (calcite), blue represents pure shale.

<b>Bulk Calcite</b>	73 (MPa)
<b>Shear Calcite</b>	40 (MPa)
<b>Density Calcite</b>	2.71 (g/cm <sup>3</sup> )
<b>Bulk Clay</b>	9.5 (MPa)
<b>Shear Clay</b>	3 (MPa)
<b>Density Clay</b>	2.45 (g/cm <sup>3</sup> )
<b>Aspect ratio</b>	[0.80 0.15 0.02]
<b>Aspect concertation</b>	[0.70 0.26 0.04]

**Table 5.1.** The table presents the modelling input parameters modified form Japesen et al., (2004); Mavko et al., (2009).

### 5.1.3 Fluid Substitution

Injections of CO<sub>2</sub> in saline aquifers are suggested as a solution to reduce the concentration of atmospheric CO<sub>2</sub>. The well data provided for this thesis is saturated with brine and hydrocarbons. A new brine-saturated log is therefore created using the Gassmann fluid substitution model. This is to simulate the properties of a brine saturated reservoir. The solid rock properties are found through calibrations. Information regarding porosity and clay volume is obtained from the provided well data. The mineralogical input parameters are described in Table 5.1. Gassmann modelling is used to replace the initial pore fluids with brine. The new log is now 100% brine saturated. The brine properties at the reservoir temperature and pore-pressure is based on empirical relations by Batzle and Wang (1992).

The same procedure was performed to create a 100% CO<sub>2</sub> saturated log. The CO<sub>2</sub> properties at the reservoir temperature and pore-pressure is based on Span and Wagner's (1996) equation of state.

Figure 5.3 shows the new logs created using rock physics models. The logs now represent a reservoir saturated with fluids consisting purely of brine and CO<sub>2</sub>. These logs are used in the modelling of the seismic effects following rock-fluid interaction.

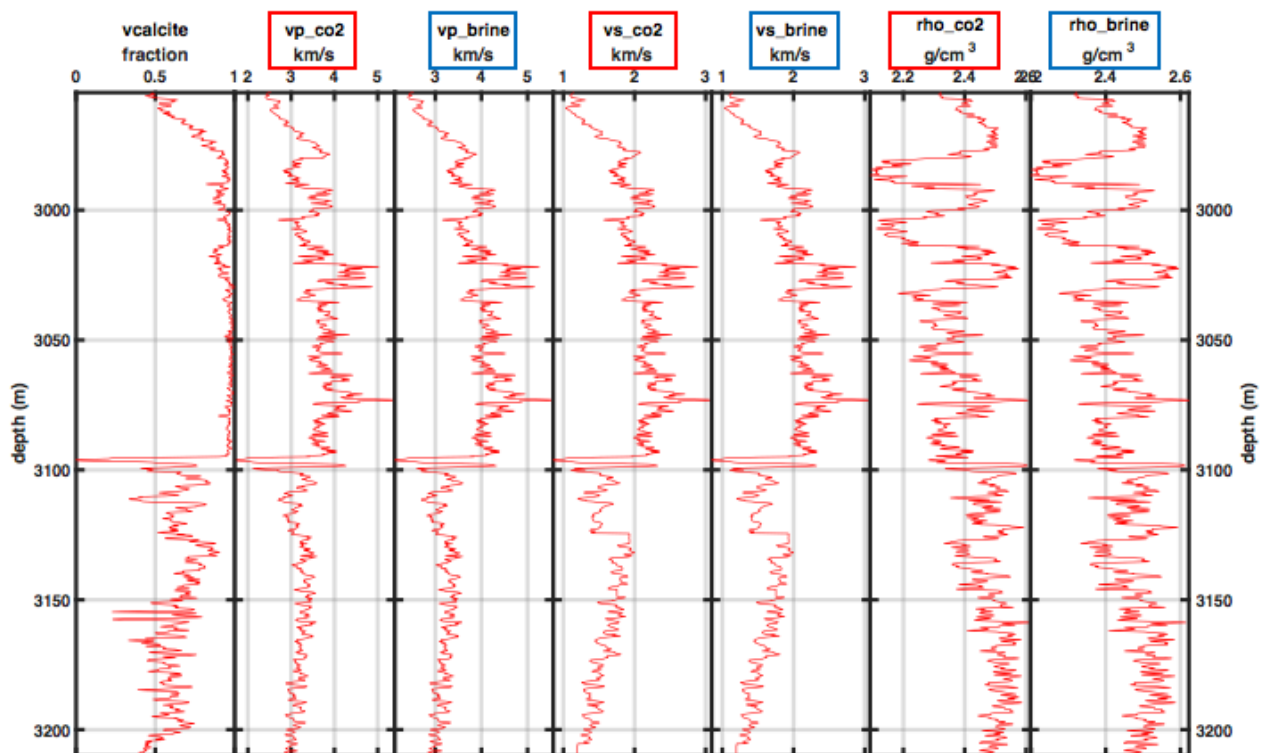


**Figure 5.3.** The figure is showing the new logs created for brine and CO<sub>2</sub> saturated chalk reservoir.

## 5.2 Modelling the Effects of Geochemical Interactions

Synthetic seismic logs are created for a set of geochemically induced scenarios, describing the response to the rock-fluid interactions. A total set of four scenarios are defined based on experiments described in literature (Grombacher et al., 2012; Luquot and Gouze, 2009; Vanorio et al., 2011; Vanorio, 2015).

For each scenario, a set of aspect ratios ( $\alpha$ ) and aspect concentrations ( $c(\alpha)$ ) are defined to represent a variation of pore shapes. Spherical-like pores have aspect ratio of 0.8, intergranular pores have aspect ratio 0.15 and cracks have aspect ratio 0.02 (Xu and Payne, 2009). An initial aspect concentration is defined through model calibrations.

The Kite model is used to model the geochemical effect on the carbonate rock fabric. To describe the alterations occurring in the rock frame, the aspect concentrations, porosity and pore-pressure are changed to fit the described scenario. All other parameters are fixed. The effect of different fluid saturations is incorporated in the model using Gassmann fluid substitution in each step.

### 5.2.1 Defining the Scenarios

Based on literature and experiments, four different scenarios are created to demonstrate the possible effect of CO<sub>2</sub> injections on carbonate reservoirs. The experimental results are described in chapter 4. Each scenario is divided into four stages, where the variations in the fabric properties occur due to the rock's response to the injected fluid:

0. The initial rock, saturated with brine.
1. The initial rock, saturated with CO<sub>2</sub>.
2. Geochemically induced alterations as a response to CO<sub>2</sub> injections.
3. The effect of compaction.

#### *Scenario 0*

Scenario 0 (S0) represents a pure fluid substitution scenario. Here, no rock-fluid interactions are considered. As a result, no variation in porosity or pore shapes are evaluated. Figure 5.3 demonstrates the different stages of scenario 0. The blue dots represent brine saturated pores, the red dots represent the CO<sub>2</sub> saturated pores.

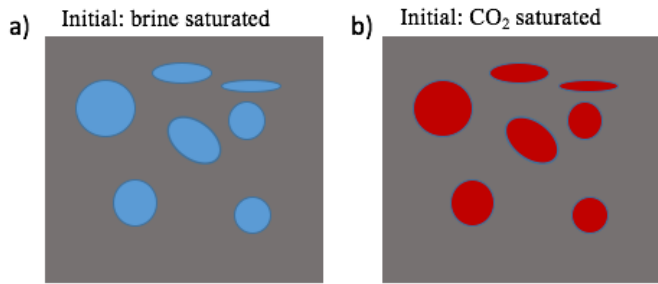


**Figure 5.3.** The figure is showing the two stages of scenario 0, where a) is the brine saturated rock and b) is the CO<sub>2</sub> saturated rock. No rock-fluid interactions are considered.

### *Scenario 1*

Scenario 1 (S1) represents the effect of injecting CO<sub>2</sub> into a tight, carbonate reservoir. The acidic solution reacts with the rock fabric according to the experimental results discussed in section 4.3.1. The stages of scenario 1 is presented in Figure 5.4, which shows:

- Dissolution target the pore geometry and increase the concentration of cracks.
- The porosity is left unaltered.
- Compaction will increase the concentration of cracks (on the expense of intergranular pores) and induce over-pressure.

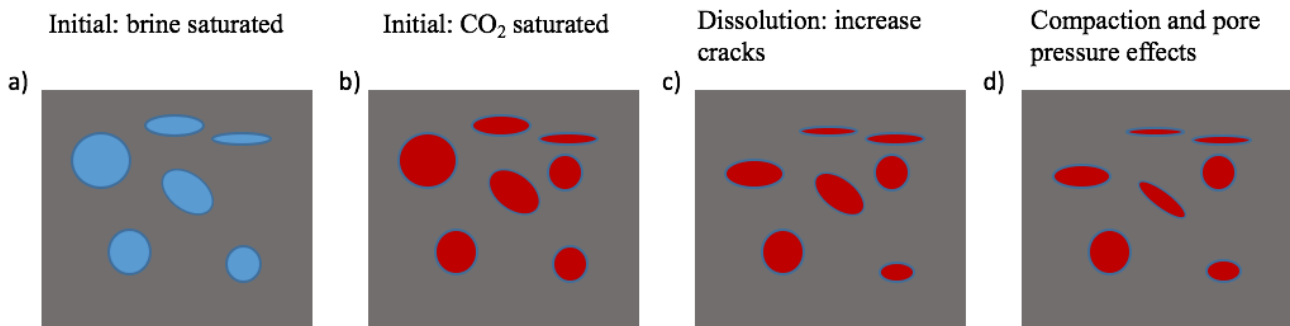


**Figure 5.4.** The figure is showing the various stages of scenario 1, a) brine saturated rock (S1.0), b) CO<sub>2</sub> saturated rock (S1.1), c) dissolved rock with increased concentration of cracks (S1.2) and d) compacted rock with increased pore-pressure and cracks (S1.3).

### *Scenario 2*

Scenario 2 (S2) represents the effect of injecting CO<sub>2</sub> into a granular, carbonate reservoir. The acidic solution reacts with the rock fabric according to the experimental results discussed in section 4.3.1. The stages of scenario 2 is presented in Figure 5.5, which shows:

- Dissolution target the pore volume, increasing the porosity by 5%.
- The pore geometry is unaltered.

- Compaction will induce a higher concentration of cracks (on the expense of intergranular pores) and over-pressure.

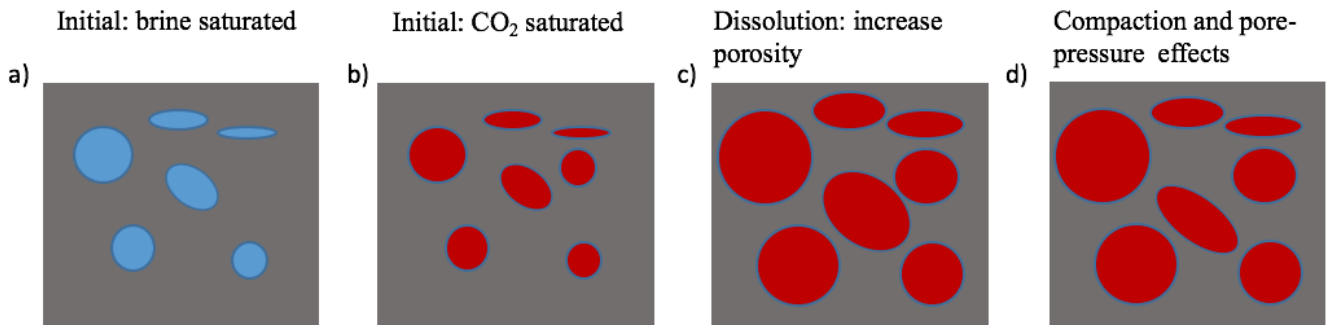


**Figure 5.5.** The figure is showing the various stages of scenario 2, a) brine saturated rock (S2.0), b) CO<sub>2</sub> saturated rock (S2.1), c) dissolved rock with increased concentration of cracks (S2.2) and d) compacted rock with increased pore-pressure and cracks (S2.3).

### *Scenario 3*

Scenario 3 (S3) represents the effect of precipitation occurring some time after the CO<sub>2</sub> injections. The process is described in section 4.4. Precipitation normally occurs in the pore-throats, which are usually represented by the elastic properties of low-aspect ratio pores (Pan et al., 2015). This effect reduces the concentration intergranular pores. The stages of scenario 3 is presented in Figure 5.6, which shows:

- Precipitation target the pore throats, reducing the porosity by 5%.
- The concentration of spherical-like pores increase, as the pore throats are clogged.
- The clogging of the pore throats will induce increased pore pressure.

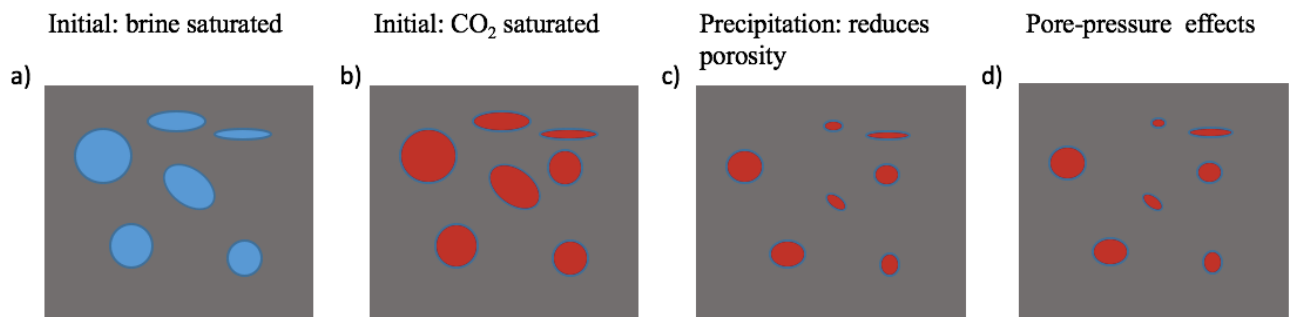


**Figure 5.6.** The figure is showing the various stages of scenario 3, a) brine saturated rock (S3.0), b) CO<sub>2</sub> saturated rock (S3.1), c) precipitated rock with reduced porosities (S3.2) and d) increased pore-pressure due to clogging of pore-throats (S3.3).

Table 5.2 provides an overview over all the aspect concentrations used to model the fabric response to the geochemically induced alterations. Note that in scenario 2 and 3, the porosity is increased and reduced by 5% respectively. The red numbers represent altered aspect concentrations.

	Scenario 0	Scenario 1	Scenario 2	Scenario 3
$\alpha$	[0.80 0.15 0.20]	[0.80 0.15 0.20]	[0.80 0.15 0.20]	[0.80 0.15 0.20]
$c(\alpha)$ : Stage 0	[0.70 0.26 0.04]	[0.70 0.26 0.04]	[0.70 0.26 0.04]	[0.70 0.26 0.04]
$c(\alpha)$ : Stage 1	[0.70 0.26 0.04]	[0.70 0.26 0.04]	[0.70 0.26 0.04]	[0.70 0.26 0.04]
$c(\alpha)$ : Stage 2	[0.70 0.26 0.04]	[0.50 0.43 0.07]	[0.70 0.26 0.04]	[0.80 0.199 0.001]
$c(\alpha)$ : Stage 3	[0.70 0.26 0.04]	[0.50 0.20 0.30]	[0.70 0.10 0.20]	[0.80 0.199 0.001]

**Table 5.2.** The table provides information about the aspect ratios ( $\alpha$ ) and aspect concentrations ( $c(\alpha)$ ) of the defined scenarios. Stage 0 represents the initial rock, stage 1 represents the CO<sub>2</sub> saturated rock, stage 2 represents the rocks repose to the CO<sub>2</sub> injections and stage 3 represents the effect of compaction and increasing pore-pressure. The aspect concentrations experiencing alterations are marked in red.

### 5.3 Amplitude Versus Angle Modelling

Synthetic AVA-gathers are created using the well logs generated for each scenario. The software used to perform this modelling is Hampson-Russel. Two synthetic AVA gathers are created for each scenario using the velocity and density log of the scenario in question. The gathers are generated using two different Ricker wavelets; one with a peak frequency of 20 Hz, and one with a peak frequency of 40 Hz. The two wavelets are illustrated in Figure 5.7. No geometrical spreading or attenuation is assumed in the modelling. The angles are varied between 0 and 45 degrees.

Synthetic reflectivity logs are generated in MATLAB, using the velocity and density logs of the scenario in question (the equations for P- and S-reflectivity described in section 3.6.2). The reflectivity logs are then used to generate synthetic gradient logs for each scenario.

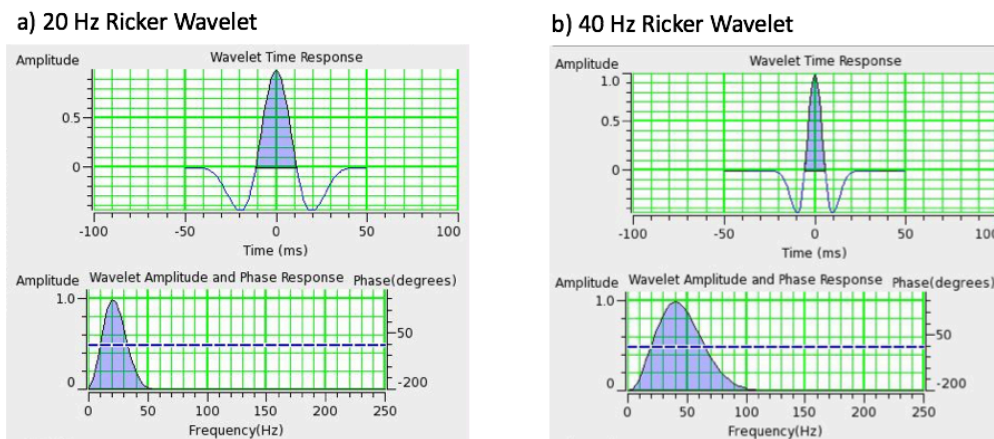


**Figure 5.7.** The figure shows the Ricker wavelets used in the AVA modelling. a) 20 Hz peak frequency, b) 40 Hz peak frequency.

#### 5.4 Applicability of the Various Rock Physics Models

A possible source of error when performing rock physics modelling is related to the assumptions underlying the model itself. Determining the appropriate rock physics model is restricted by its validity under specific conditions (Wang, 1997).

The applicability of the Gassmann model on carbonate reservoirs have been discussed by various authors, and is evaluated in section 3.4.1. As an example, Baechle et al. (2005) questions whether the result of constant shear modulus is valid for carbonate rocks. For practical reasons, the Gassmann fluid substitution model is used to model the saturation effects. As the Kite model considers the alterations occurring in the rock fabric following rock-fluid interactions, the implementation of Gassmann equations only models the effect of various fluid saturations. Thus, alterations in shear modulus of the rock frame is included in the model.

Further, the applicability of the Kite model on carbonate rocks can be evaluated. The low porosity interval is modelled using DEM, which is based on the K-T model, assuming isolated pores (Mavko et al., 2009). However, through higher order scattering, pore-to-pore interaction is also taken into consideration using DEM theory. This creates a good basis for modelling of the dry rock properties in the low-porosity interval, as carbonate pore systems can be both isolated and connected. Similar modelling techniques have been applied to model the effect of micro pores in carbonates by for example Xu and Payne (2009). The high-porosity end-member is modelled using cemented granular medium models. A similar modelling strategy for carbonate reservoirs have been successfully applied by Afif and Dvorkin (2016). Thus, the Kite model should be a reasonable modeling approach for the dry rock properties.

An additional modelling problem is related to the challenges of creating a valid rock model. A good rock physics model should be consistent with the available well data. Creating a rock model that is not comparable with the provided data is a possible source of misinterpretation. To address this problem, thorough model calibrations should be performed to ensure best possible fit between data and model.

In addition, it is important to be aware that synthetic data does not necessarily relate to a real data set. The modelled AVA response in this thesis does not consider attenuation or geometrical spreading. As the subsurface is complex, different factors may contribute to scattering or attenuation of the seismic waves. Thus, by assuming that no energy loss occurs, the representation of the seismic data may be somewhat unrealistic.



## 6 Results and Analysis

In the following chapter, the results of the modelling will be presented and analyzed. The main purpose is to explore the effects of fluid substitution and alterations in the rock fabric on the seismic response. As the reservoir consists of relatively pure calcite, there is expected little variation in the seismic properties due to mineralogical effects. However, throughout this chapter, the effect of pore shape, porosity and pore fluid will be studied. Variations in the following parameters will be evaluated for all scenarios:

- Elastic properties and density
- Seismic velocities
- Rock physics template
- AVA response

### 6.1 The Effect of Porosity, Pore Shape and Saturation on the Seismic Properties

The general effect of porosity, pore shape and saturation on the seismic properties is modelled using the Kite model. The input parameters describe a theoretical calcite rock, and are found in Table 5.1. Figure 6.1 demonstrates the effect of porosity, pore-shape and saturation on seismic properties, using this rock model.

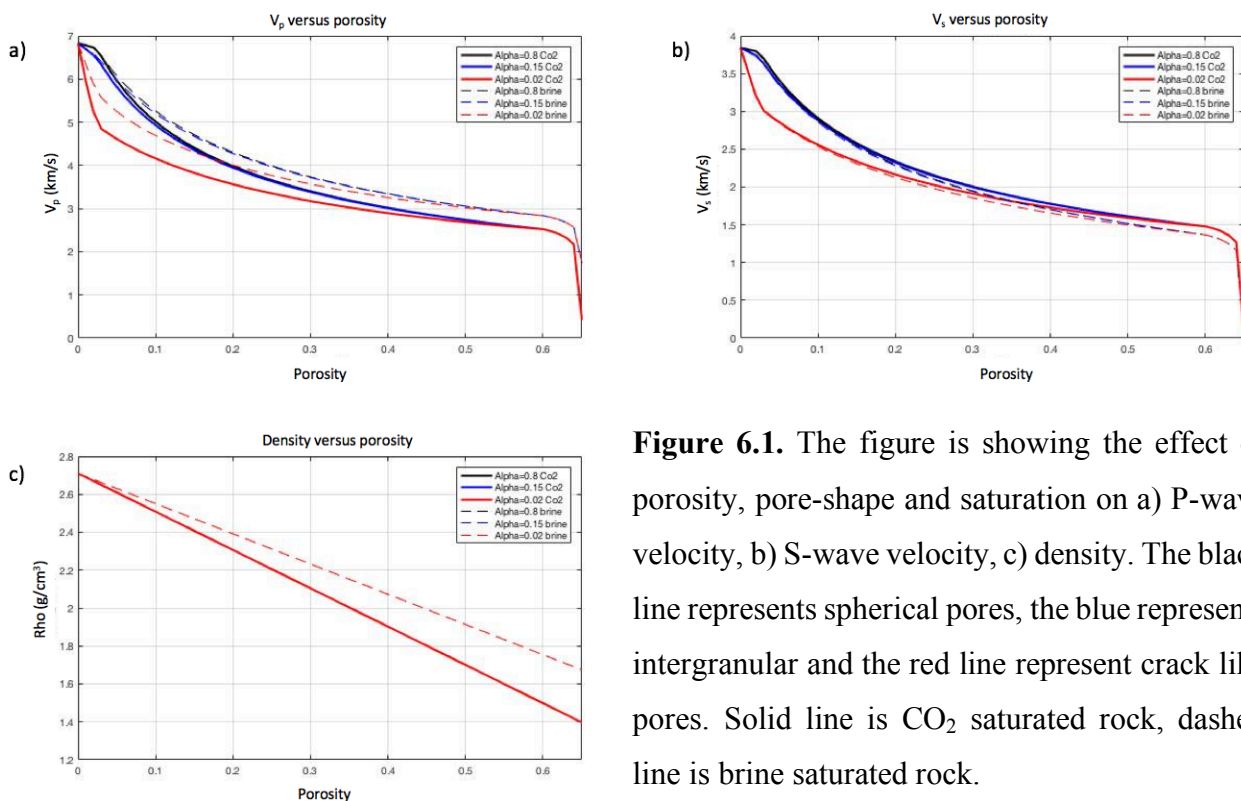


**Figure 6.1.** The figure is showing the effect of porosity, pore-shape and saturation on a) P-wave velocity, b) S-wave velocity, c) density. The black line represents spherical pores, the blue represents intergranular and the red line represent crack like pores. Solid line is CO<sub>2</sub> saturated rock, dashed line is brine saturated rock.

In Figures 6.1a and 6.1b the seismic velocities are plotted against porosity for various pore shapes and fluid saturations. The trend is that the velocity is reduced as the porosity increase and the aspect ratio decrease. A rock containing spherical pores will hold higher velocity at a given porosity than a rock containing crack-like pores.

The effect of pore fluid on the seismic velocities is included by modelling the velocity trend for brine and CO<sub>2</sub> saturated rocks. The dashed lines represent the velocity of a brine saturated rock, whereas the solid lines represent the velocity of a CO<sub>2</sub> saturated rock. For a given pore shape and porosity, the brine saturated rock holds higher P-wave velocity than the CO<sub>2</sub> saturated rock. The S-wave velocity in Figure 6.1b does however demonstrate a slightly higher velocity in CO<sub>2</sub> saturated rock compared to the rock saturated with brine. The fluid effect is not as obvious on S-wave compared to P-wave velocity.

The effect of pore shape on the seismic velocities is evaluated by including a velocity model for a rock containing 100% cracks (red line), intergranular (blue line) and spherical (black line) pores. Spherical pores hold higher velocities than both intergranular pores and cracks. It is obvious that the pore shapes contribute to variations in velocity over the same porosity. The contrast in properties for various pore shapes decrease as the porosity increase. Also, the fluid sensitivity is higher for low aspect ratio pores than for the spherical pores.

Figure 6.1c demonstrates the effect of porosity, pore shape and pore fluid on the rock density. As the porosity increase, the density decrease. The pore shape has no effect on the density of the rock, whereas the pore fluid contributes to density alterations. The density is higher for the brine saturated rock than for CO<sub>2</sub> saturated rock.

In the following sections, more detailed modelling will be performed, to investigate the seismic effects caused by rock-fluid interaction.

## **6.2 Scenario Zero: The Effect of Fluid Substitution**

Scenario 0 represents the effect of fluid substitution alone. Table 6.1 summarizes the expected variation in the rock fabric of the carbonate rock. Information regarding scenario 0 is provided in section 5.2.1. Table 5.2 displays the aspect ratios and aspect concentrations used in the modelling. Note that these results represent the two first stages in all the following modelling of the various scenarios. Thus, in all future scenarios, the effect of fluid substitution will not be evaluated in detail, as it is presented in the following sections.

	$\Delta\phi$	Cracks	Spherical pores	Intergranular pores	Dissolved carbonate minerals in pore fluid
<b>Initial <math>P_p</math></b>	0	0	0	0	0
<b>Increased <math>P_p</math></b>	0	0	0	0	0

**Table 6.1.** The table summarizes the effect of fluid substitution in scenario 0. In the table, 0 means that no alterations in the rock frame are expected.

### 6.2.1 Elastic Properties and Density

Information regarding the elastic properties is useful for understanding the variations in the seismic responses occurring in the reservoir zone. This section will evaluate the modelled effect on the elastic properties following fluid substitution in a chalky reservoir. The blue line in Figure 6.2 represents the moduli and density of the initial reservoir, saturated with brine. The red line is the moduli and density of the CO<sub>2</sub> saturated reservoir.

The effect of fluid substitution on bulk and shear modulus is demonstrated in Figures 6.2a and 6.2b respectively. The bulk modulus of a CO<sub>2</sub> saturated reservoir is lower than that of a brine saturated reservoir. As fluids have no shear strength, the pore fluid of the reservoir will exhibit no effect on the reservoir shear modulus.

At the given reservoir pressure and temperature, CO<sub>2</sub> holds lower density than brine. Thus, by changing the pore fluid from brine to CO<sub>2</sub>, a reduction in the density of the reservoir zone is observed (Figure 6.2c).

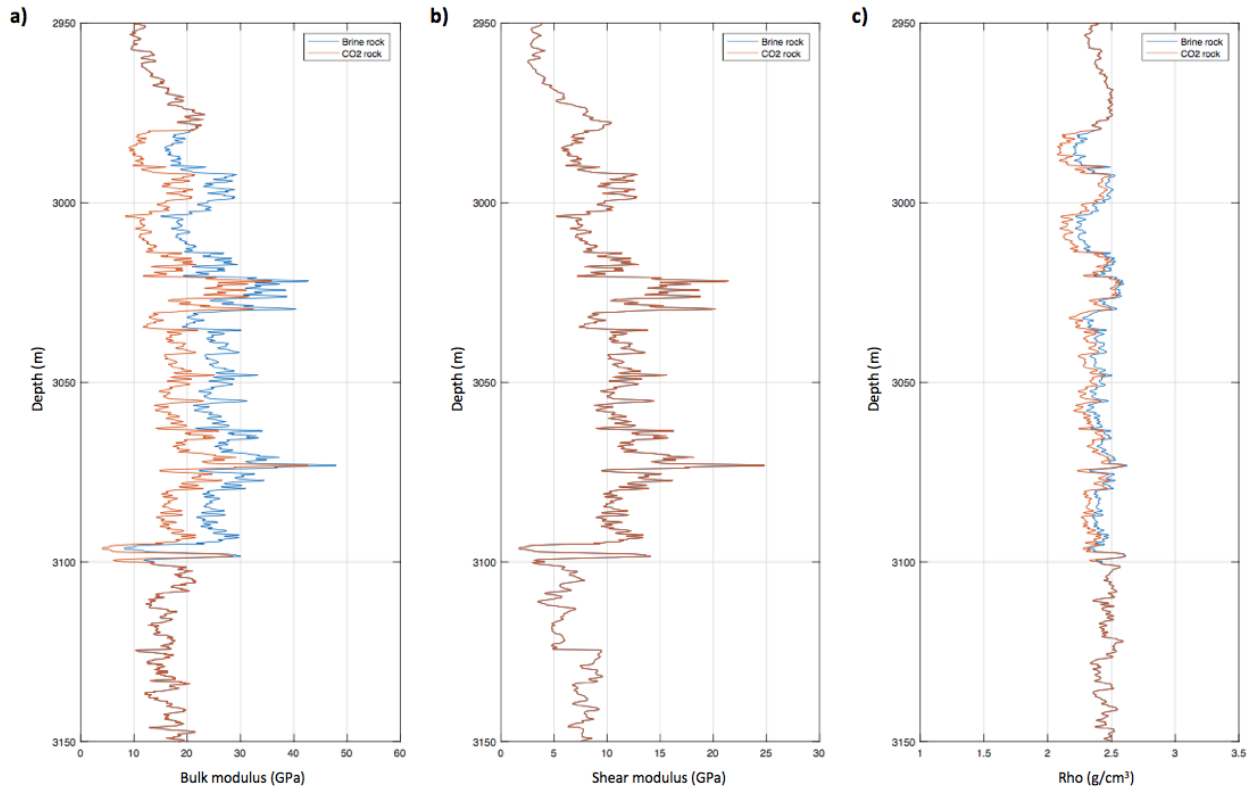


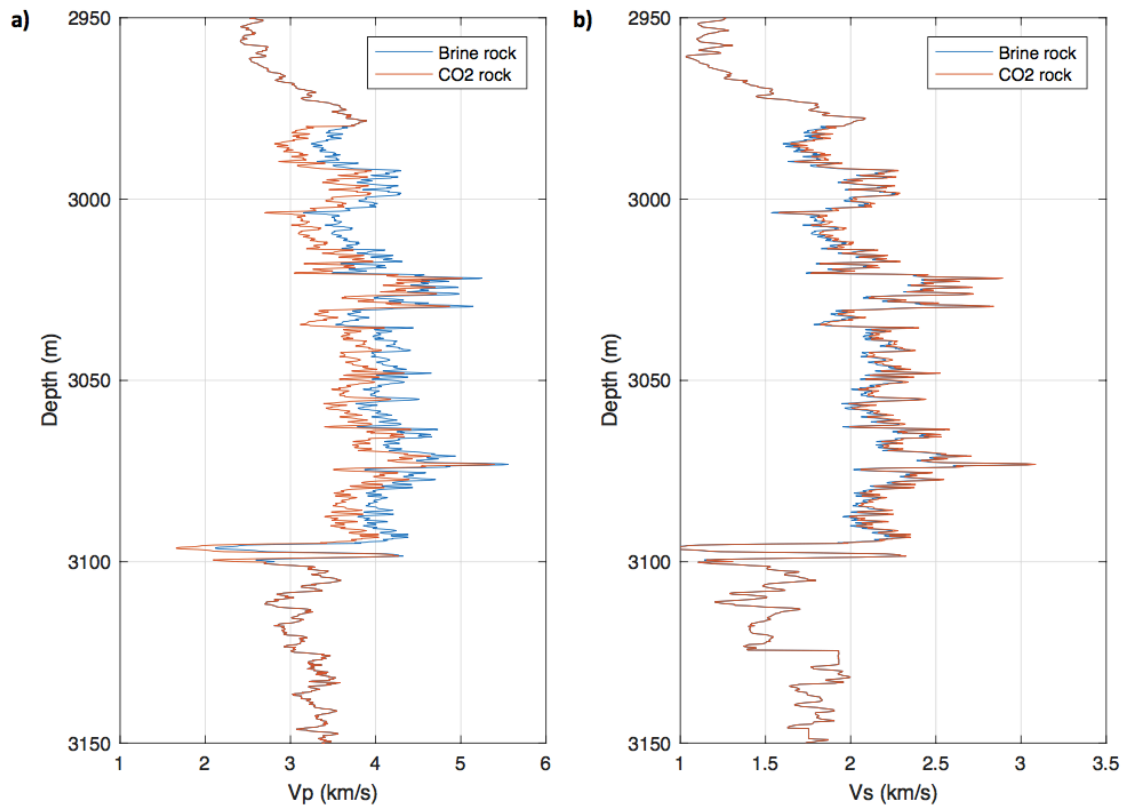
**Figure 6.2.** The figure shows the effect of fluid substitution on a) bulk modulus, b) shear modulus and c) density. The blue line represent the brine saturated properties, the red line represents the CO<sub>2</sub> saturated properties.

### 6.2.2 Seismic Velocity and Acoustic Impedance

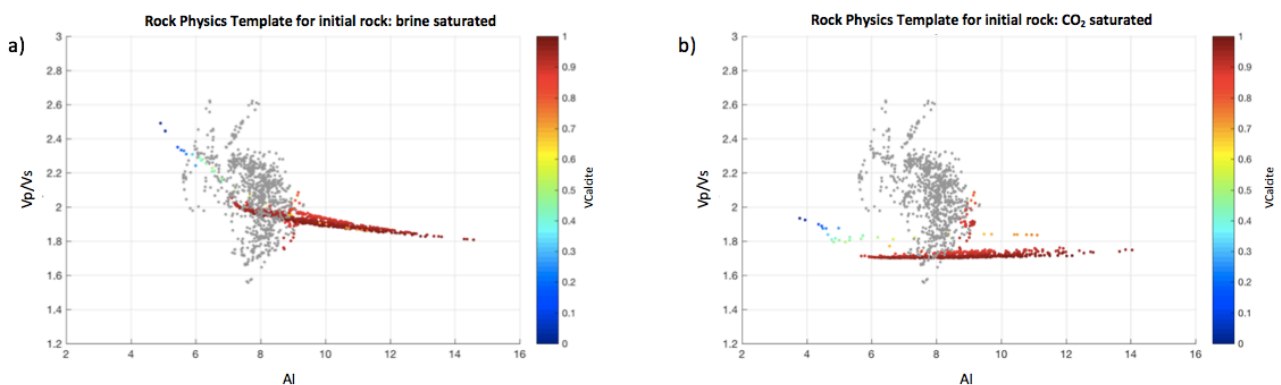
The modelled variations in the elastic properties discussed in the section above, will affect the seismic velocity of the saturated reservoir (see Equations 3.1 and 3.3). The effect of fluid substitution on the P- and S-wave velocity is plotted in Figure 6.3. The P-wave velocity is lower for a reservoir saturated with CO<sub>2</sub> compared to brine. The S-wave velocity does however display a slight increase as brine is replaced by CO<sub>2</sub>. These observations can be traced back to the alterations occurring in the elastic properties following the fluid substitution. The reduction in P-wave velocity is dominated by the lowering of the bulk modulus. The reduced density dominates the S-wave velocity as fluid substitution shows no effect on the shear modulus. This explains the slight increase in the S-wave velocity as brine is substituted with CO<sub>2</sub>.

Figure 6.4 displays the rock physics template for scenario 0, where the reservoir data is plotted as a function of calcite content. The rest of the data set is plotted in gray. Figure 6.4a shows the rock physics template of the initial rock, saturated with brine, whereas the CO<sub>2</sub> saturated rock is displayed in Figure 6.4b. Comparing the two figures demonstrate the effect of

fluid substitution on the acoustic impedance and velocity ratio. As the less dense CO<sub>2</sub> replaces brine, both the velocity ratio and acoustic impedance is reduced.



**Figure 6.3.** The figure displays the variations due to fluid substitution on a) P-wave velocity and b) S-wave velocity. The blue line represents the velocity of the brine saturated rock, whereas the red line represents the CO<sub>2</sub> saturated rock.



**Figure 6.4.** The figure shows the rock physics template of scenario 0 for a) the initial, brine saturated rock, b) CO<sub>2</sub> saturated rock. The reservoir data is plotted as a function of calcite content; the remaining data is plotted in gray.

### 6.2.3 Amplitude Versus Angle Response

AVA analysis can be used as an additional tool in fluid detection and reservoir monitoring. In this section, the variations in the AVA response and properties due to fluid substitution will be evaluated.

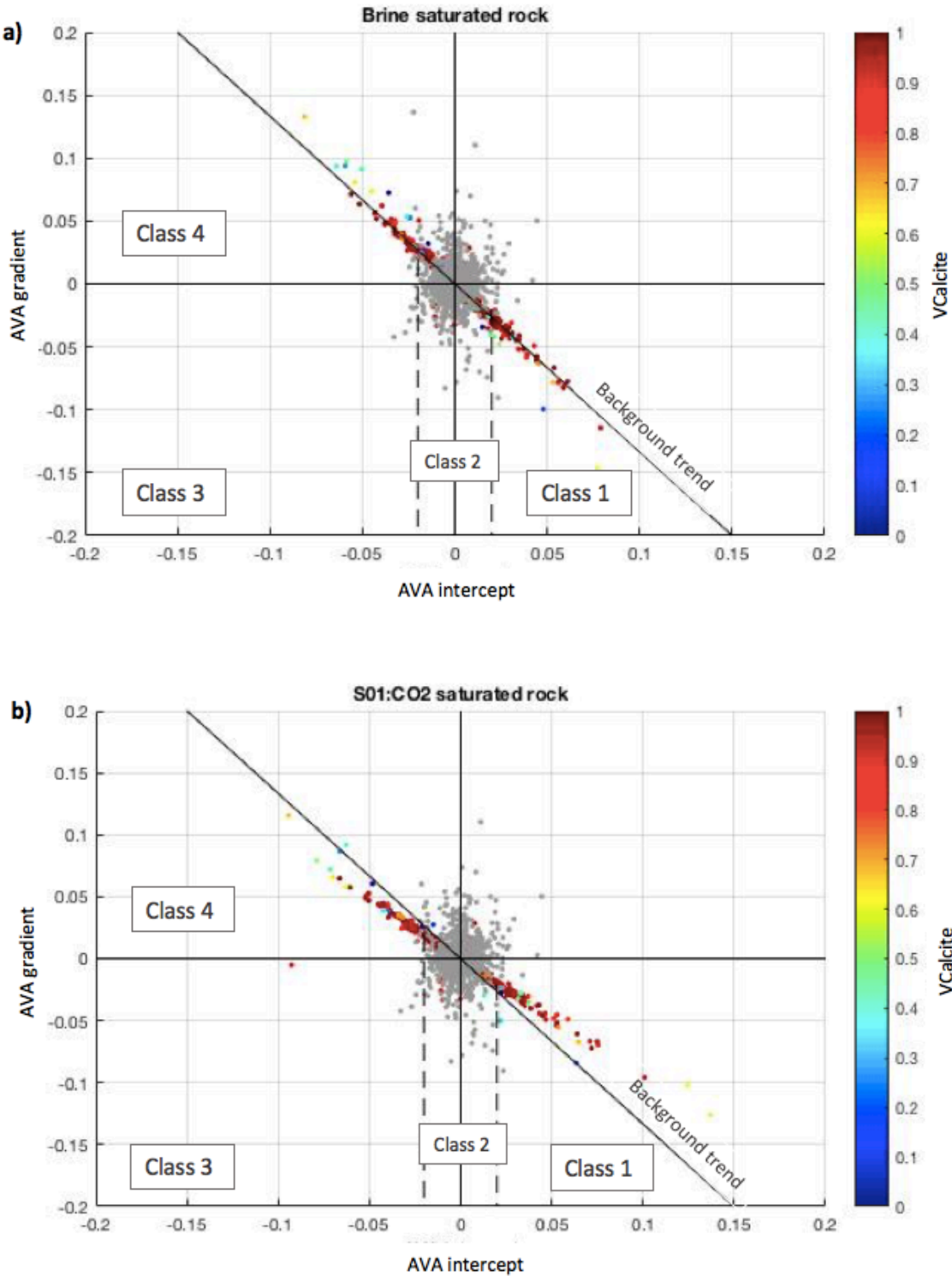
The intercept versus gradient cross plots for the chalky reservoir is illustrated in Figure 6.5. Here, the four classes and background trend are based on Castagna and Chopra's (2014) AVO cross plot. The reservoir data is plotted as a function of calcite content, and the remaining data is plotted in gray.

Figure 6.5a displays the brine saturated cross plot, where the reservoir data plot on the background trend. The cross plot for the CO<sub>2</sub> saturated reservoir is presented in Figure 6.5b, and displays a deviation from the background trend. Now positive gradients plot at less positive values, whereas the negative gradients plot at less negative values.

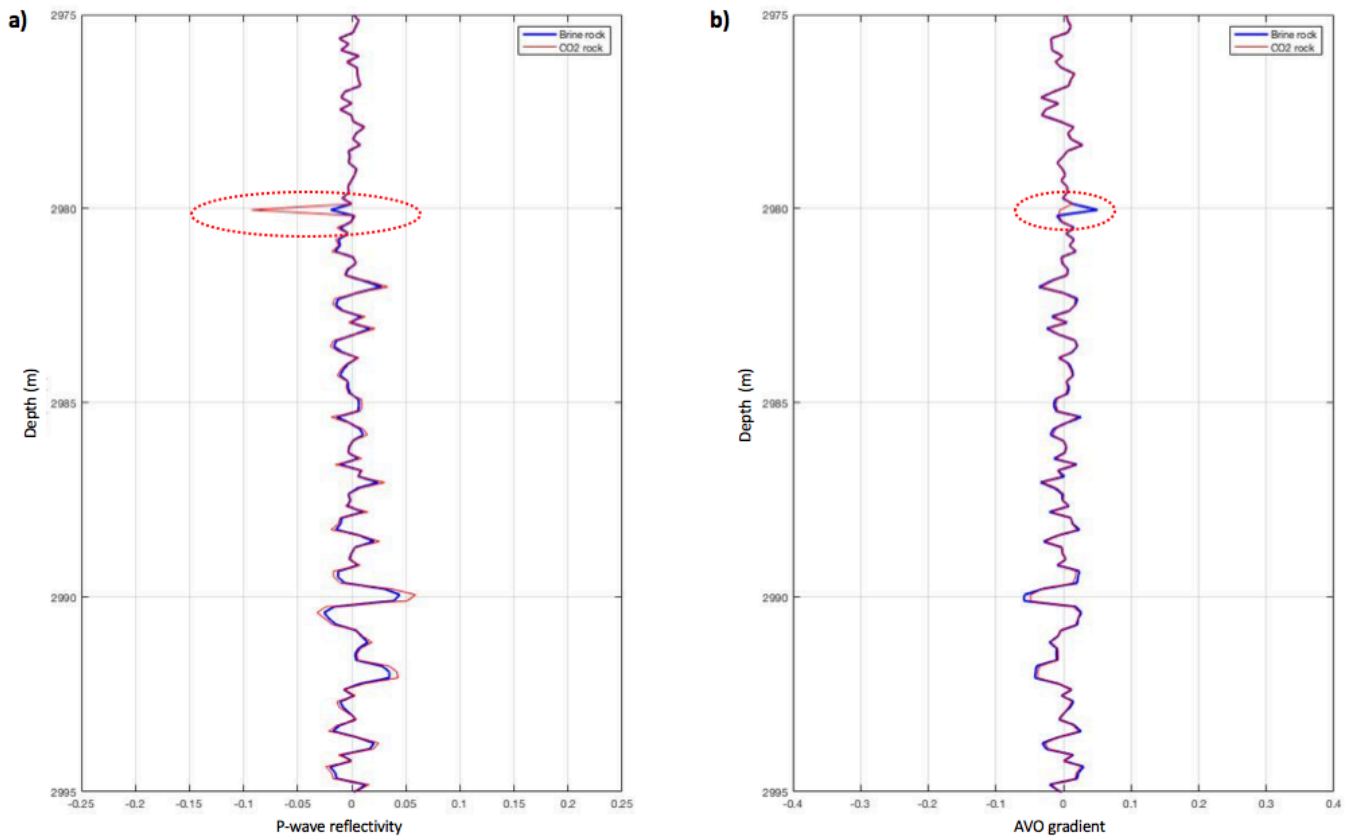
Figure 6.6 displays the calculated P-wave reflectivity and gradient using the modelled well data describing scenario 0. It provides a general overview of the alterations induced by fluid substitution. The brine reservoir is marked by a blue line, whereas the CO<sub>2</sub> reservoir is marked by a red line.

Figure 6.6a demonstrates that the reflectivity of the CO<sub>2</sub> saturated reservoir generally is stronger than the reflectivity in the brine saturated reservoir. This will induce stronger amplitudes as brine is substituted by CO<sub>2</sub>. The calculated AVA gradient of the brine saturated reservoir is somewhat stronger compared to the gradient of the CO<sub>2</sub> saturated reservoir, illustrated in Figure 6.6b.

Figure 6.9 displays a synthetic AVA gather for Scenario 0, modelled using a Ricker wavelet with a peak frequency of 40 Hz. The amplitudes of the CO<sub>2</sub> saturated gather b) is stronger compared to the amplitudes of the brine saturated gather a). In addition to affecting the strength of the amplitude and the AVA gradient, fluid substitution also affects the travel time of the seismic waves. Comparing the reflectors in each gather, a time shift is revealed, caused by the fluid replacement. The apparent location of the reflectors in the CO<sub>2</sub> saturated rock appears at longer travel times compared to the brine saturated rock. The red arrow marks the time shift in one of the reflectors, which is more visible in the deeper part of the reservoir.



**Figure 6.5.** The figure shows the intercept-gradient cross plot for a) brine saturated rock and b) CO<sub>2</sub> saturated rock. The reservoir data is plotted as a function of calcite content; the remaining data is plotted in gray.



**Figure 6.6.** The figure compares a) the P-wave reflectivity and b) AVO gradient for scenario 0. The blue line represents the brine saturated reservoir, whereas the red line represents the CO<sub>2</sub> saturated reservoir. The red circle marks an anomaly from the brine saturated log.

A more detailed AVO modelling was performed in the top of the reservoir. The target reflector is marked by the red line in Figure 6.9. This zone also represents an anomaly in Figure 6.6, where it is marked by a red circle. The variation in gradient and intercept following fluid substitution is displayed in Figure 6.7. Here, the gradient of the brine saturated rock is more positive compared to the CO<sub>2</sub> saturated rock. The intercept value demonstrates the zero angle reflectivity, which is more negative for the CO<sub>2</sub> saturated rock compared to the brine saturated rock.

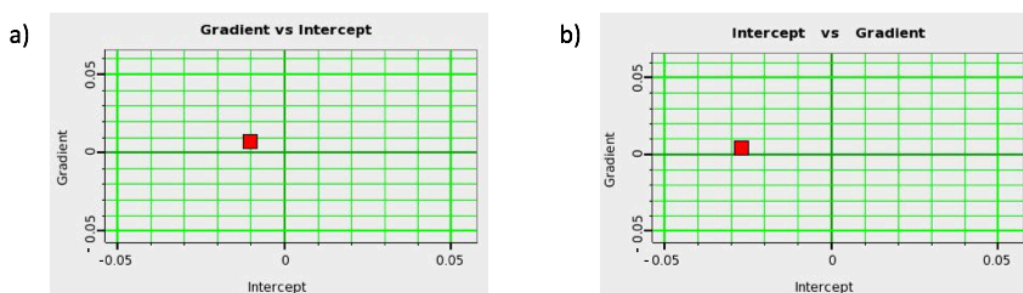


**Figure 6.7.** The figure shows the gradient and intercept for top reservoir in scenario 0 (40 Hz wavelet), a) initial rock, b) CO<sub>2</sub> saturated rock (S0.1).



To demonstrate the effect of the wavelet used in the modelling, an additional synthetic gather is created, using a Ricker wavelet with peak frequency of 20 Hz (Figure 6.10). The variation in gradient and intercept following fluid substitution is displayed in Figure 6.8, which represents the zone marked by a red line in Figure 6.10. Here, the brine saturated rock displays a positive gradient while the CO<sub>2</sub> saturated rock displays a negative gradient. The intercept value is more negative for the CO<sub>2</sub> saturated rock compared to the brine saturated rock.

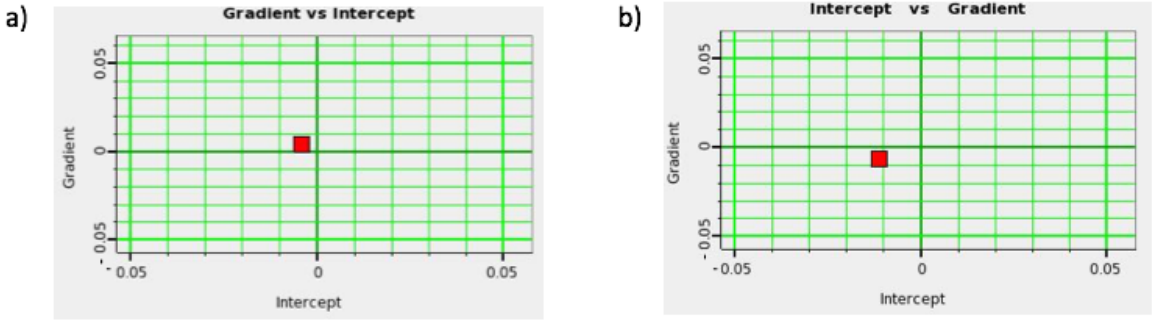


**Figure 6.8.** The figure shows the gradient and intercept for top reservoir in scenario 0 (20 Hz wavelet), a) initial rock, b) CO<sub>2</sub> saturated rock (S0.1) .

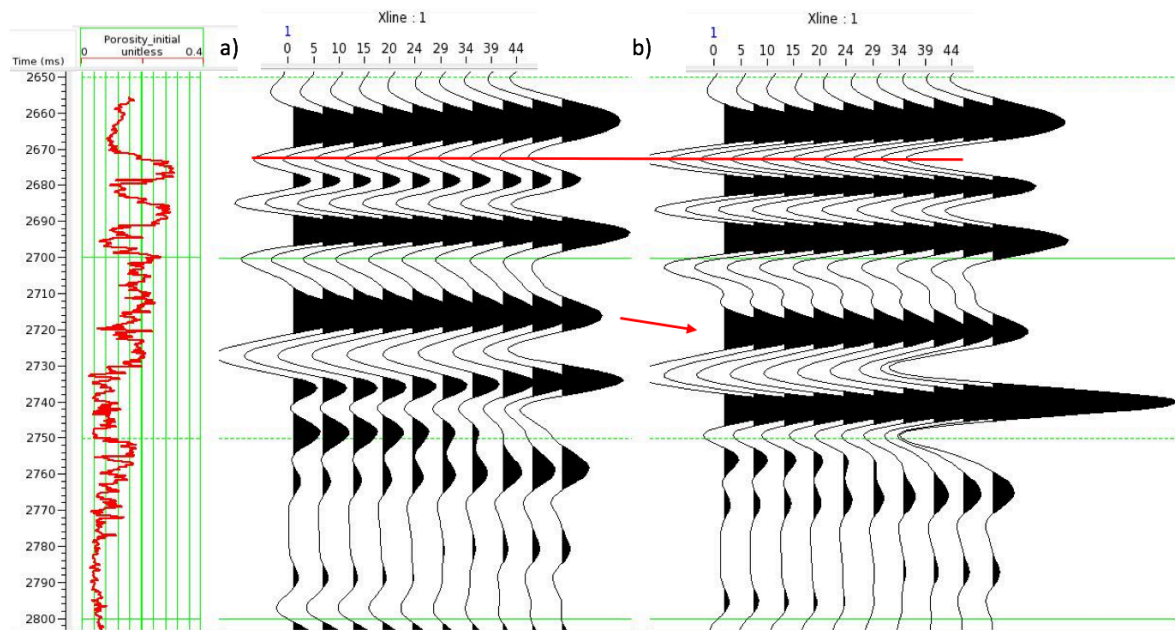


**Figure 6.9.** The figure shows the synthetic AVA gathers for scenario 0 (40 Hz wavelet), displaying the gather for a) brine saturated rock and b) CO<sub>2</sub> saturated rock. The red line represents the negative amplitude of which a more detailed analysis is performed. The red arrow outlines the increasing travel times occurring due to fluid substitution.

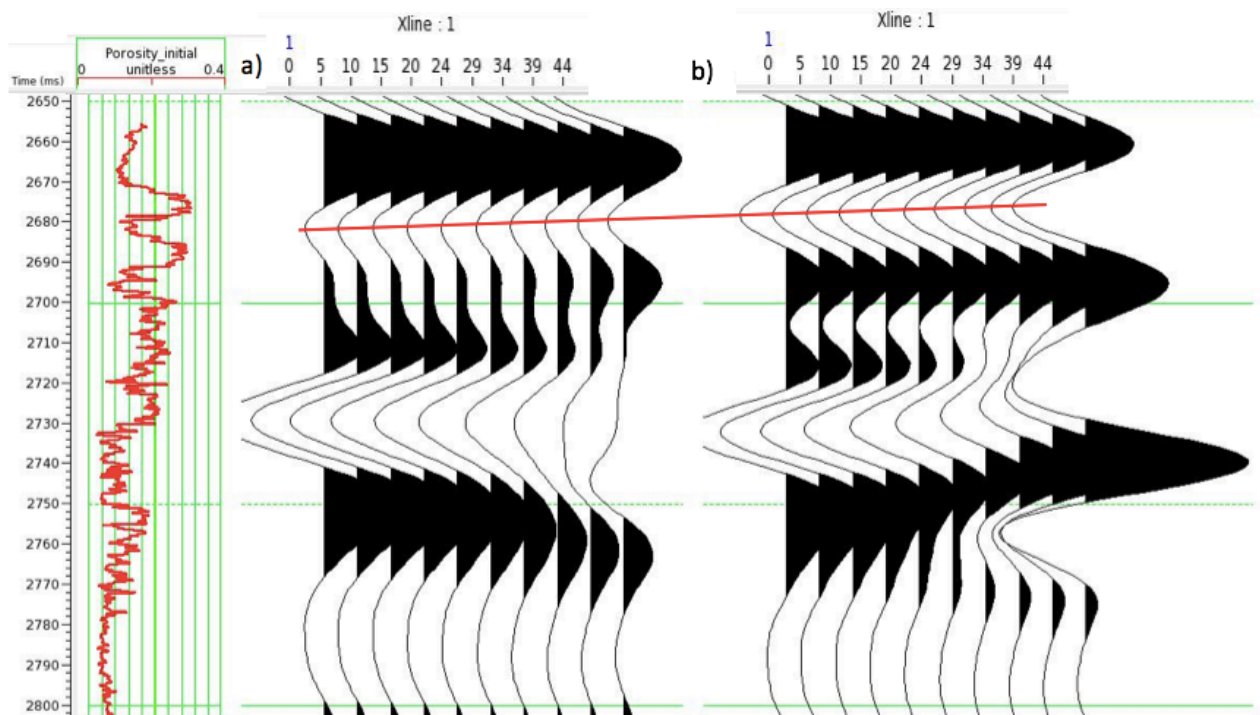


**Figure 6.10.** The figure shows the synthetic AVA gathers for scenario 0 (20 Hz wavelet), displaying the gather for a) brine saturated rock and, b) CO<sub>2</sub> saturated rock. The red line represents the negative amplitude of which the gradient analysis is performed.

### 6.3 Scenario One: The Effect of Altered Pore Geometries

Scenario 1 represents the effect of CO<sub>2</sub> injections in a tight carbonate rock. Rock-fluid interactions are expected to increase the concentration of low-aspect ratio pores on expense of spherical pores. Table 6.2 summarizes the expected variations in the rock fabric of the carbonate rock. Further information regarding scenario 1 is provided in section 5.2.1. The effect of fluid substitution is not evaluated in detail, but included in the figures.

	$\Delta\phi$	Cracks	Spherical pores	Intergranular pores	Dissolved carbonate minerals in pore fluid
<b>Initial P<sub>p</sub></b>	~0	+	-	+	+
<b>Increased P<sub>p</sub></b>	~0	+	~0	-	~0

**Table 6.2.** The table summarizes the effect of CO<sub>2</sub> injections in scenario 1. +/- represent increasing or decreasing concentration, ~0 means no variation is assumed

#### 6.3.1 Elastic Properties

Figures 6.11, 6.12 and 6.13 demonstrate the variations in elastic properties and density at the different stages of scenario 1. Dissolution effects (S1.2) and compaction (S1.3) is believed to be a source of the discussed variations in elastic properties observed in carbonate rocks after CO<sub>2</sub> injections. The blue line represents the moduli of the initial reservoir saturated with brine. The red line is the moduli of the CO<sub>2</sub> saturated reservoir at the different stages of scenario 1.

To evaluate the effect of dissolution targeting the pore geometry, the aspect concentration of the initial rock is changed according to the values in S1 in Table 5.2. The porosity remains unaltered. By increasing the concentration of cracks and intergranular pores on expense of spherical pores, both the bulk and shear modulus is reduced compared to the initial CO<sub>2</sub> saturated rock. This effect is illustrated in Figures 6.11b and 6.12b. Figure 6.13b shows that the density is unaffected by the pore geometry of the rock.

To investigate the effect of compaction, the concentration of cracks is increased on the expense of intergranular pores. Also, the pore-pressure is increased to 44 MPa. This will induce an overpressure of 11 MPa. As spherical pores are stiff, they are left unaltered. Figures 6.11c and 6.12c show that both the bulk and shear modulus is reduced as a response to the continued alterations in pore geometries and increased pore-pressure. A small increase in the CO<sub>2</sub> saturated density from Figure 6.13b to 6.13c follows the increasing pore-pressure and compaction.

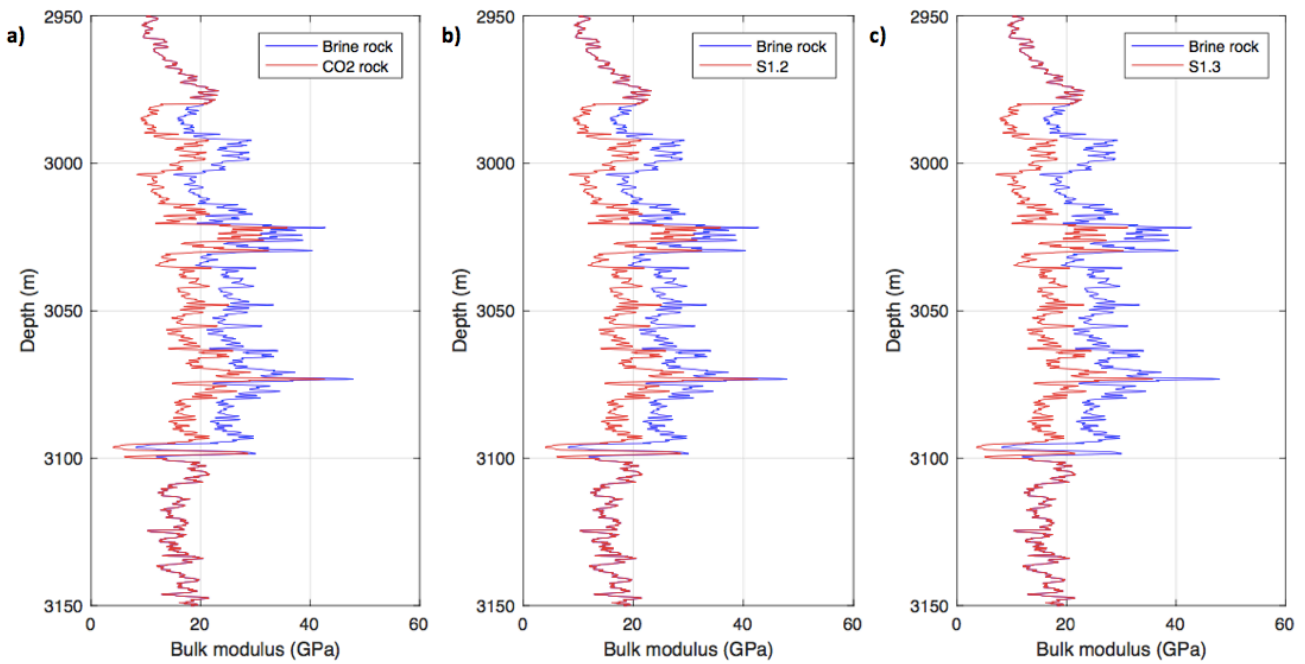


**Figure 6.11.** The figure shows the variation in brine saturated (blue) reservoir bulk modulus and a) CO<sub>2</sub> saturated reservoir (S1.1), b) dissolved reservoir (S1.2) and c) compacted reservoir (S1.3).

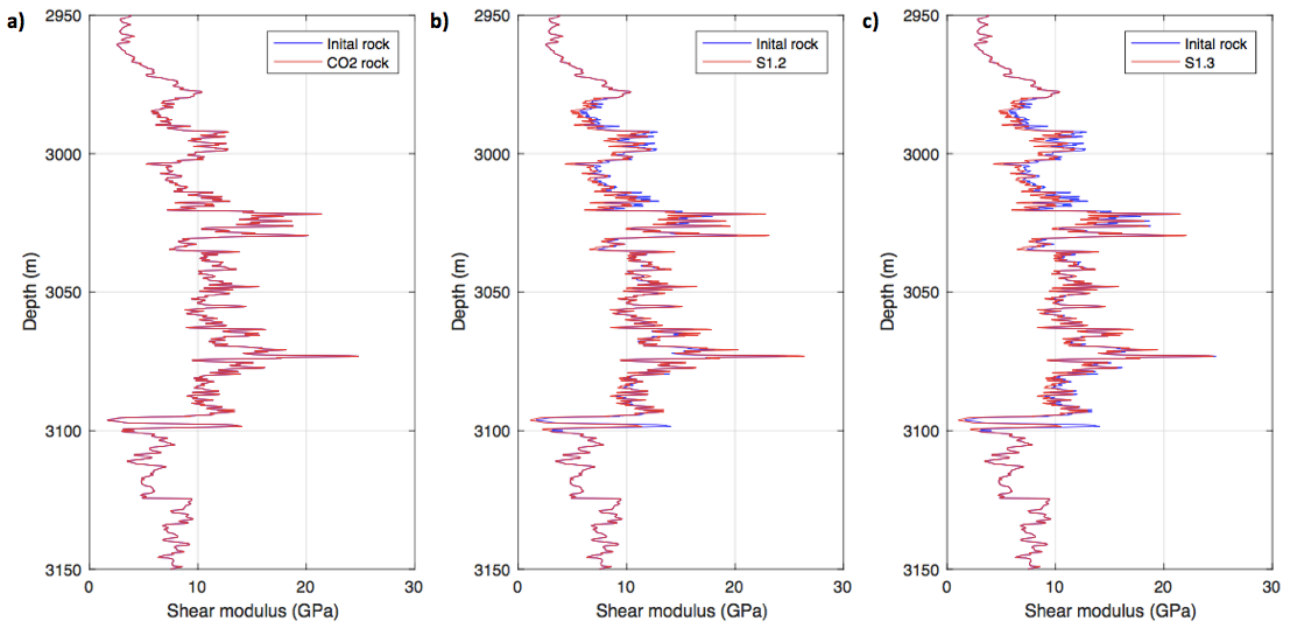


**Figure 6.12.** The figure shows the variation in brine saturated (blue) reservoir shear modulus and a) CO<sub>2</sub> saturated reservoir (S1.1), b) S Dissolved reservoir (S1.2) and c) compacted reservoir (S1.3).

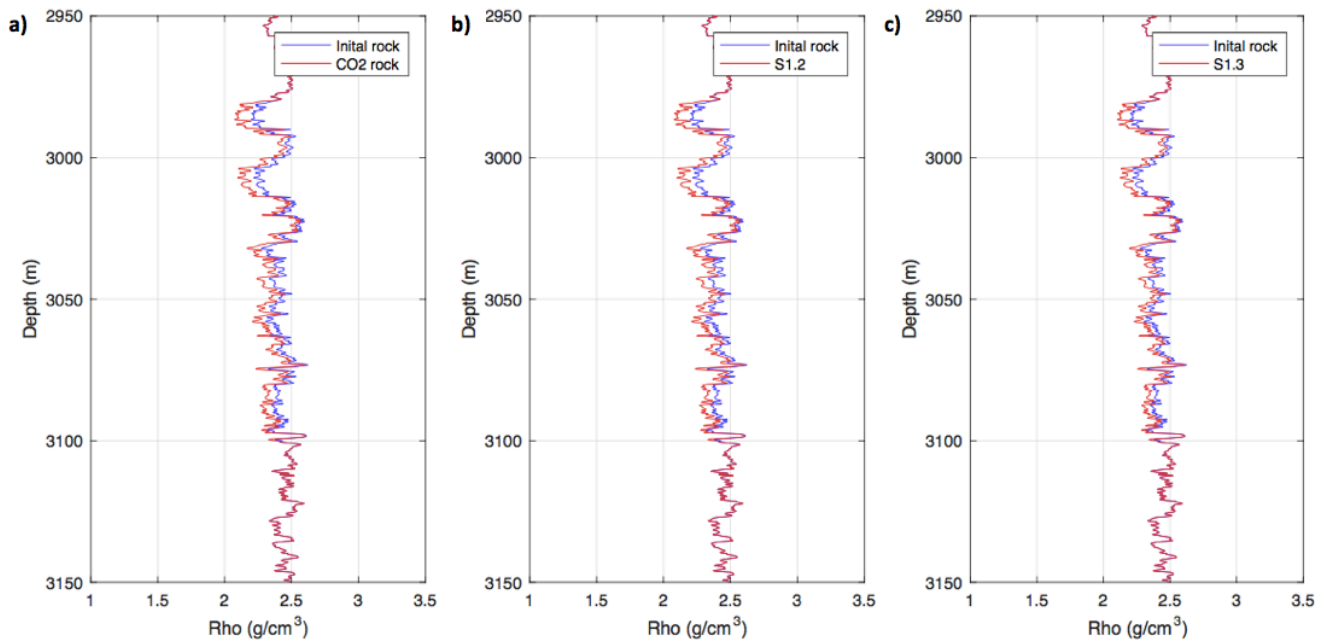


**Figure 6.13.** The figure shows the variation between brine saturated (blue) reservoir density and a) CO<sub>2</sub> saturated reservoir (S1.1), b) dissolved reservoir (S1.2) and c) compacted reservoir (S1.3).

### 6.3.2 Seismic Velocity and Acoustic Impedance

Dissolution increases the concentration of low aspect ratio pores on expense of spherical pores. A moderate reduction in both P- and S-wave velocities is observed following the dissolution effects (Figures 6.14b and 6.15b). The effect of compaction and increased pore-pressure of the CO<sub>2</sub> bearing rock induces small reductions in both P- and S-wave velocity, demonstrated in Figures 6.14c and 6.15c. Evaluating the velocity trend at the different stages of scenario 1, the effect of altering the pore geometry on the velocity is revealed. Increasing the concentration of low-aspect ratio pores will induce reductions in the seismic velocities of the rock frame.

Figure 6.16 displays the rock physics template for Scenario 1. The reservoir data is plotted as a function of calcite content. The rest of the data set is plotted in gray. Figure 6.16c displays the effect of dissolution on the CO<sub>2</sub> saturated reservoir zone. Compared to the plot in 6.16b, the acoustic impedance is now slightly reduced while the velocity ratio shows a small increase. Knowing that the density is unaffected by alterations in pore geometry, the reduction in acoustic impedance is an effect of the reduced P-wave velocity alone. As the rock is compacted, the acoustic impedance is reduced somewhat more, as displayed in Figure 6.16d. The velocity ratio exhibits little variations due to this effect.

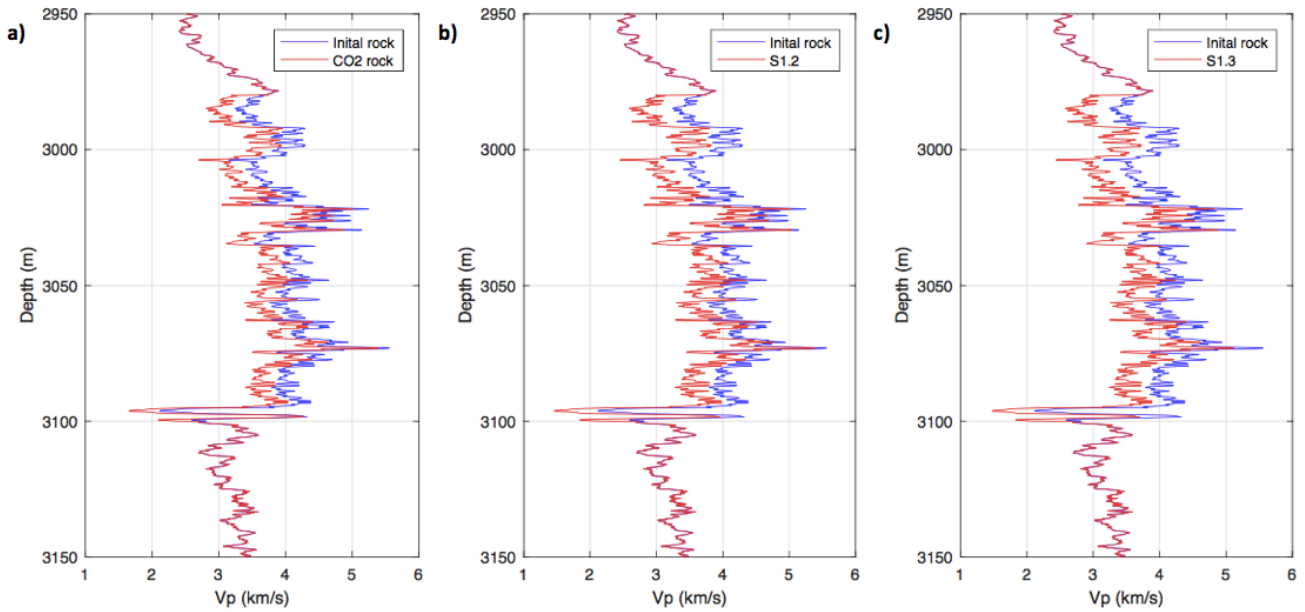


**Figure 6.14.** The figure displays the contrast in P-wave velocity of brine saturated rock (blue) and a) CO<sub>2</sub> saturated reservoir (S1.1), b) dissolved reservoir (S1.2) and c) compacted reservoir (S1.3).

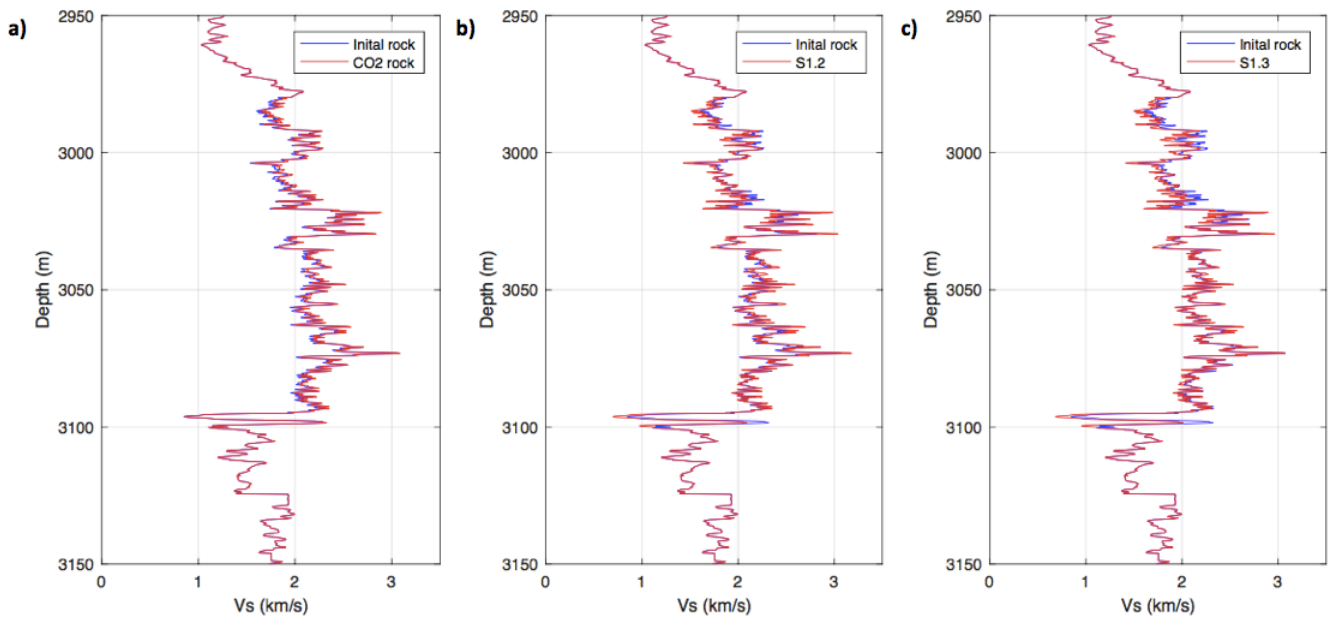


**Figure 6.15.** The figure displays the contrast in S-wave velocity of brine saturated rock (blue) and a) CO<sub>2</sub> saturated reservoir (S1.1), b) dissolved reservoir (S1.2) and c) compacted reservoir (S1.3).

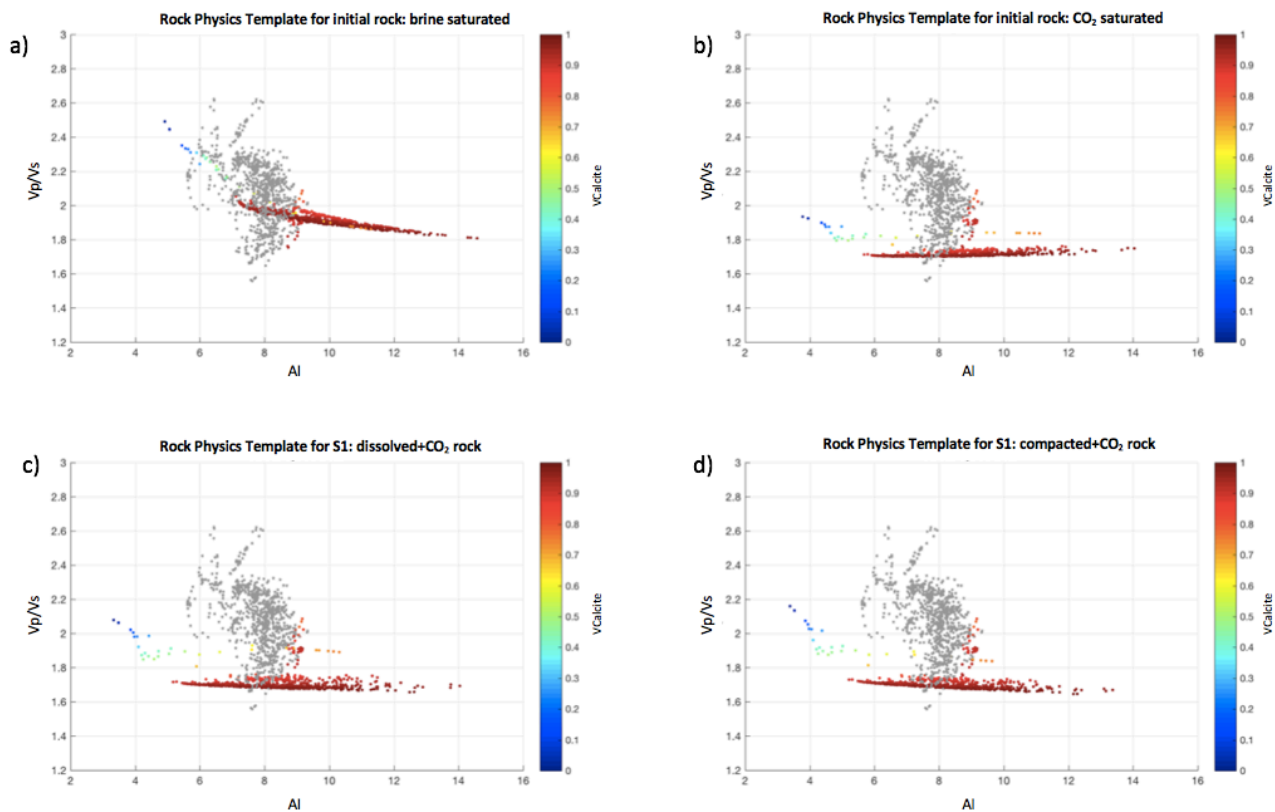


**Figure 6.16.** The figure shows the rock physics template of scenario 1 for a) the initial rock (S1.0), b) CO<sub>2</sub> saturated rock (S1.1), c) dissolved rock (S1.2) and d) compacted rock (S1.3). The reservoir data is plotted as a function of calcite content; the remaining data is plotted in gray.

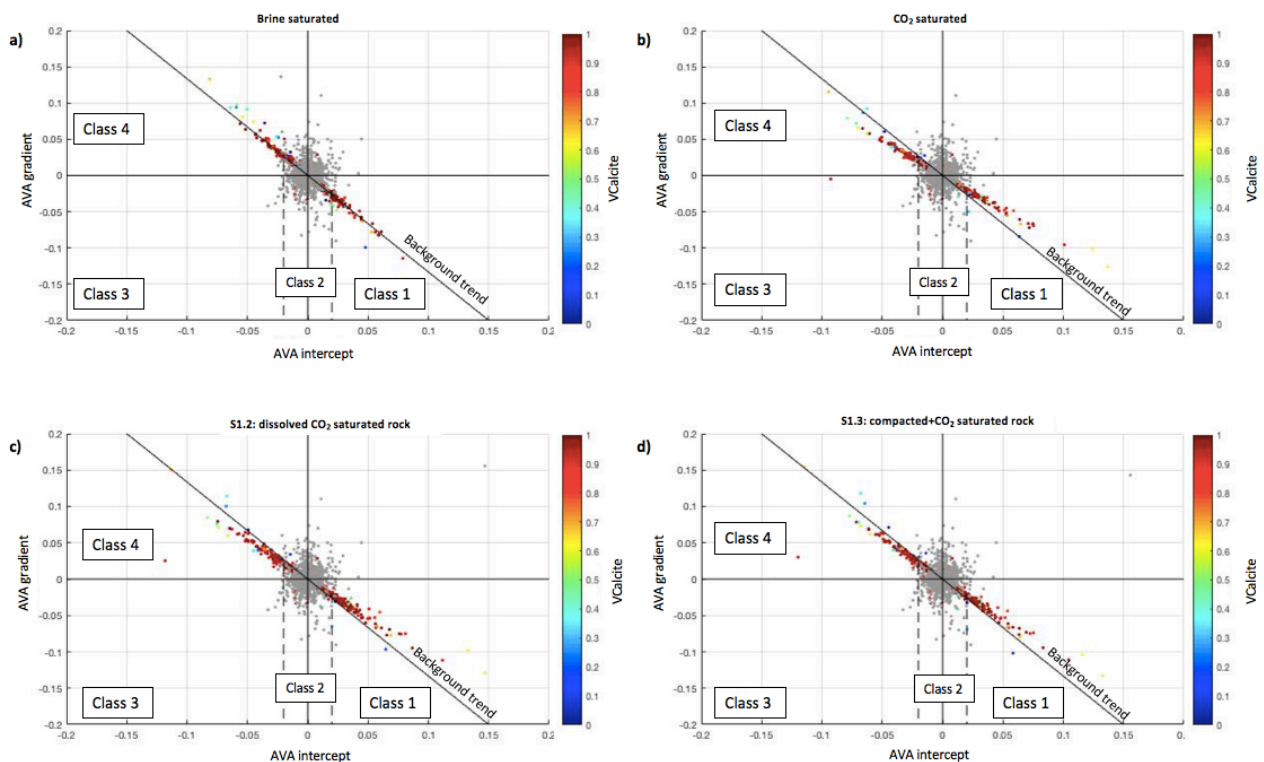
### 6.3.3 Amplitude Versus Angle Response

Figure 6.17 displays the intercept-gradient cross plot for scenario 1. The increased concentration of cracks and compaction will induce a slight reduction in the deviation from the background trend. The data now plots closer to the background trend compared to the initial CO<sub>2</sub> saturated reservoir data.

The calculated P-wave reflectivity using the modelled well data describing scenario 1 is displayed in Figure 6.18. The increased concentration of cracks and intergranular pores will enhance the reflectivity contrast between the brine saturated rock, and the dissolved CO<sub>2</sub> saturated rock (termed S1.2). This effect is illustrated in Figure 6.18b. The reflectivity log of the compacted reservoir follows in Figure 6.18c, where the reflectivity contrast is slightly increased. The calculated AVA gradient of the dissolved and compacted reservoir is plotted in Figure 6.19b and 6.19c. The gradient displays a slightly stronger value following both dissolution and compaction compared to the initial CO<sub>2</sub> saturated rock in Figure 6.19b.



A synthetic AVA gather for scenario 1, modelled using a Ricker wavelet with a peak frequency of 40 Hz, is presented in Figure 6.20. Gathers c) and d) show stronger amplitudes as a result of dissolution and compaction. The effect of an increasing amplitude is clearly demonstrated in the zone marked by the red circle. Here, a new positive amplitude appears, that was not visible in gathers a) and b). In addition to affecting the strength of the amplitude and the AVA gradient, dissolution induce a time shift in the synthetic gathers. This time shift is more prominent in the gather where dissolution effects are included, compared to the gather only including fluid effects. The red arrow marks the time shift in one of the reflectors.



**Figure 6.17.** The figure shows the intercept-gradient cross plot for a) brine saturated rock (S1.0) b) CO<sub>2</sub> saturated rock (S1.1) c) dissolved and CO<sub>2</sub> saturated rock (S1.2) and d) compacted and CO<sub>2</sub> saturated rock (S1.3). The reservoir data is plotted as a function of calcite content; the remaining data is plotted in gray.



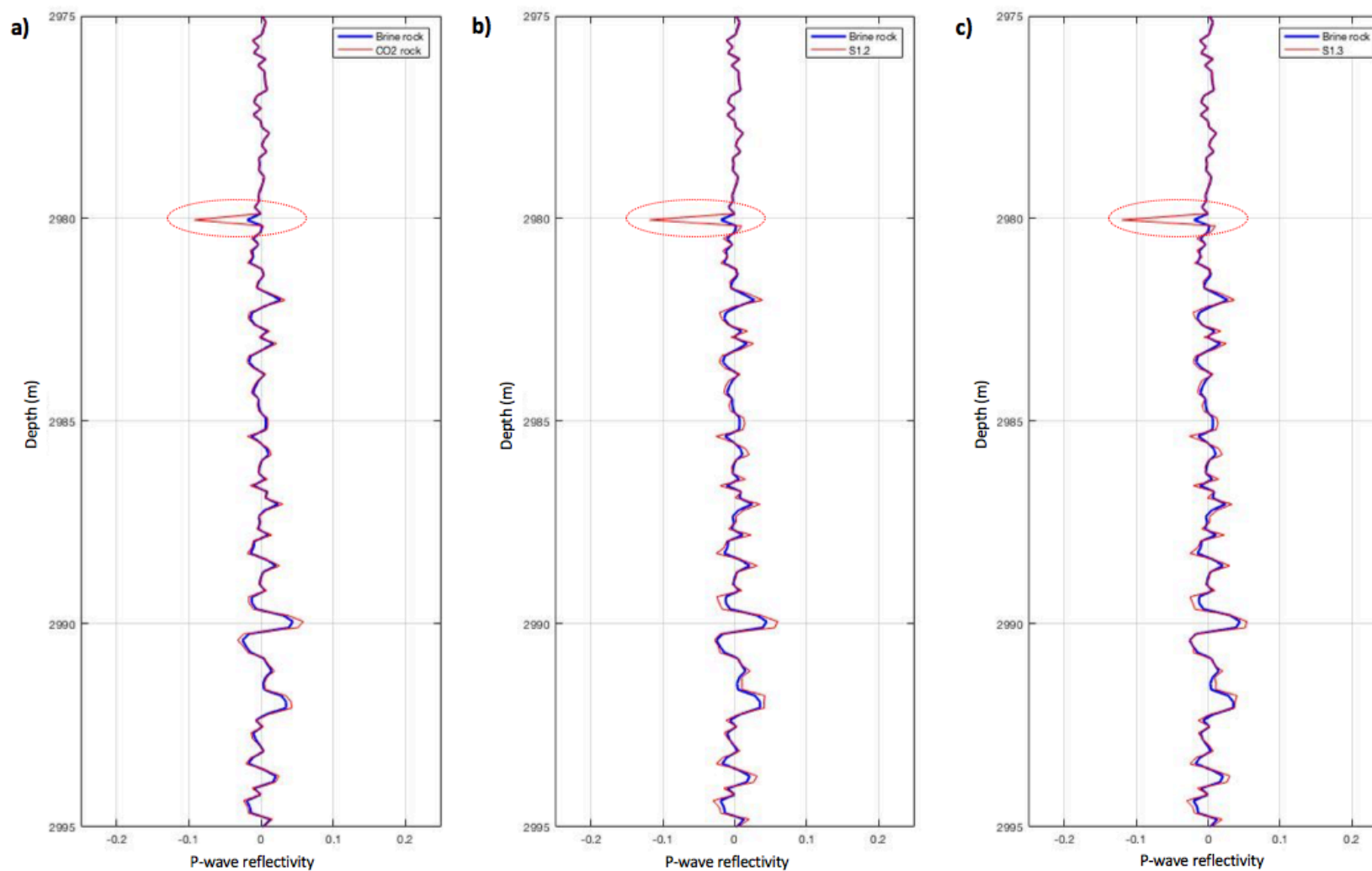


**Figure 6.18.** The figure compares the P-reflectivity for scenario 1. The blue line represent the brine saturated rock and the red lines in a) the CO<sub>2</sub> saturated rock (S1.1), b) CO<sub>2</sub> saturated and dissolved rock (S1.2) and c) compacted CO<sub>2</sub> rock (S1.3). The red circle marks an anomaly from the brine saturated reflectivity.

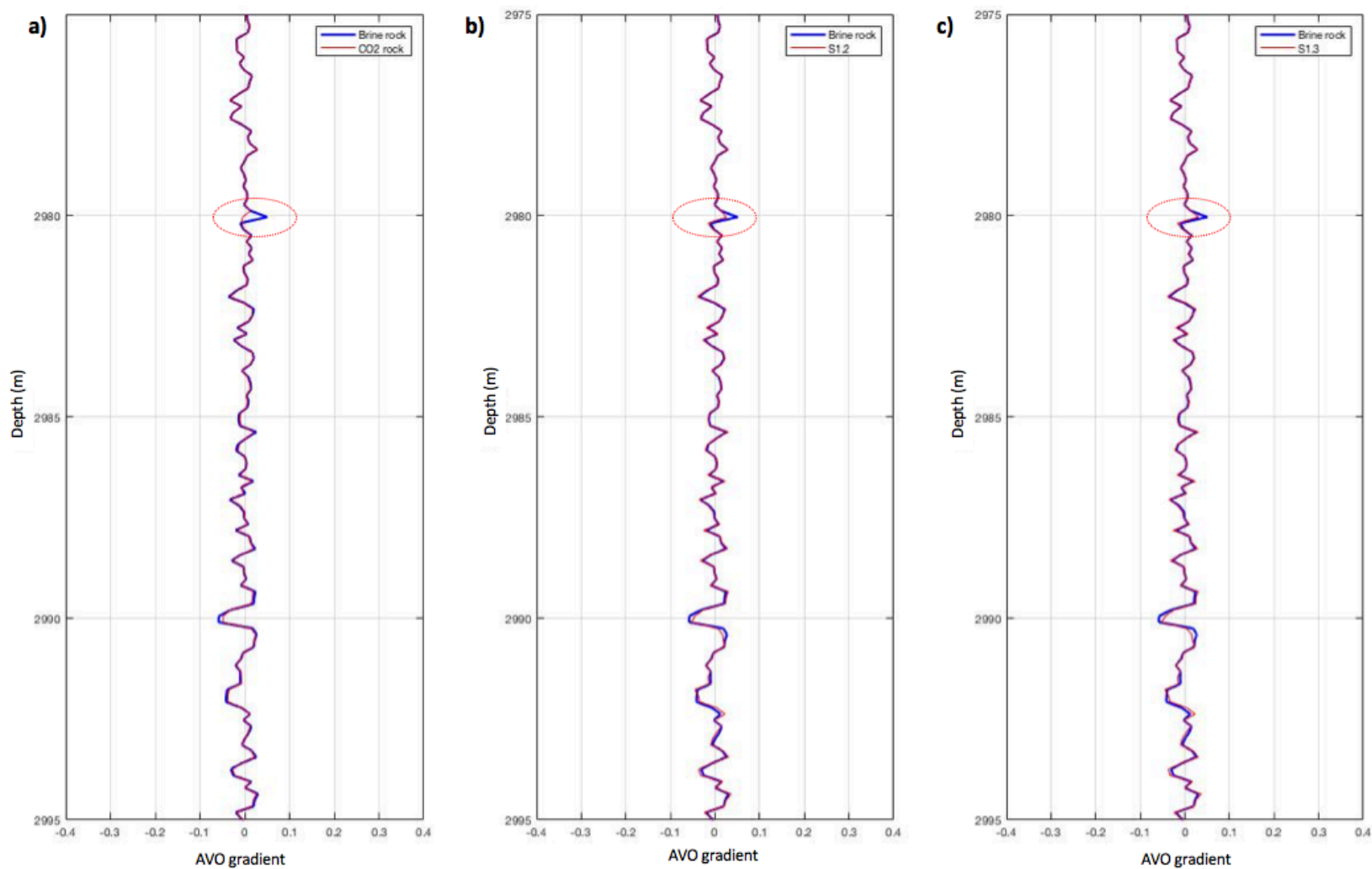


**Figure 6.19.** The figure compares the AVO gradient for scenario 1. The blue line represent the brine saturated rock and the red lines in a) the CO<sub>2</sub> saturated rock (S1.1), b) CO<sub>2</sub> saturated and dissolved rock (S1.2) and c) compacted CO<sub>2</sub> rock (S1.3). The red circle marks an anomaly from the brine saturated reflectivity.

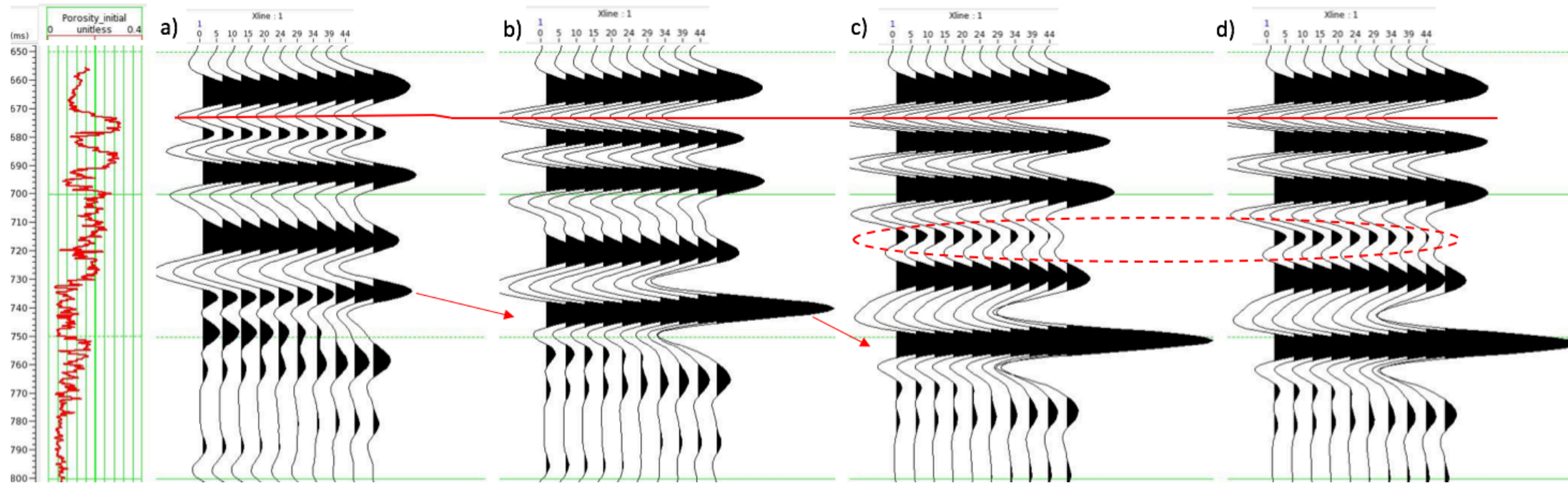


**Figure 6.20.** The figure shows the synthetic AVA gathers for scenario 1 (40 Hz wavelet), displaying the gather for a) brine saturated rock (S1.0), b) CO<sub>2</sub> saturated rock (S1.1), c) CO<sub>2</sub> saturated and dissolved rock (S1.2) and d) CO<sub>2</sub> saturated and compacted rock (S1.3). The red line represents the negative amplitude of which the gradient analysis is performed. The red arrows outline the increasing travel times occurring due to fluid substitution and altered rock fabric. The red circle highlights the new amplitudes occurring due to dissolution and compaction.

A more detailed AVA modelling was performed in the top of the reservoir. The target reflector is marked by a red line in Figure 6.20. This zone also represents an anomaly in Figure 6.18, where it is marked by a red circle. Figure 6.21 displays the gradient versus intercept plot for the top reservoir. The effect of dissolution and compaction is plotted in Figures 6.21c and 6.21d, where the intercept is reduced compared to the value of the brine and CO<sub>2</sub> saturated reservoir. In relation to the brine saturated gradient, the fluid substitution effect displays a gradient reduction whereas the fluid substituted *and* dissolved reservoir display a relative gradient increase. As this result is opposite of what predicted only evaluating the fluid effect, it is a possible source for misinterpreting the dataset.

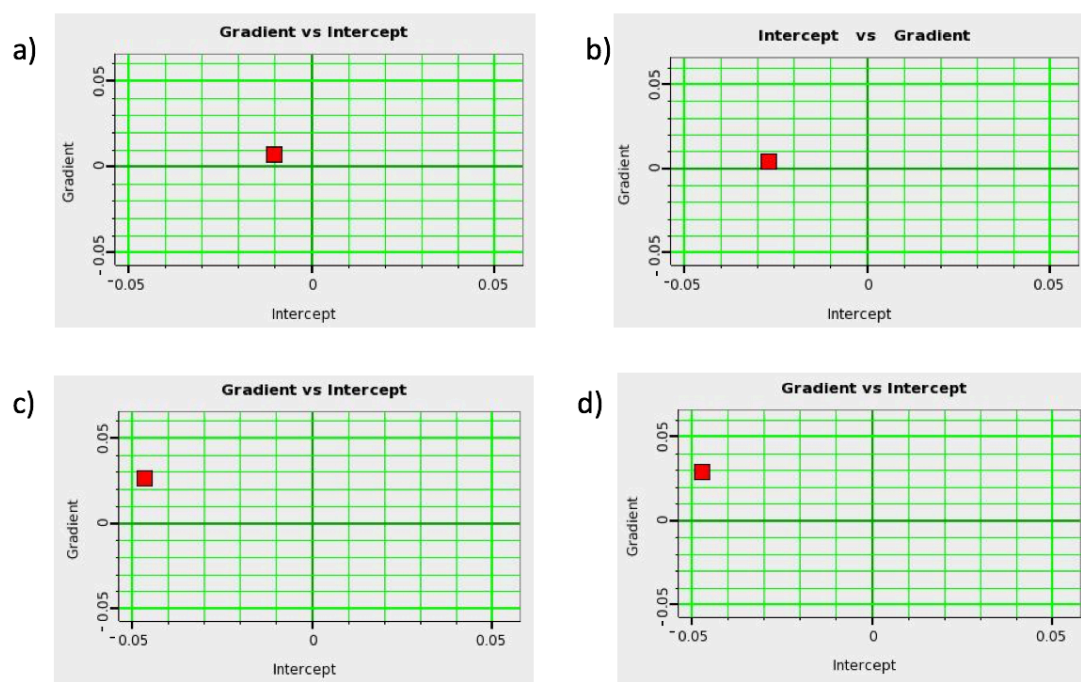


**Figure 6.21.** The figure shows the gradient and intercept for scenario 1 (40 Hz wavelet) for a) initial rock (S1.0), b) CO<sub>2</sub> saturated rock (S1.1), c) CO<sub>2</sub> saturated and dissolved rock (S1.2) and d) CO<sub>2</sub> saturated and compacted rock (S1.3).

An additional synthetic gather is created, using a Ricker wavelet with peak frequency of 20 Hz. The synthetic gather is displayed in Figure 6.23. The intercept versus gradient plots in Figure 6.22 represents the high porosity zone in the top reservoir, marked by the red line in the synthetic gather in Figure 6.23. The intercept values for Figures 6.22c and 6.22d are approximately the same, indicating little reflectivity effect of the compaction. The gradient of the dissolved rock plots at 0, suggesting that there is very little amplitude sensitivity to angle. Only small effects can be observed due to increased pore-pressure on both gradient or intercept, compared to the normal pressured reservoir (Figure 6.22d).

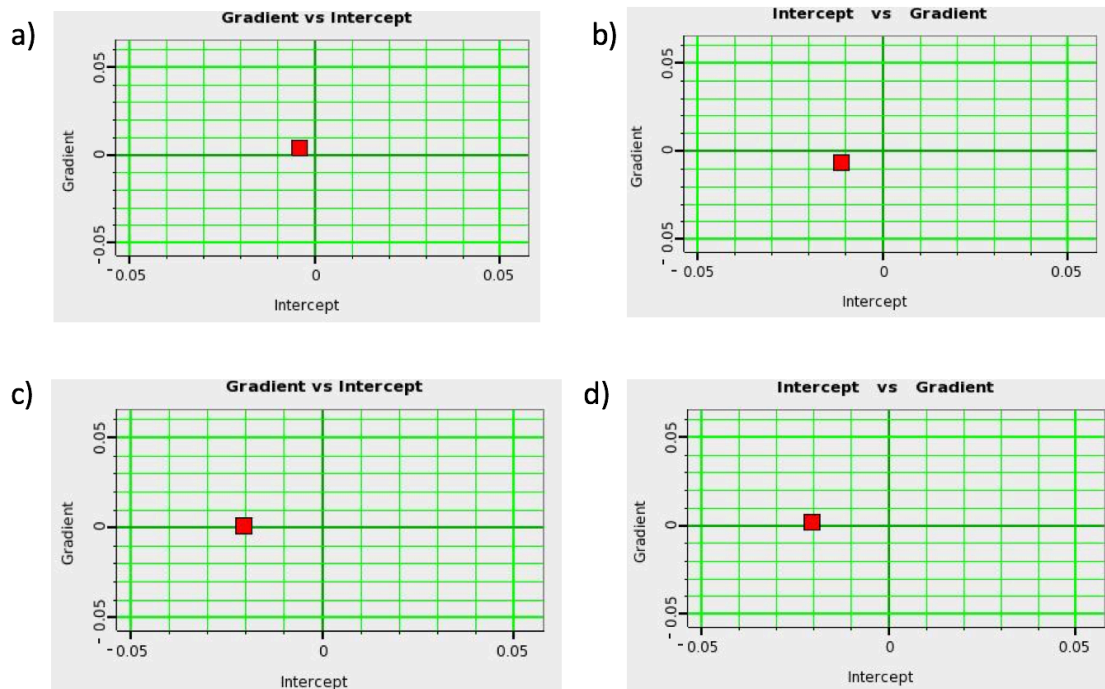


**Figure 6.22.** The figure shows the gradient and intercept for scenario 1 (20 Hz wavelet) for a) initial rock (S1.0), b) CO<sub>2</sub> saturated rock (S1.1), c) CO<sub>2</sub> saturated and dissolved rock (S1.2) and d) CO<sub>2</sub> saturated and compacted rock (S1.3).



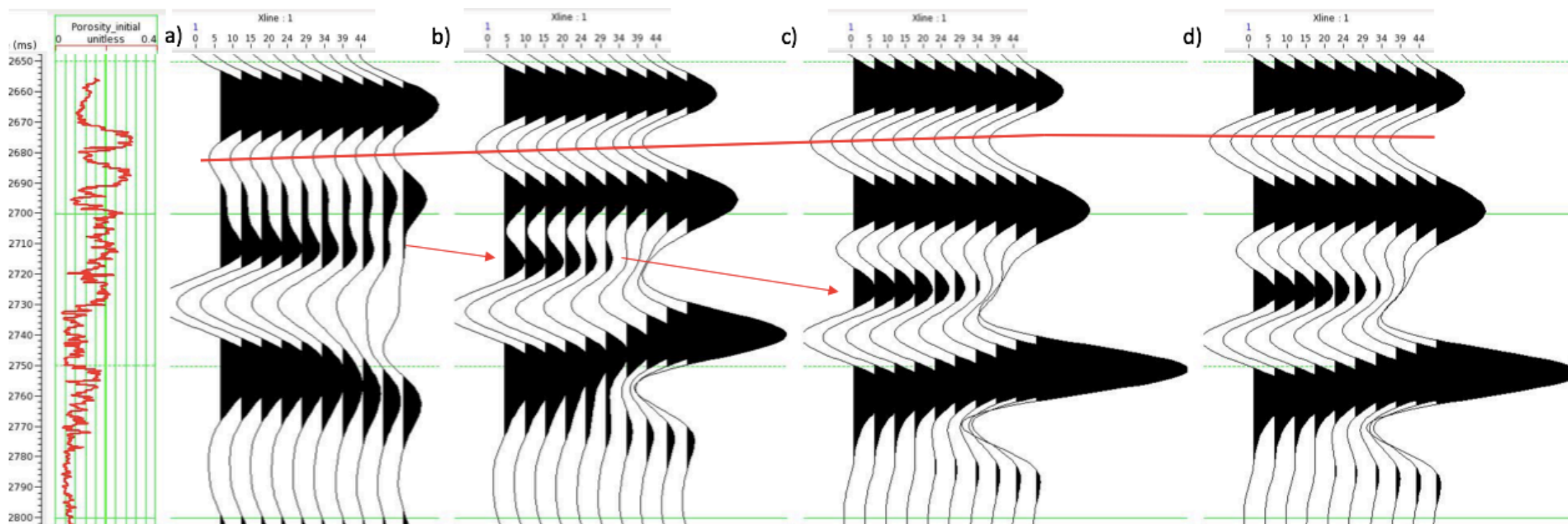


**Figure 6.23.** The figure shows the synthetic AVA gathers for scenario 1 (20 Hz wavelet), displaying the gather for a) brine saturated rock (S1.0), b) CO<sub>2</sub> saturated rock (S1.1), c) CO<sub>2</sub> saturated and dissolved rock (S1.2) and d) CO<sub>2</sub> saturated and compacted rock (S1.3). The red line represents the negative amplitude of which the gradient analysis is performed. The red arrows outline the increasing travel times occurring due to fluid substitution and altered rock fabric.

## 6.4 Scenario Two: The Effect of Increased Porosity

Scenario 2 represents the effect of CO<sub>2</sub> injections in a granular carbonate rock. Rock-fluid interactions are expected to increase the porosity, leaving the pore geometry unaltered. Table 6.3 summarizes the expected variations in the rock fabric of the carbonate rock. Information regarding scenario 2 is provided in section 5.2.1. The effect of fluid substitution is not evaluated in detail, but included in the figures.

	$\Delta\phi$	Cracks	Spherical pores	Intergranular pores	Dissolved carbonate minerals in pore fluid
Initial P <sub>P</sub>	+	0	0	0	+
Increased P <sub>P</sub>	~0	+	~0	-	~0

**Table 6.3.** The table summarizes the effect of CO<sub>2</sub> injections in scenario 2. +/- represent increasing or decreasing concentration, ~0 means no variation is assumed.

### 6.4.1 Elastic Properties and Density

Figures 6.24, 6.25 and 6.26 demonstrate the variations in elastic properties and density at the different stages of scenario 2. The blue line represents the moduli and density of the initial reservoir saturated with brine. The red line is the moduli and density of the CO<sub>2</sub> saturated reservoir at the different stages of scenario 2. Dissolution effects (S2.2) and compaction (S2.3) is believed to be a source of the discussed variations in elastic properties of a carbonate rock after CO<sub>2</sub> injections (Chapter 4). To study the effect of dissolution targeting the pore volume, the porosity of the CO<sub>2</sub> saturated rock is increased by 5%. The pore geometry of the rock remains unaltered and is defined in S2 in Table 5.2.

By increasing the porosity, the bulk and shear modulus is reduced. This effect is illustrated in Figures 6.24b and 6.25b. Increasing the porosity will result in density reductions, as illustrated in Figure 6.26b. The effect of compaction is modelled by increasing the concentration of cracks on the expense of intergranular pores. The pore-pressure is increased to 44 MPa. This induce an overpressure of 11 MPa. As spherical pores are stiff, they are left unaltered. Figures 6.24c and 6.25c reveals that the bulk and shear modulus are not affected noticeably by the compacted rock. The effect of compaction and altered pore-pressure increase the density somewhat from 2.26b to 2.26c.

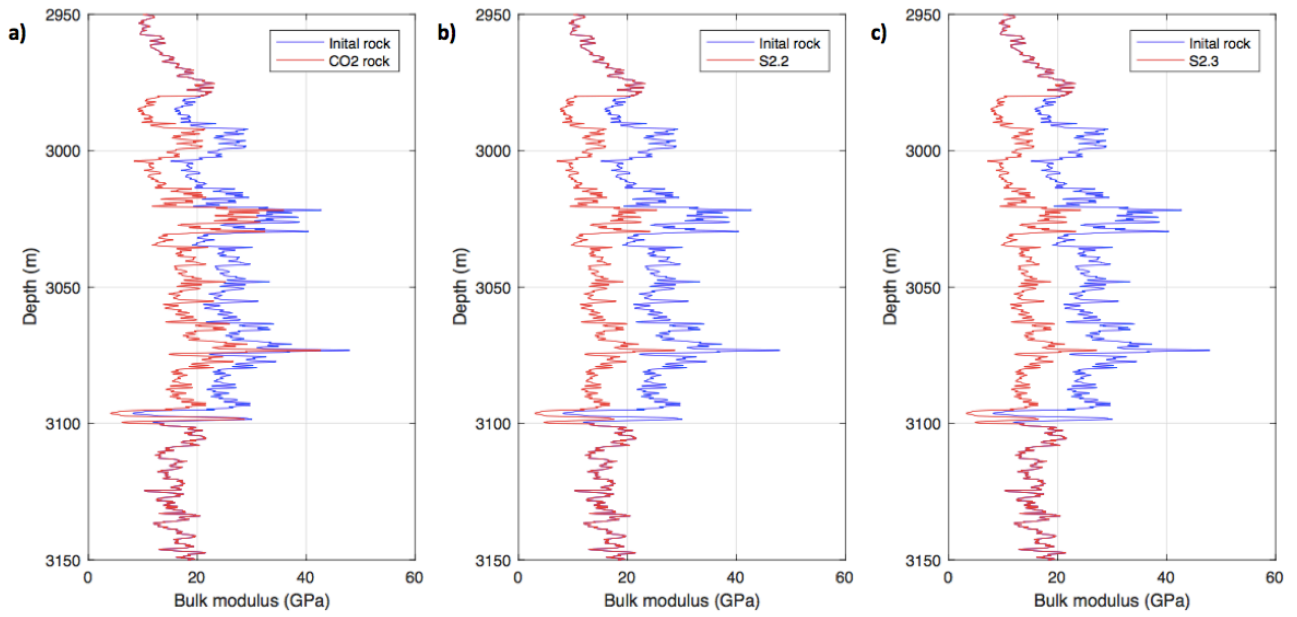


**Figure 6.24.** The figure shows the variation in brine saturated (blue) reservoir bulk modulus and a) CO<sub>2</sub> saturated reservoir (S2.1), b) dissolved reservoir (S2.2) and c) compacted reservoir (S2.3).

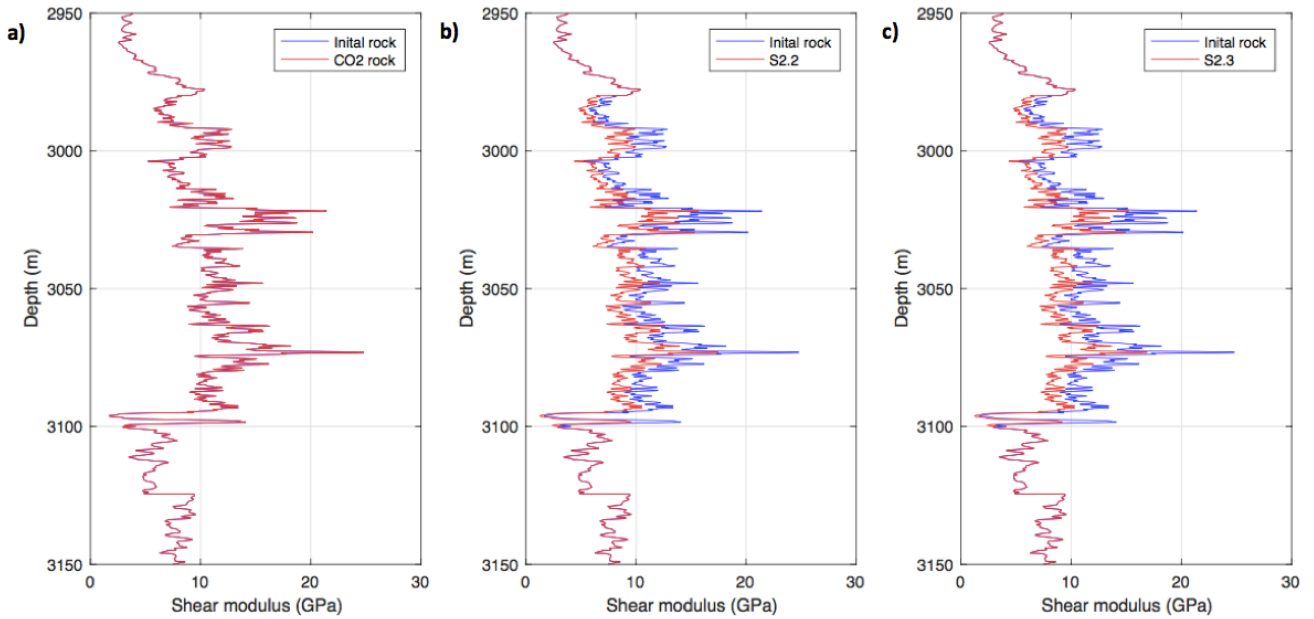


**Figure 6.25.** The figure shows the variation in brine saturated (blue) reservoir shear modulus and a) CO<sub>2</sub> saturated reservoir (S2.1), b) dissolved reservoir (S2.2) and c) compacted reservoir (S2.3).



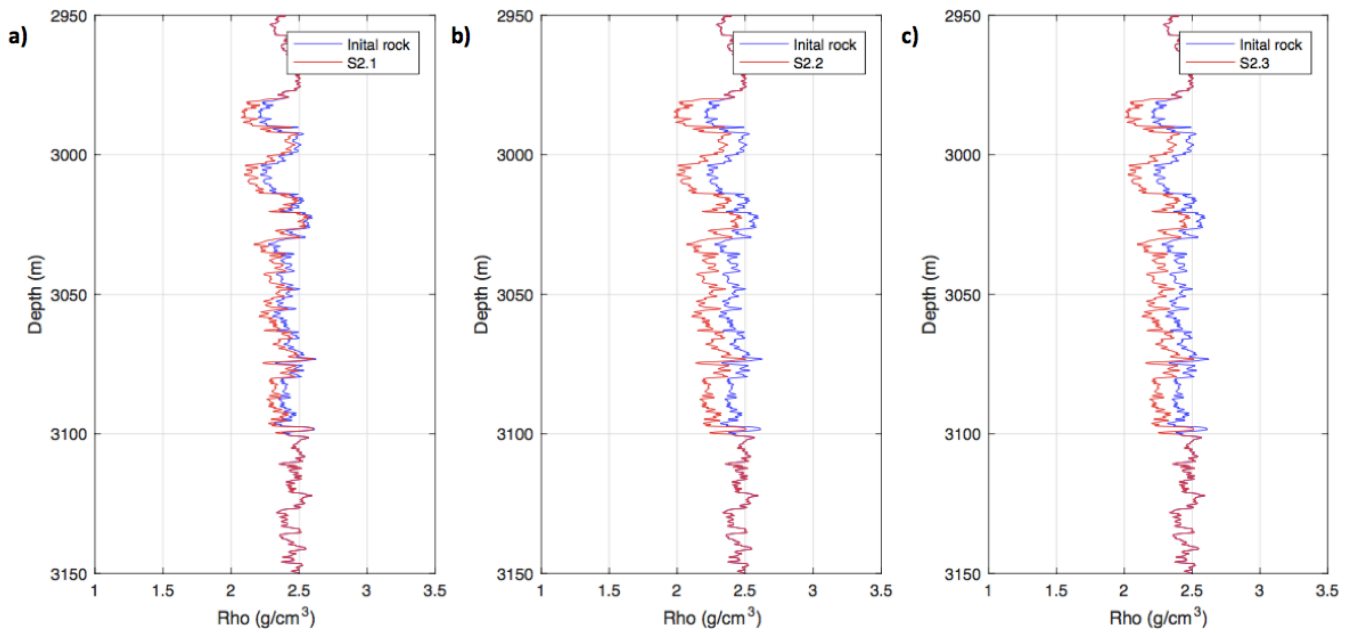


**Figure 6.26.** The figure shows the variation in brine saturated (blue) reservoir density and a)  $\text{CO}_2$  saturated reservoir (S2.1), b) dissolved reservoir (S2.2) and c) compacted reservoir (S2.3).

#### 6.4.2 Seismic Velocity and Acoustic Impedance

The 5% increase in porosity following dissolution induce reductions in both P- and S-wave velocities (Figures 6.27b and 6.28b). Compacting the  $\text{CO}_2$  bearing rock demonstrates little effect on either of the seismic velocities compared to the dissolved  $\text{CO}_2$  saturated reservoir (Figures 2.27c and 6.28c). Evaluating the velocity trend at the different stages of scenario 2, the effect of altering the pore volume is revealed. By increasing the porosity, the velocity of the rock frame itself is reduced.

Figure 6.29 displays the rock physics template for Scenario 2. The reservoir data is plotted as a function of calcite content, whilst the remaining data is plotted in gray. Figure 6.29c displays the effect of increased porosity on the  $\text{CO}_2$  saturated reservoir zone. Compared to the  $\text{CO}_2$  saturated plot in Figure 6.29b, the acoustic impedance is now slightly reduced while the velocity ratio displays very little effect to the increased porosity. The modelled compaction reduce the acoustic impedance somewhat more, as displayed in Figure 6.29d.

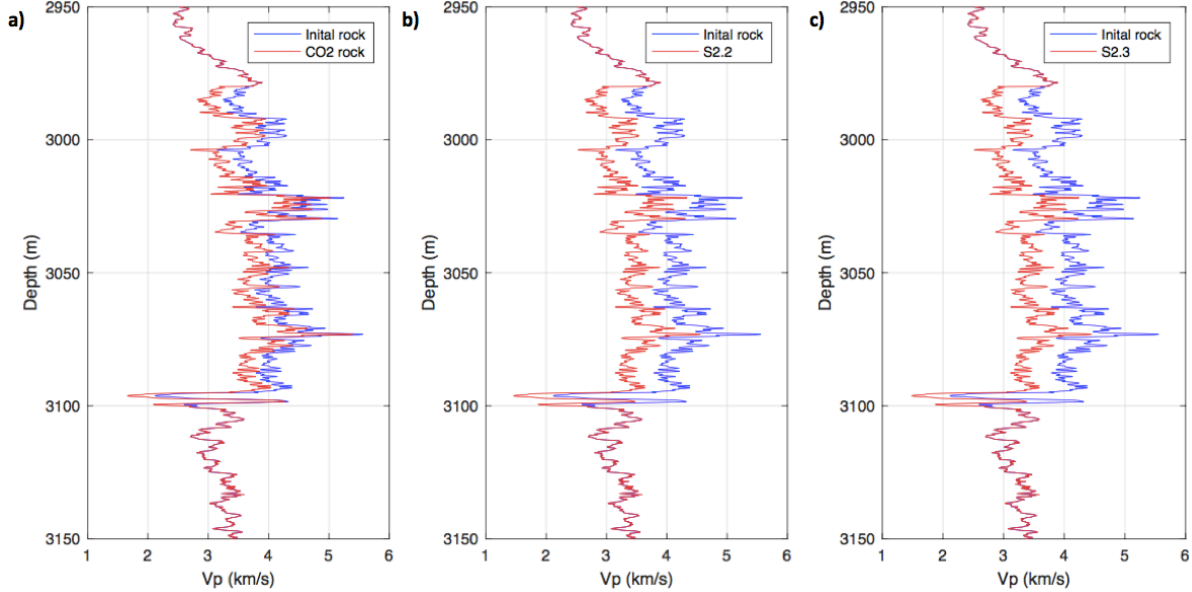


**Figure 6.27.** The figure displays the contrast in P-wave velocity of brine saturated rock (blue) and a) CO<sub>2</sub> saturated reservoir (S2.1), b) dissolved reservoir (S2.2) and c) compacted reservoir (S2.3).

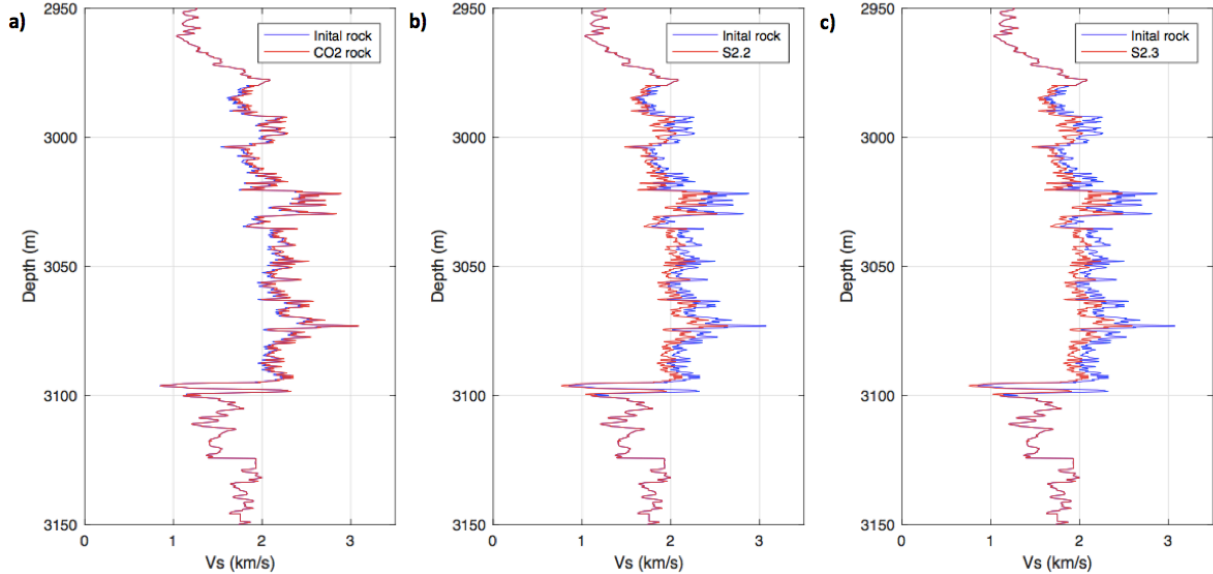


**Figure 6.28.** The figure displays the contrast in S-wave velocity of brine saturated rock (blue) and a) CO<sub>2</sub> saturated reservoir (S2.1), b) dissolved reservoir (S2.2) and c) compacted reservoir (S2.3).

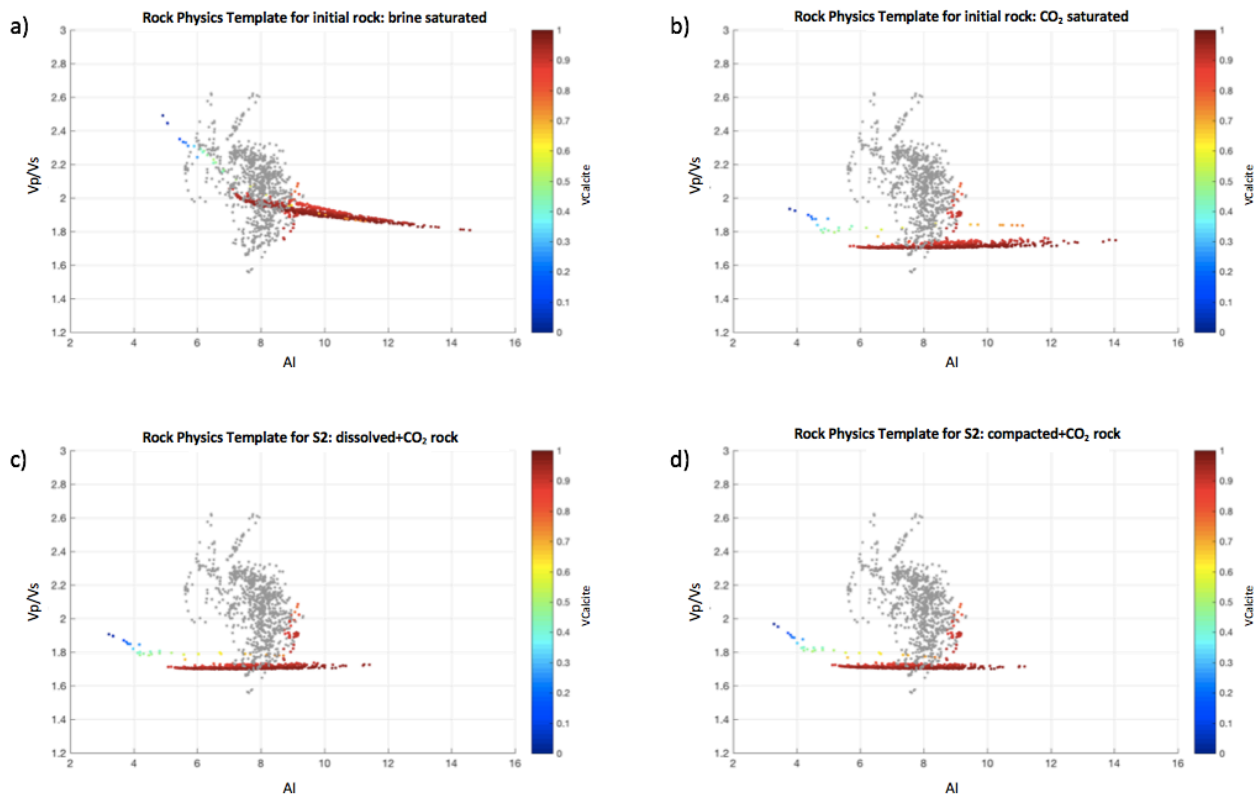


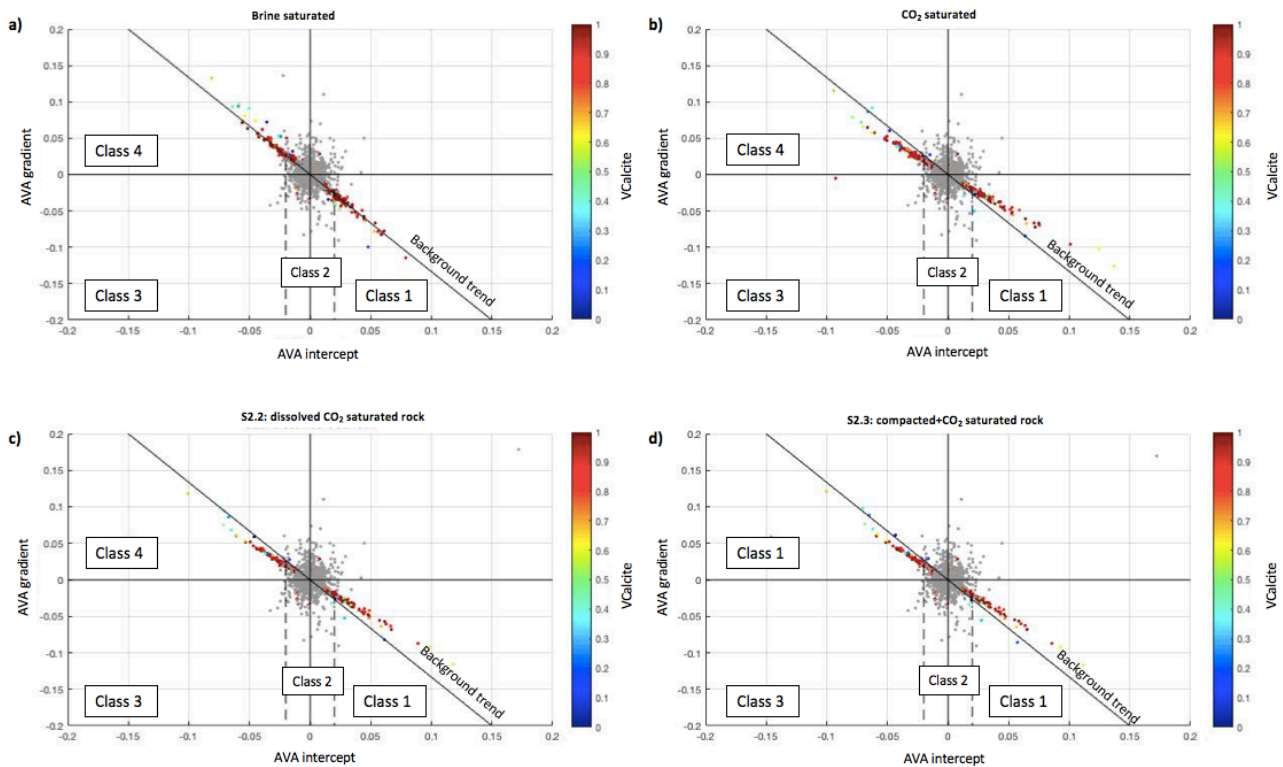
**Figure 6.29.** The figure shows the rock physics template of scenario 2 for a) the initial rock (S1.0), b) CO<sub>2</sub> saturated rock (S2.1), c) dissolved rock (S2.2) and d) compacted rock (S2.3). The reservoir data is plotted as a function of calcite content; the remaining data is plotted in gray.

### 6.4.3 AVA Analysis

Figure 6.30 displays an intercept-gradient cross plot for scenario 2. The data of the dissolved reservoir illustrate a deviation from the background trend. However, the contrast between the dissolved and the un-dissolved CO<sub>2</sub> saturated reservoir is not significant.

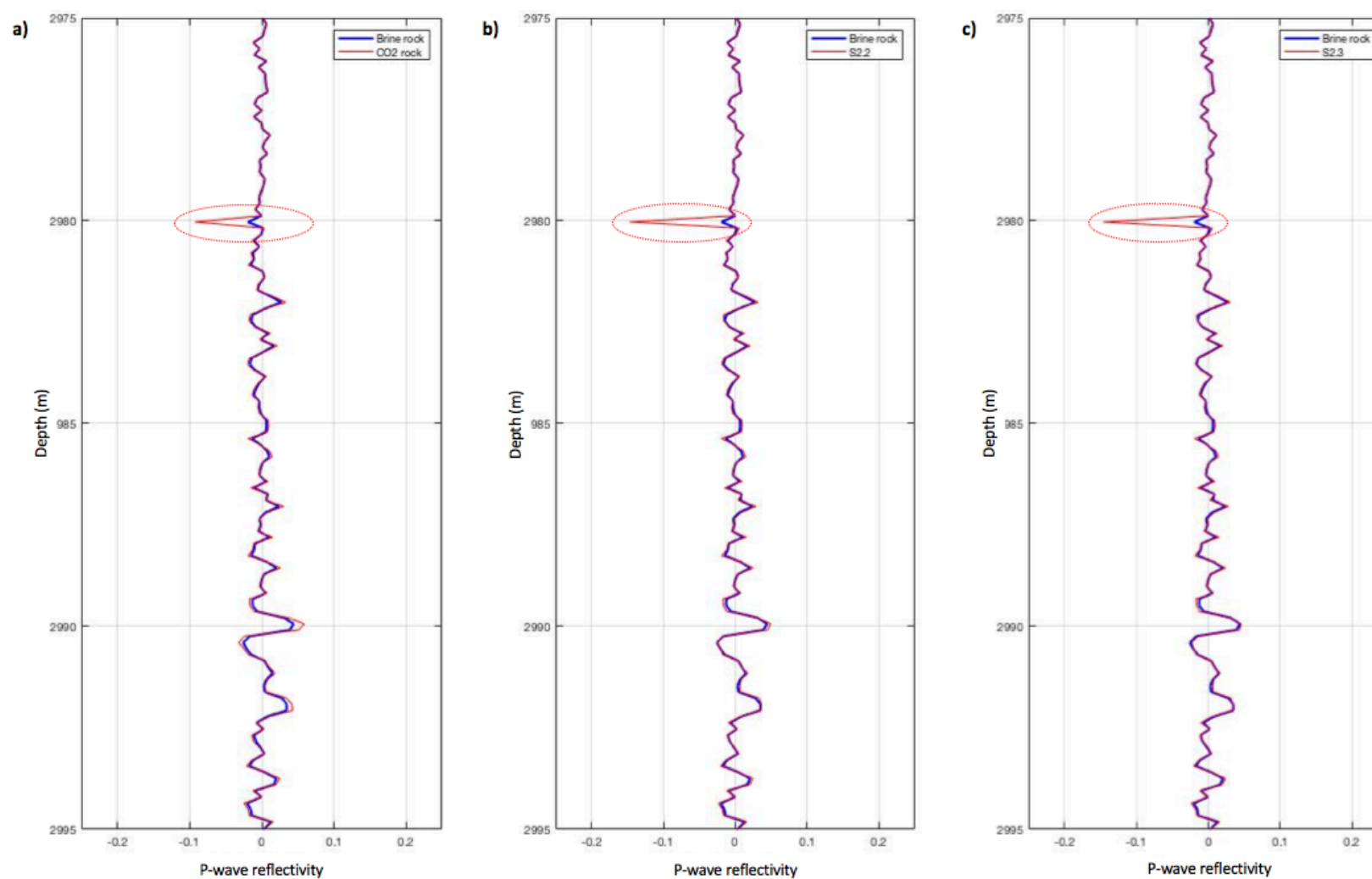
Figures 6.31 and 6.32 display the calculated P-wave reflectivity and gradient using the modelled well data describing scenario 2. It provides a general overview of the alterations induced by fluid substitution and rock-fluid interactions. The brine reservoir is plotted in a blue line, whereas the CO<sub>2</sub> reservoir is plotted in red. The increased porosity resulting from dissolution will contribute to enhance the reflectivity contrast between the brine saturated rock, and the dissolved CO<sub>2</sub> saturated rock. This effect is illustrated in Figure 6.31b. The reflectivity log of the compacted reservoir follows in Figure 6.31c, where increased reflectivity is observed. The gradient does however seem fairly unaffected by the increased porosity and compaction effects.

Figure 6.33 displays a synthetic AVA gather for Scenario 2, modelled using a Ricker wavelet with a peak frequency of 40 Hz. The gathers c) and d) show an increasing amplitude and travel time as a result of the increased porosity and compaction. The effect of increased reflectivity is clearly demonstrated in the zone marked by the red circle. Here, a new positive amplitude appears, that was not visible in gathers a) and b).



**Figure 6.30.** The figure shows the intercept-gradient cross plot for a) brine saturated rock (S2.0) b) CO<sub>2</sub> saturated rock (S2.1) c) dissolved and CO<sub>2</sub> saturated rock (S2.2) and d) compacted and CO<sub>2</sub> saturated rock (S2.3). The reservoir data is plotted as a function of calcite content; the remaining data is plotted in gray.

A more detailed AVA modelling was performed in the top of the reservoir. The target reflector is marked by the red line in Figure 6.33. The gradient versus intercept cross plot in Figure 6.34 demonstrates the effect of fluid substitution and dissolution targeting the pore volume. The gradient increase compared to the initial, brine saturated gradient when alterations in the pore volume is included into the modelling (Figure 6.34c). This gradient effect is opposite of what is displayed in the fluid substitution scenario, and can therefore be a source for misinterpretations.



**Figure 6.31.** The figure compares the P-reflectivity for scenario 2. The blue line represent the brine saturated rock and the red lines in a) the CO<sub>2</sub> saturated rock (S2.1), b) CO<sub>2</sub> saturated and dissolved rock (S2.2) and c) compacted CO<sub>2</sub> rock (S2.3). The red circle marks an anomaly from the brine saturated reflectivity.

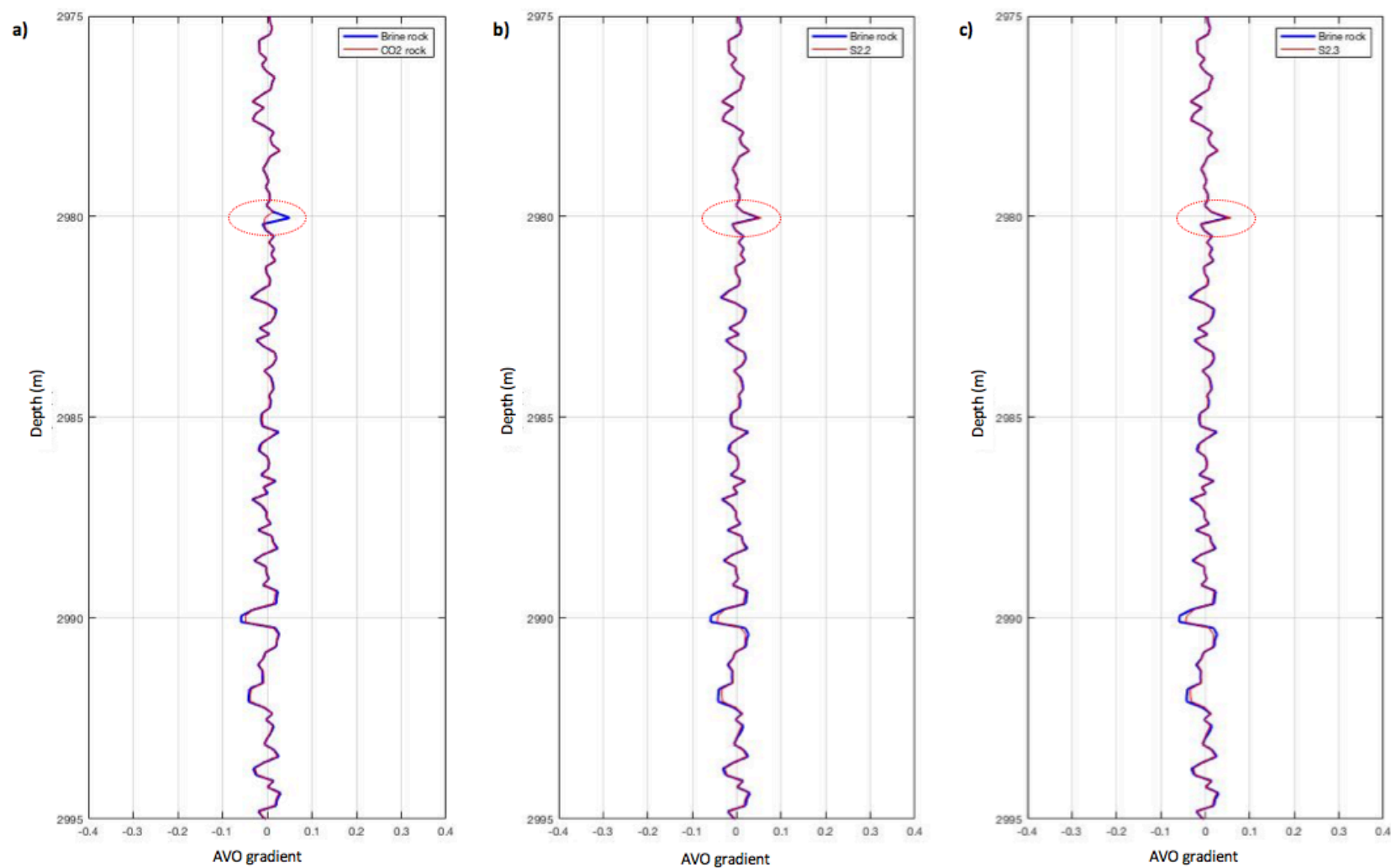


**Figure 6.32.** The figure compares the AVO gradient for scenario 2. The blue line represent the brine saturated rock and the red lines in a) the CO<sub>2</sub> saturated rock (S2.1), b) CO<sub>2</sub> saturated and dissolved rock (S2.2) and c) compacted CO<sub>2</sub> rock (S2.3). The red circle marks an anomaly from the brine saturated reflectivity.

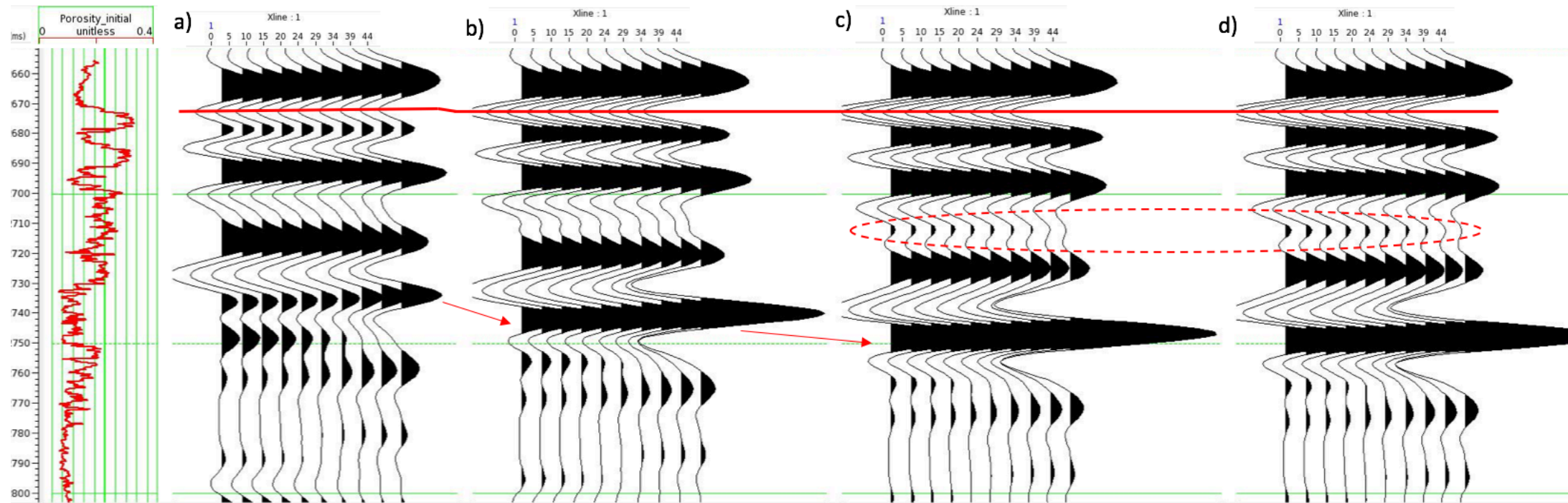


**Figure 6.33.** The figure shows the synthetic AVA gathers for scenario 2 (40 Hz wavelet), displaying the gather for a) brine saturated rock (S2.0), b) CO<sub>2</sub> saturated rock (S2.1), c) CO<sub>2</sub> saturated and dissolved rock (S2.2) and d) CO<sub>2</sub> saturated and compacted rock (S2.3). The red line represents the negative amplitude of which the gradient analysis is performed. The red arrows outline the increasing travel times occurring due to fluid substitution and altered rock fabric. The red circle highlights the new amplitudes occurring due to dissolution and compaction.



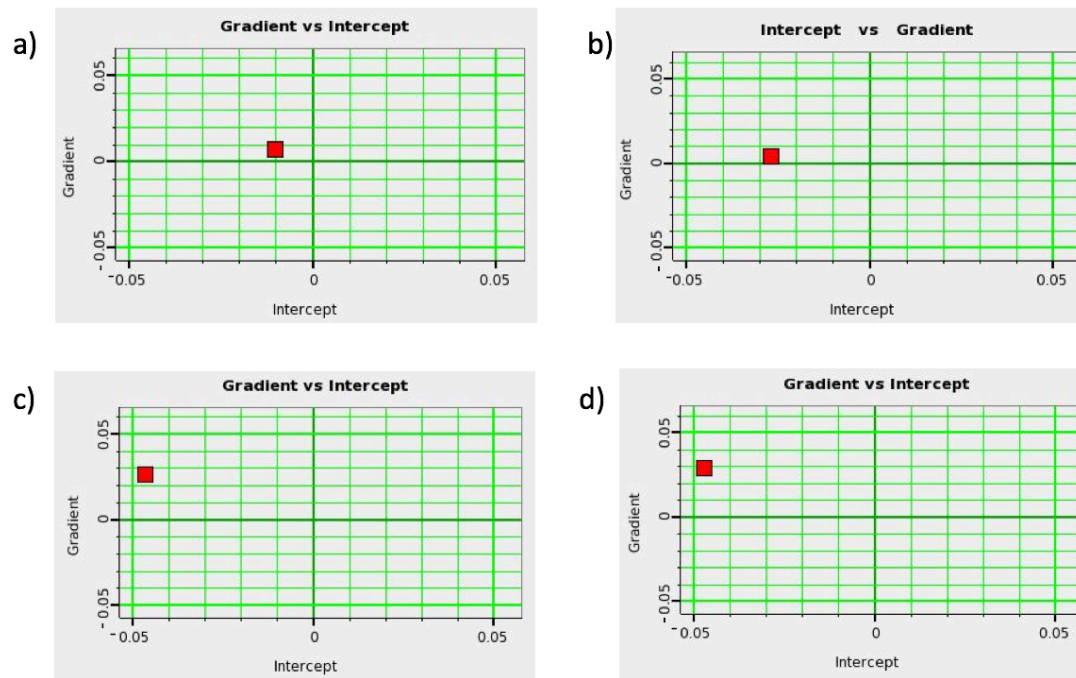


**Figure 6.34.** The figure shows the gradient and intercept for scenario 2 (40 Hz wavelet) for a) initial rock (S2.0), b) CO<sub>2</sub> saturated rock (S2.1), c) CO<sub>2</sub> saturated and dissolved rock (S2.2) and d) CO<sub>2</sub> saturated and compacted rock (S2.3).

An additional synthetic gather is created using a Ricker wavelet with peak frequency of 20 Hz (Figure 6.36). The gradient versus intercept cross plot in Figure 6.35 demonstrates the effect of fluid substitution, and dissolution targeting the pore volume. Compared to the initial, brine saturated rock, the intercept value is reduced following dissolution. However, the intercept for Figures 6.35c and 6.35d are the same, which reveal little reflectivity effect from the compaction. The gradient of the dissolved rock plots at 0, indicating very little amplitude sensitivity to angle (Figure 6.35c). The modelled compaction effects do not contribute to any significant alterations in the gradient, which plot around 0 (Figure 6.35d).



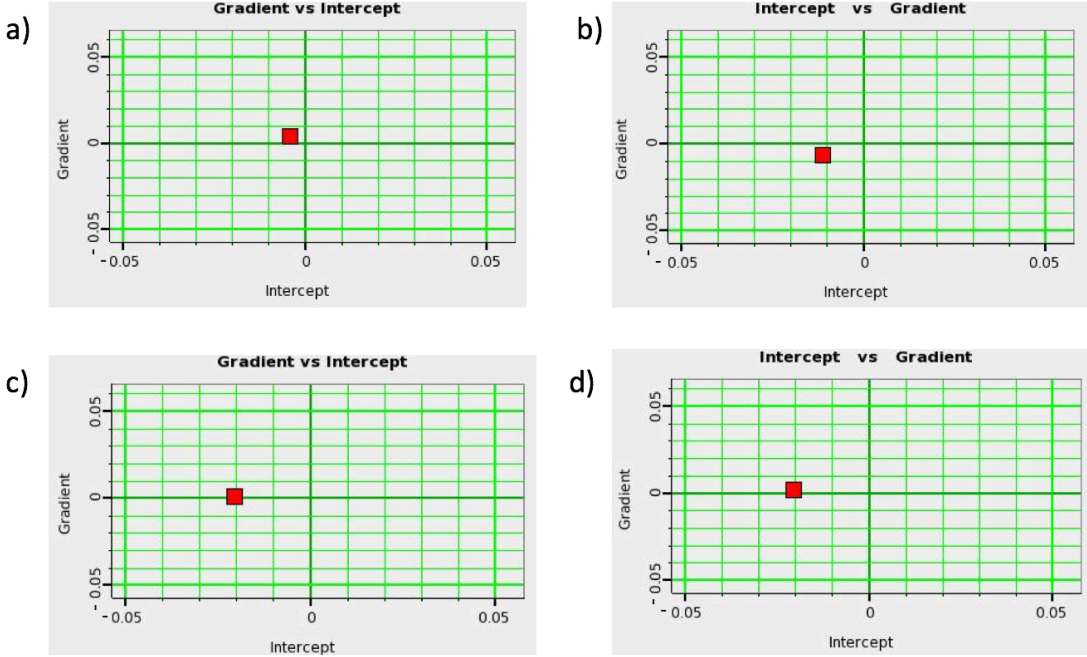


**Figure 6.35.** The figure shows the gradient and intercept for scenario 2 (20 Hz wavelet) for a) initial rock (S2.0), b) CO<sub>2</sub> saturated rock (S2.1), c) CO<sub>2</sub> saturated and dissolved rock (S2.2) and d) CO<sub>2</sub> saturated and compacted rock (S2.3).

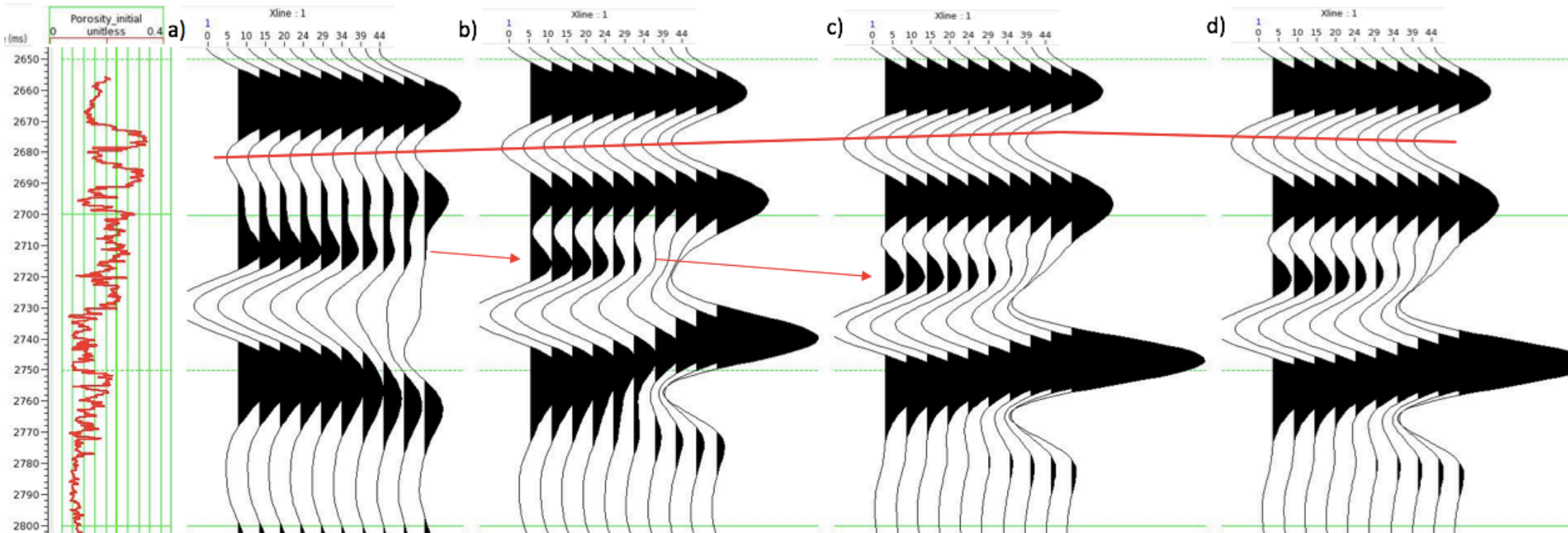


**Figure 6.36.** The figure shows the synthetic AVA gathers for scenario 2 (20 Hz wavelet), displaying the gather for a) brine saturated rock (S2.0), b) CO<sub>2</sub> saturated rock (S2.1), c) CO<sub>2</sub> saturated and dissolved rock (S2.2) and d) CO<sub>2</sub> saturated and compacted rock (S2.3). The red line represents the negative amplitude of which the gradient analysis is performed. The red arrows outline the increasing travel times occurring due to fluid substitution and altered rock fabric.

### 6.5 Scenario Three: The Effect of Reduced Porosity

Scenario 3 represents the effect of precipitation occurring some time after the CO<sub>2</sub> injections. Precipitation is expected to reduce the porosity. The concentration of spherical pores increases on expense of intergranular pores. Table 6.4 summarizes the expected variations in the rock fabric of the carbonate rock. Information regarding scenario 3 is provided in section 5.2.1. The effect of fluid substitution is not evaluated in detail, but included in the figures.

	$\Delta\phi$	Cracks	Spherical pores	Intergranular pores	Dissolved carbonate minerals in pore fluid
<b>Initial P<sub>p</sub></b>	-	-	+	-	-
<b>Increased P<sub>p</sub></b>	~0	+	~0	-	~0

**Table 6.4.** The table summarizes the effect of CO<sub>2</sub> injections in scenario 3. +/- represent increasing or decreasing concentration, ~0 means no variation is assumed

#### 6.5.1 Elastic Properties and Density

This section evaluates the alterations in elastic properties and density following precipitation of carbonate minerals. Carbonate precipitation is included in the modelling by reducing the concentration of intergranular pores and increasing the concentration of spherical pores. The porosity is reduced by 5%.

Figure 6.37b demonstrates the effect of porosity reductions on the bulk modulus. As the porosity is reduced, the bulk modulus increases compared to that of the CO<sub>2</sub> saturated rock in Figure 6.37a. However, the bulk modulus of the CO<sub>2</sub> saturated and precipitated rock is still lower than that of the initial, brine saturated rock (blue line). Figure 6.37c displays the effect of increasing the pore-pressure. As the reservoir is stiffened, compaction is not evaluated. The increased pore-pressure is assumed to follow pore-throat clogging, and displays little effect on the bulk modulus.

The shear modulus demonstrates a significant increase as the pore volume is reduced, as illustrated in Figure 6.38b. As for the bulk modulus, little variation is observed in shear modulus following increased pore-pressure (Figure 6.38c).

The effect of precipitation on the reservoir density is illustrated in Figure 6.39b. Compared to the density of the initial CO<sub>2</sub> saturated rock in Figure 6.39a, the reduced porosity induces a significant increase in density. Increasing the pore-pressure contributes to higher density values in the well data (Figure 6.39c).

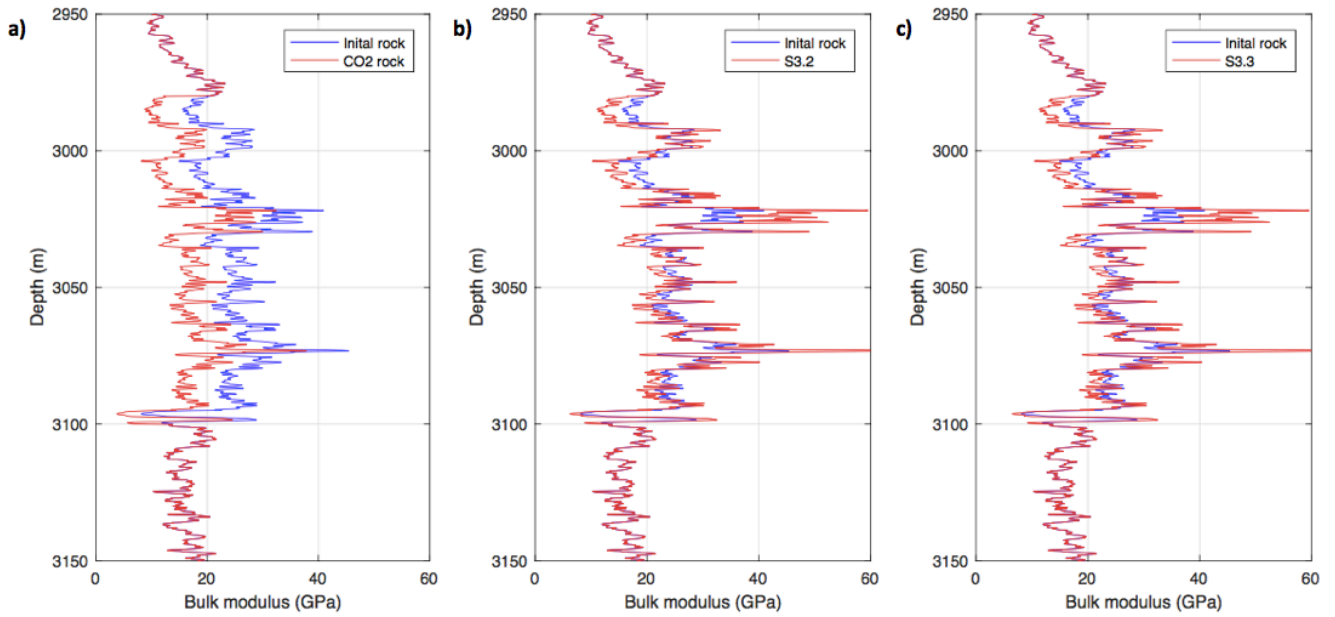


**Figure 6.37.** The figure shows the variation in brine saturated (blue) reservoir bulk modulus and a) CO<sub>2</sub> saturated reservoir (S3.1), b) precipitated reservoir (S3.2) and c) increased pore-pressure (S3.3).

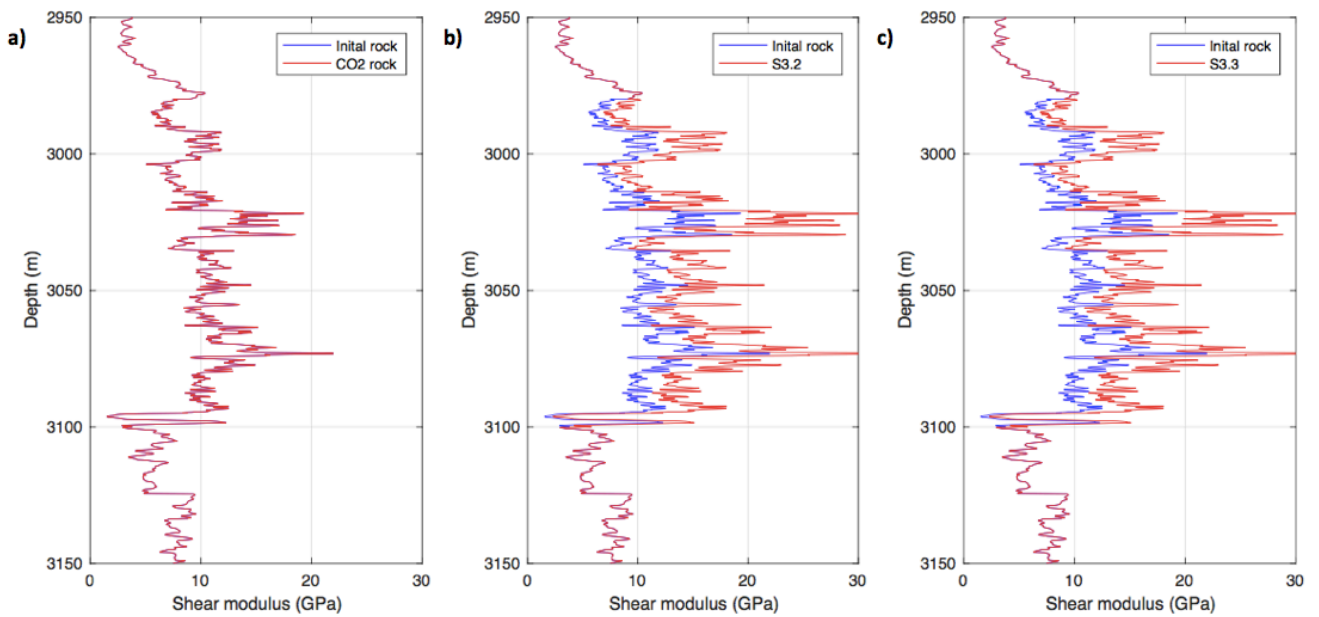


**Figure 6.38.** The figure shows the variation in brine saturated (blue) reservoir shear modulus and a) CO<sub>2</sub> saturated reservoir (S3.1), b) precipitated reservoir (S3.2) and c) increased pore-pressure (S3.3).

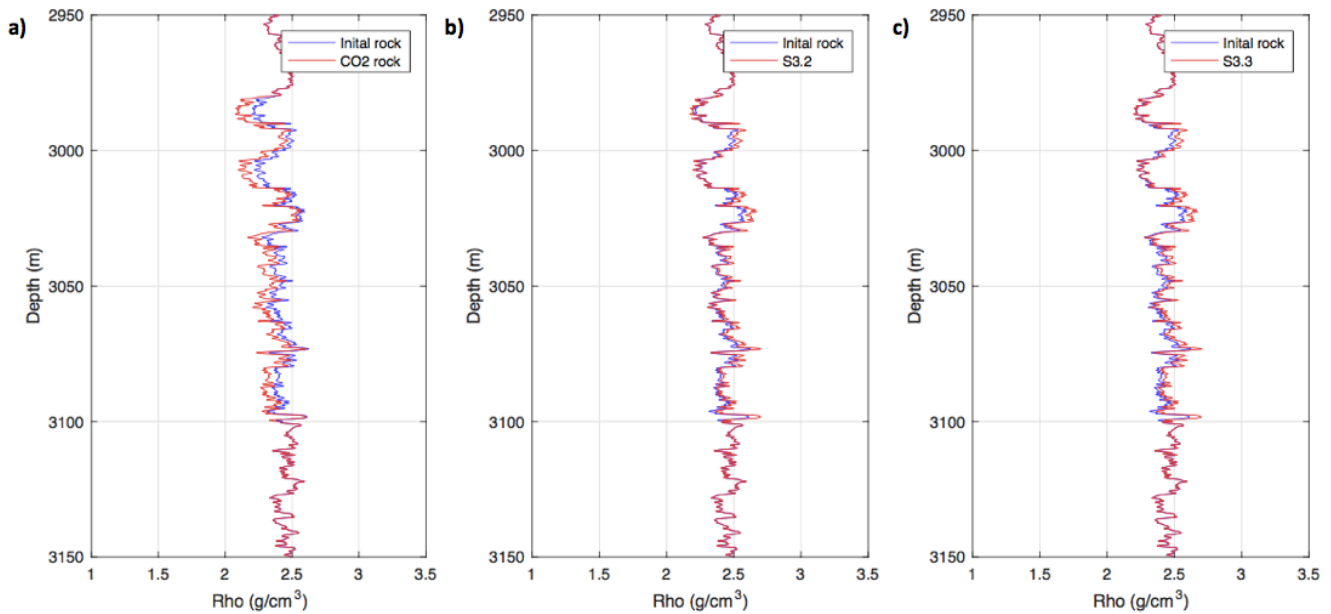


**Figure 6.39.** The figure shows the variation in brine saturated (blue) reservoir density and a) CO<sub>2</sub> saturated reservoir (S3.1), b) precipitated reservoir (S3.2) and c) increased pore-pressure (S3.3).

### 6.5.2 Seismic Velocity and Acoustic Impedance

The effect of precipitation and reduced porosity on the seismic velocity will be evaluated in this section. Figures 6.40b and 6.41b demonstrates increased P- and S-wave velocity following precipitation effects in the CO<sub>2</sub> saturated rock. Increased pore-pressure does however exhibit little effect on either of the seismic velocities (Figures 6.40c and 6.41c).

Figure 6.42 shows the rock physics template for scenario 3, where Figure 6.42c displays the precipitation effect on the velocity ratio and acoustic impedance. Compared to the CO<sub>2</sub> saturated reservoir displayed in Figure 6.42b, both the acoustic impedance and velocity ratio is increased. The effect of increased pore pressure does not seem to affect either the acoustic impedance or the velocity ratio noticeably (Figure 6.42 d).

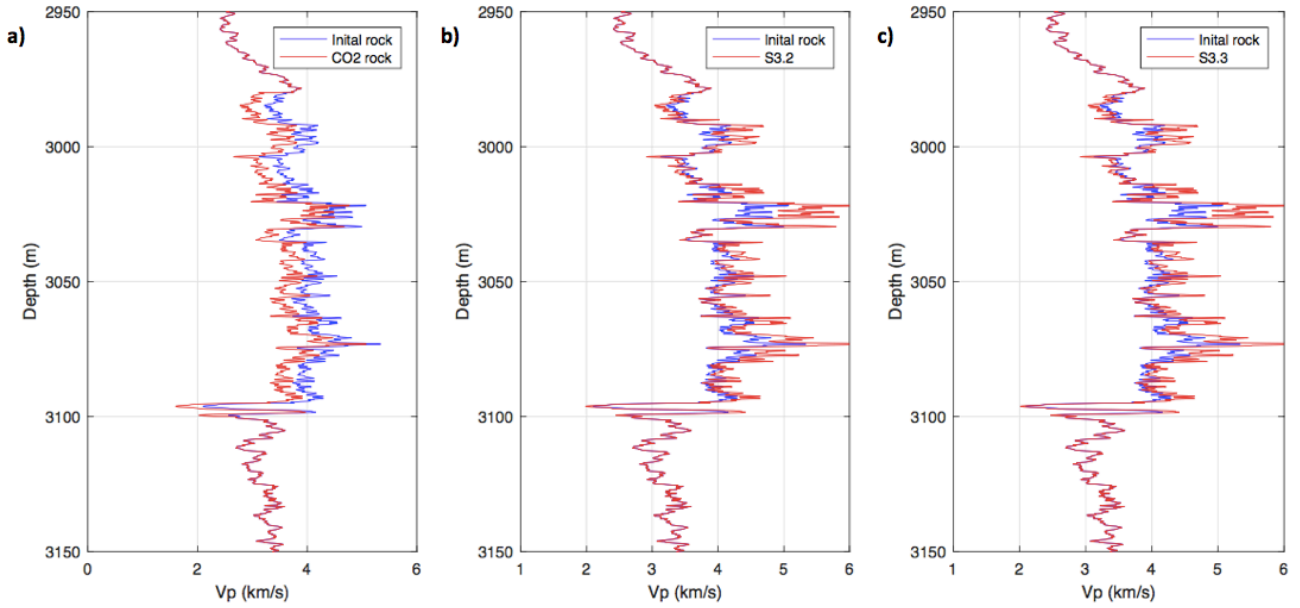


**Figure 6.40.** The figure displays the contrast in P-wave velocity of brine saturated rock (blue) and a) CO<sub>2</sub> saturated reservoir (S3.1), b) precipitated reservoir (S3.2) and c) increased pore-pressure (S3.3).

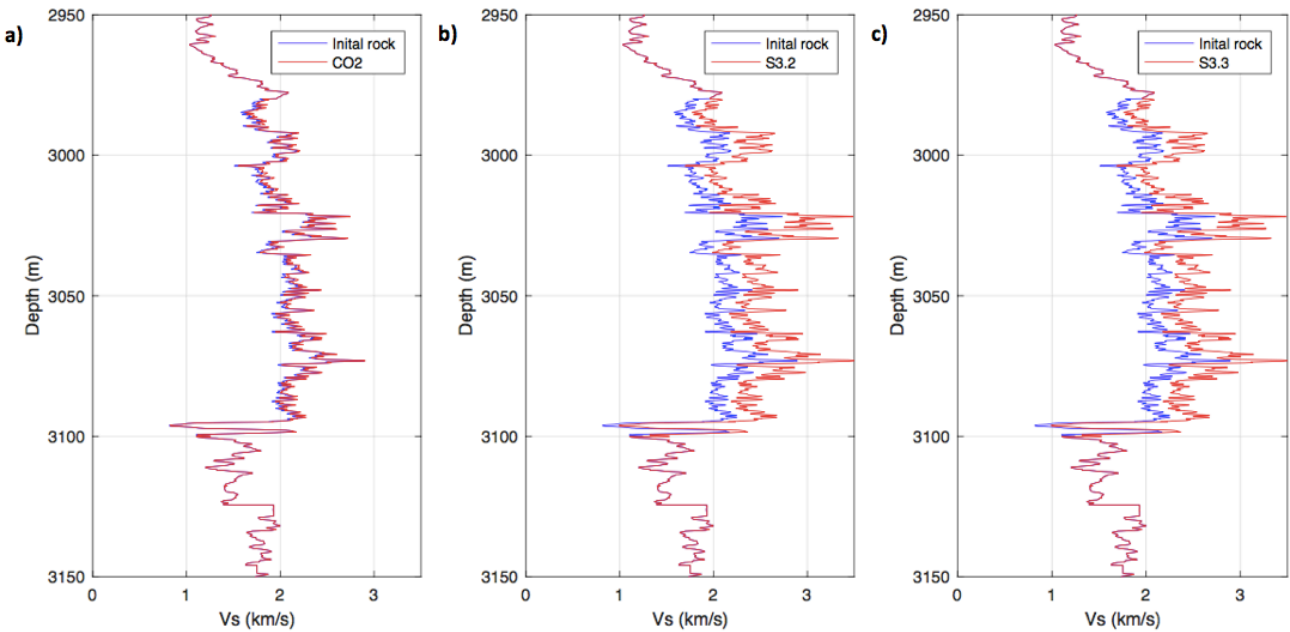


**Figure 6.41.** The figure displays the contrast in S-wave velocity of brine saturated rock (blue) and a) CO<sub>2</sub> saturated reservoir (S3.1), b) precipitated reservoir (S3.2) and c) increased pore-pressure (S3.3).

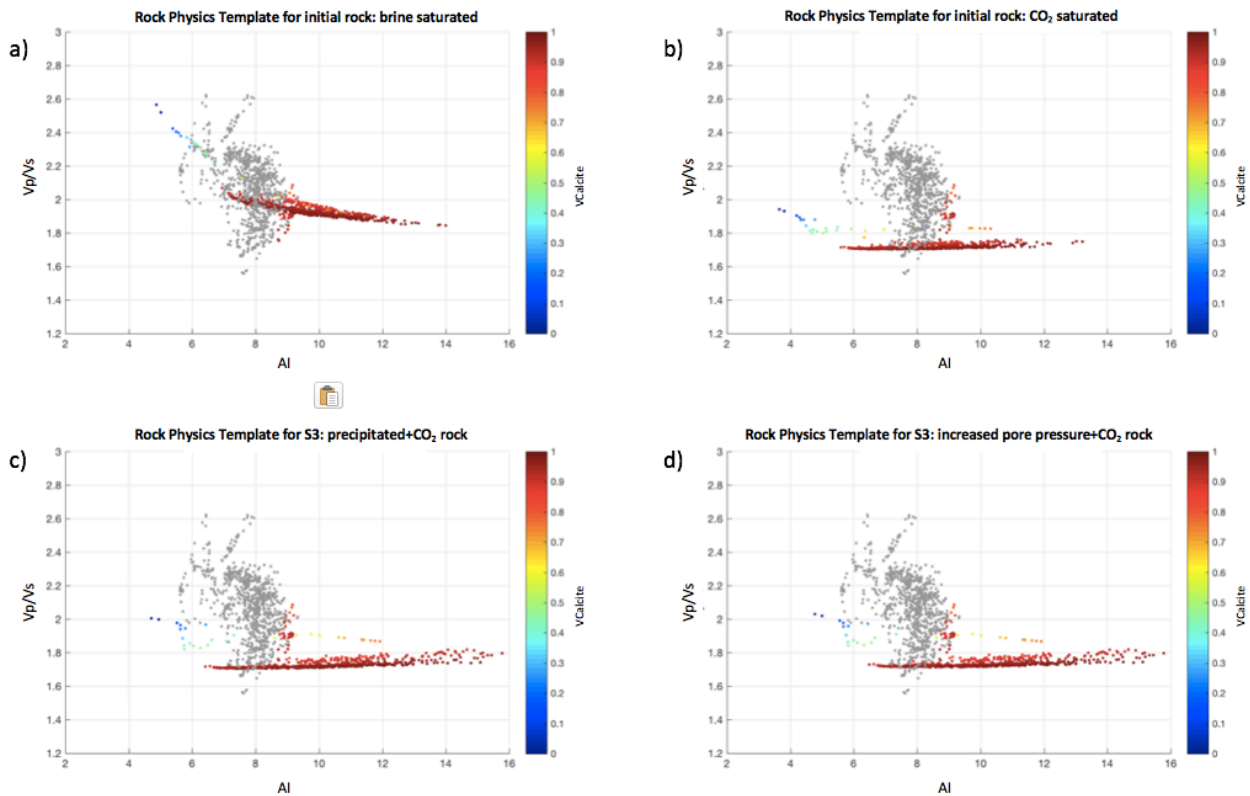


**Figure 6.42.** The figure shows the rock physics template of scenario 3 for a) the initial rock (S3.0), b) CO<sub>2</sub> saturated rock (S3.1), c) precipitated rock (S3.2) and d) increased pore-pressure (S3.3). The reservoir data is plotted as a function of calcite content; the remaining data is plotted in gray.

### 6.5.3 Amplitude Versus Angle Analysis

Figure 6.43 displays the intercept versus gradient cross plot for scenario 3. Following both reduced porosity and compaction, it can seem as more of the dataset now plots closer to the background trend compared to the cross-plot in Figure 6.43b.

The calculated P-wave reflectivity log is plotted in Figure 6.44. The brine saturated reflectivity is plotted in blue and the CO<sub>2</sub> saturated reflectivity in red. The modelled P-wave reflectivity of the reservoir zone experiencing precipitation is plotted in Figure 6.44b. Reducing the porosity of the reservoir induce a higher reflectivity compared to both the initial brine- and CO<sub>2</sub> saturated reservoir. Figure 6.43c reveals that there is no obvious variation between the reflectivity of the reservoir model experiencing increased pore-pressure compared to the reflectivity plot representing the precipitated CO<sub>2</sub> rock.

Figure 6.45 shows the gradient log for the top reservoir zone in scenario 3. The effect of precipitation and stiffening of the CO<sub>2</sub> saturated rock frame is plotted in red in Figure 6.45b. It is difficult to spot a general trend on the gradient of the modified rock frame. However, some



differences are observed. The zone marked by a red circle demonstrates a gradient shift as the porosity is reduced, and is a clear anomaly from the brine saturated gradient.

Figure 6.46 displays a synthetic AVA gather for scenario 3, modelled using a Ricker wavelet with a peak frequency of 40 Hz. Gather c) displays the effect of reducing the porosity, and show higher amplitudes than the brine saturated rock. Little variation is observed in the synthetic gather following the increased pore-pressure in gather d). A more detailed AVA modelling was performed in the top of the reservoir. The target reflector is marked by the red line in Figure 6.46. A gradient versus intercept cross plot for the top reservoir is presented in Figure 6.47.

Figures 6.47c and 6.47d represent the effect of precipitation and increased pore-pressure. The intercept values are less negative compared to that of the initial, CO<sub>2</sub> saturated rock. Both gradients do however display negative values, whereas the gradient considering only the fluid effects displays a positive value (Figure 6.47b). Thus, a completely different AVA response is predicted when the effect of precipitation is included in the modelling.

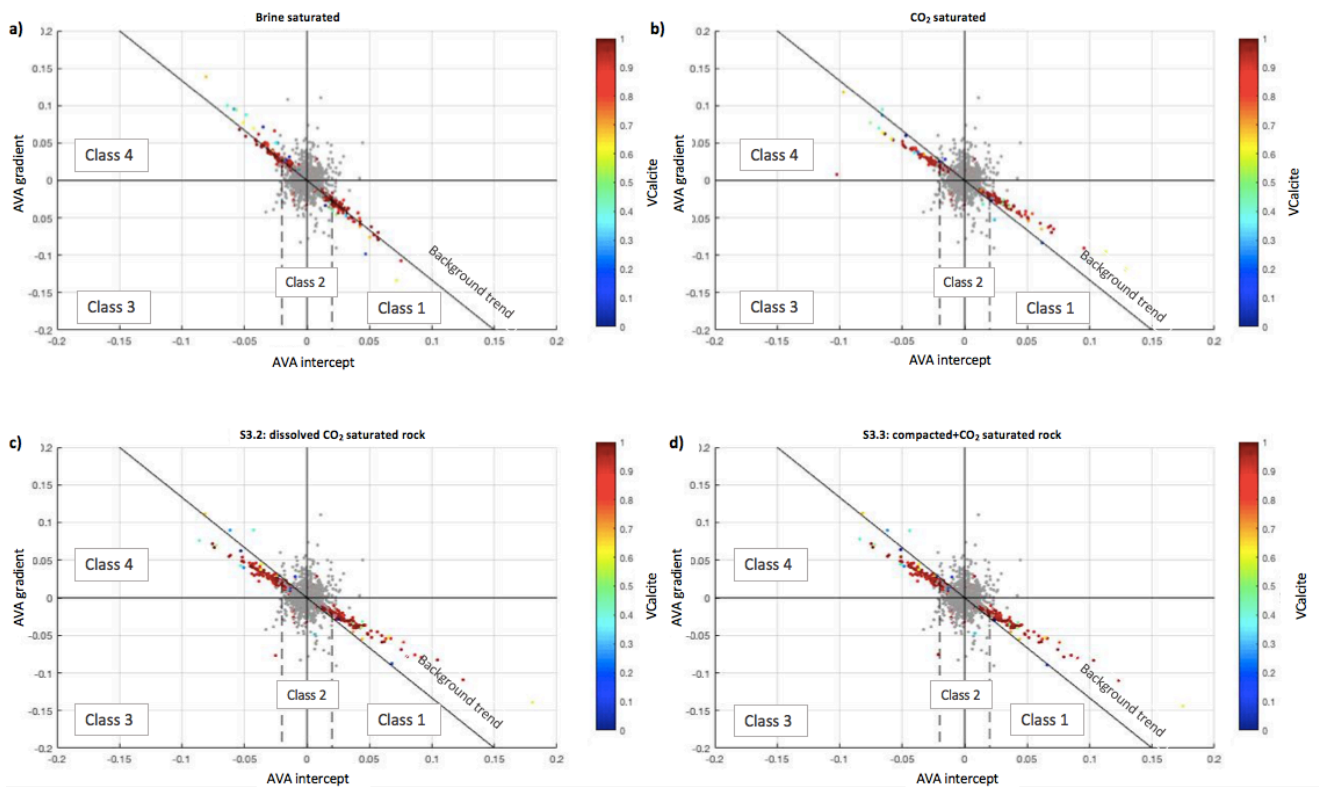


**Figure 6.43.** The figure shows the intercept-gradient cross plot for a) brine saturated rock (S3.0) b) CO<sub>2</sub> saturated rock (S3.1) c) precipitated and CO<sub>2</sub> saturated rock (S3.2) and d) increased pore-pressure (S1.3). The reservoir data is plotted as a function of calcite content; the remaining data is plotted in gray.



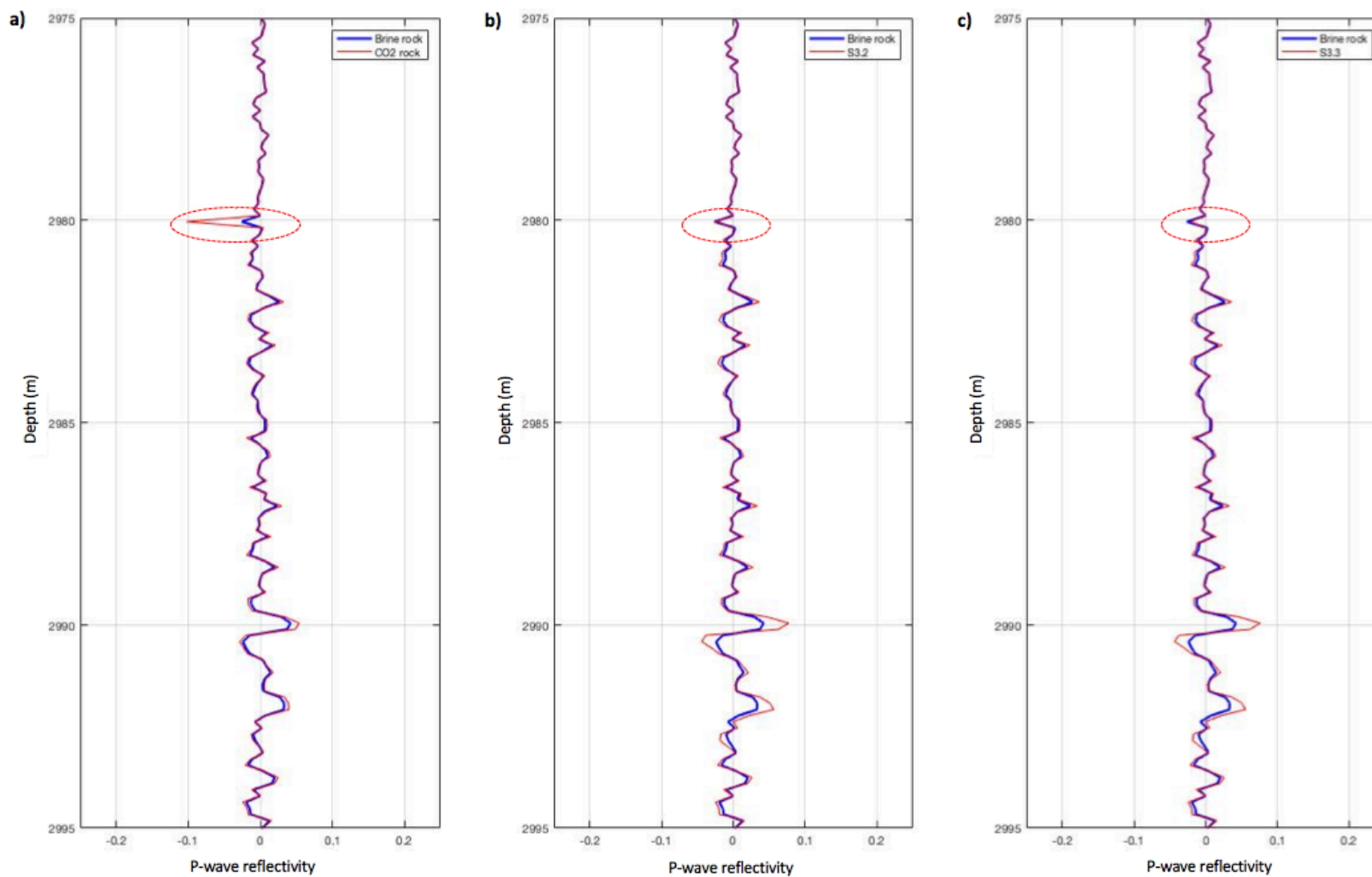


**Figure 6.44.** The figure compares the P-reflectivity for scenario 3. The blue line represent the brine saturated rock and the red lines in a) the CO<sub>2</sub> saturated rock (S3.1), b) CO<sub>2</sub> saturated and precipitated rock (S3.2) and c) increased pore-pressure (S3.3). The red circle marks an anomaly from the brine saturated reflectivity.

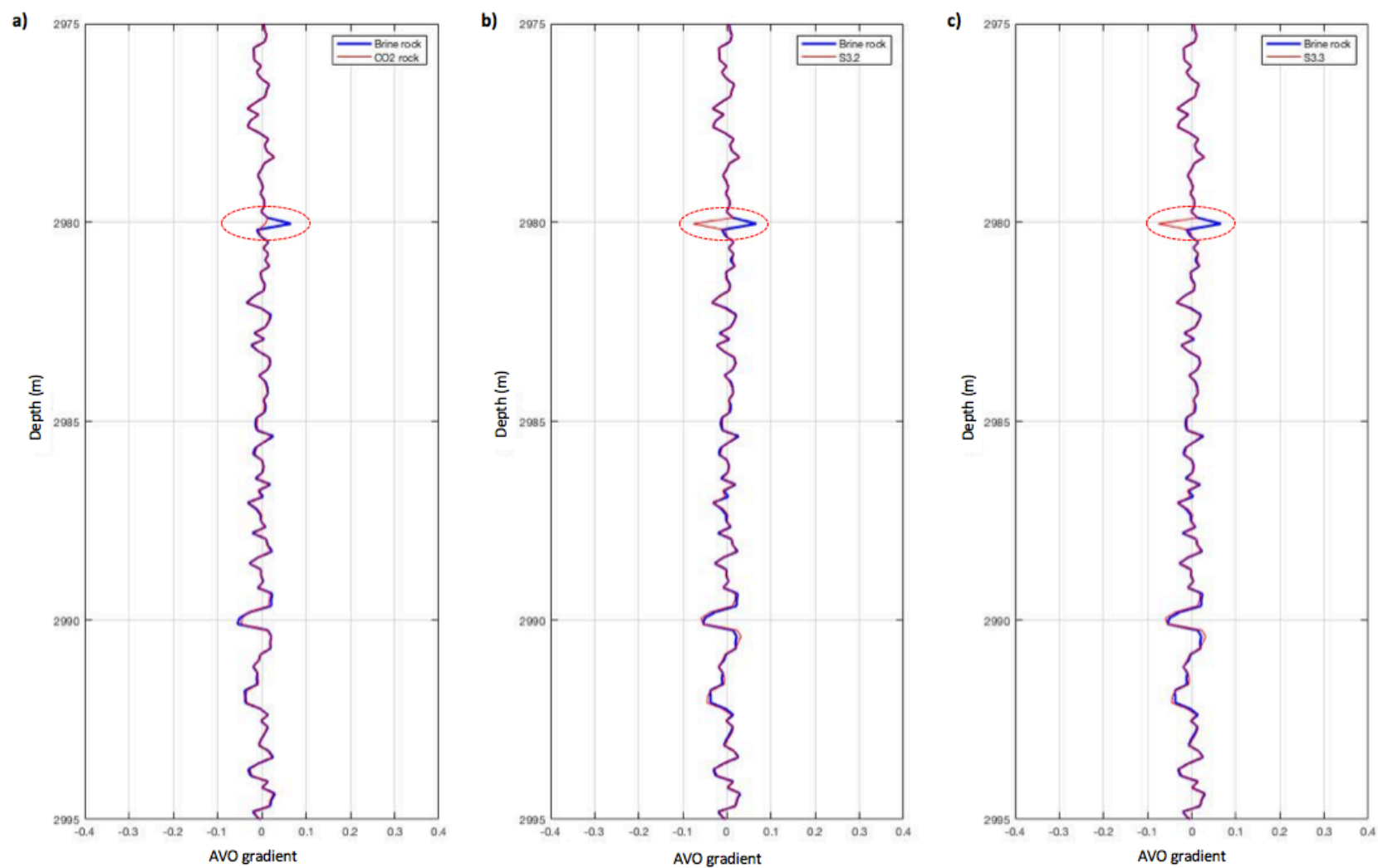


**Figure 6.45.** The figure compares the AVO gradient for scenario 3. The blue line represent the brine saturated rock and the red lines in a) the CO<sub>2</sub> saturated rock (S3.1), b) CO<sub>2</sub> saturated and precipitated rock (S3.2) and c) increased pore-pressure (S3.3). The red circle marks an anomaly from the brine saturated reflectivity.

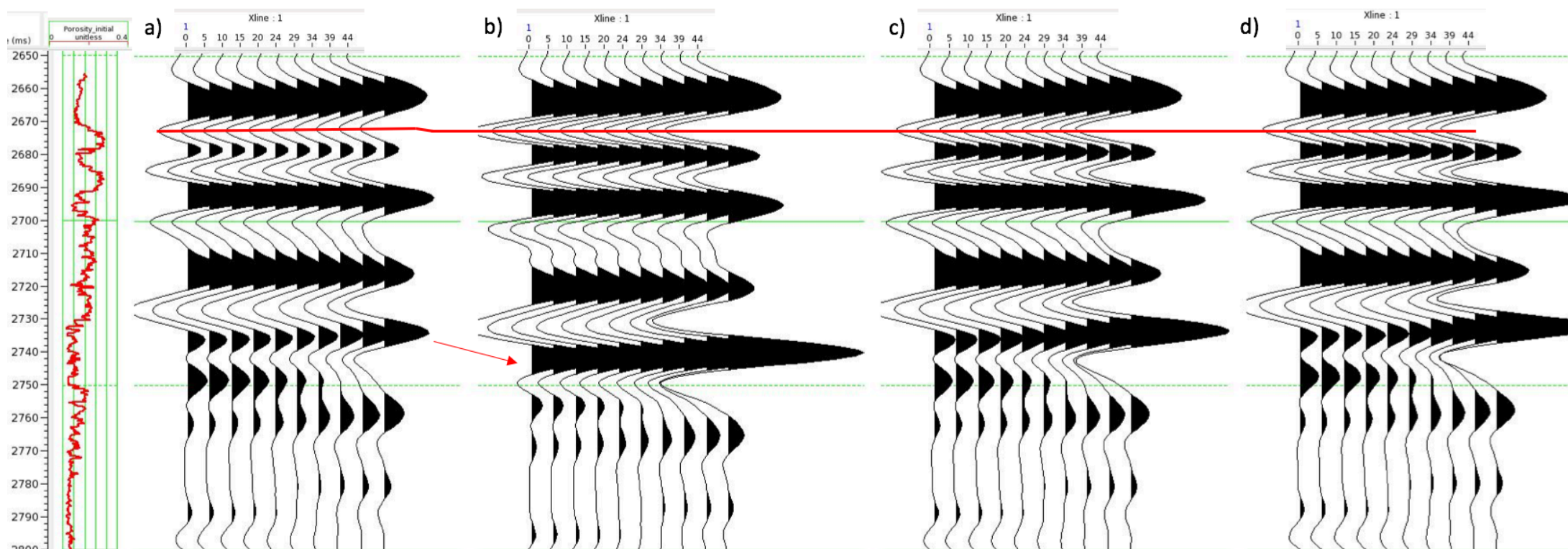


**Figure 6.46.** The figure shows the synthetic AVA gathers for scenario 3 (40 Hz wavelet), displaying the gather for a) brine saturated rock (S3.0), b) CO<sub>2</sub> saturated rock (S3.1), c) CO<sub>2</sub> saturated and precipitated rock (S3.2) and d) increased pore-pressure (S3.3). The red line represents the negative amplitude of which the gradient analysis is performed. The red arrows outline the increasing travel times occurring due to fluid substitution and altered rock fabric.

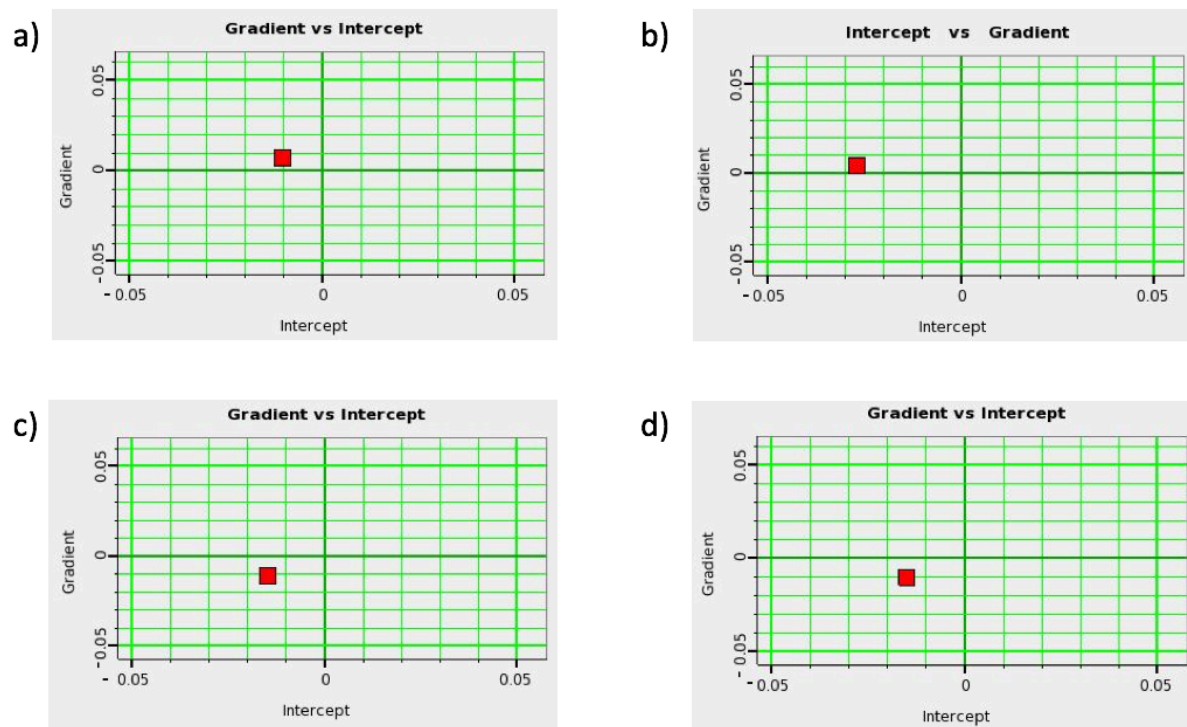


**Figure 6.47.** The figure shows the gradient and intercept for scenario 3 (40 Hz wavelet) for a) initial rock (S3.0), b) CO<sub>2</sub> saturated rock (S3.1), c) CO<sub>2</sub> saturated and precipitated rock (S3.2) and d) CO<sub>2</sub> saturated with increased pore-pressure (S3.3).

An additional synthetic gather is created, using a Ricker wavelet with peak frequency of 20 Hz (Figure 6.49). Figure 6.48c demonstrates the gradient versus intercept cross plot for the precipitated reservoir. Here, the gradient is slightly more negative compared to that of the initial CO<sub>2</sub> saturated reservoir (Figure 6.48b). Little variation in gradient occurs following increased pore-pressure (Figure 6.48d). The intercept value of the precipitated reservoir plots close to the zero axis in both 6.48c and 6.48d.

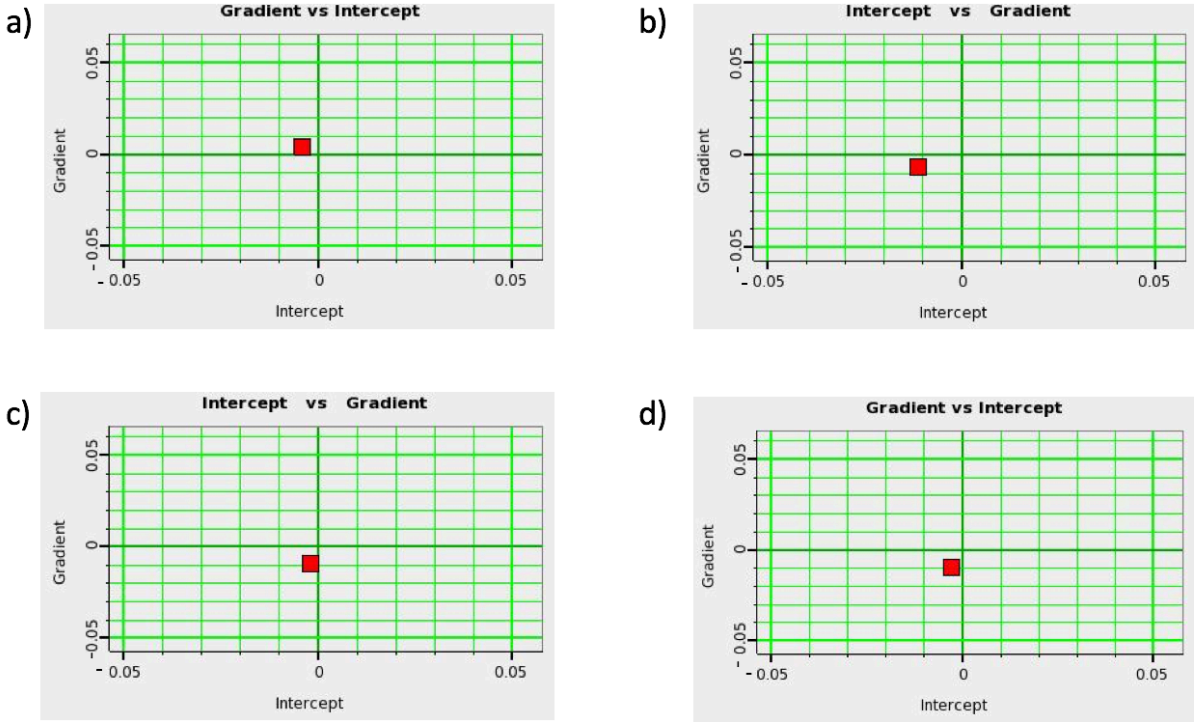


**Figure 6.48.** The figure shows the gradient and intercept for scenario 3 (20 Hz wavelet) for a) initial rock (S3.0), b) CO<sub>2</sub> saturated rock (S3.1), c) CO<sub>2</sub> saturated and precipitated rock (S3.2) and d) CO<sub>2</sub> saturated with increased pore-pressure (S3.3).



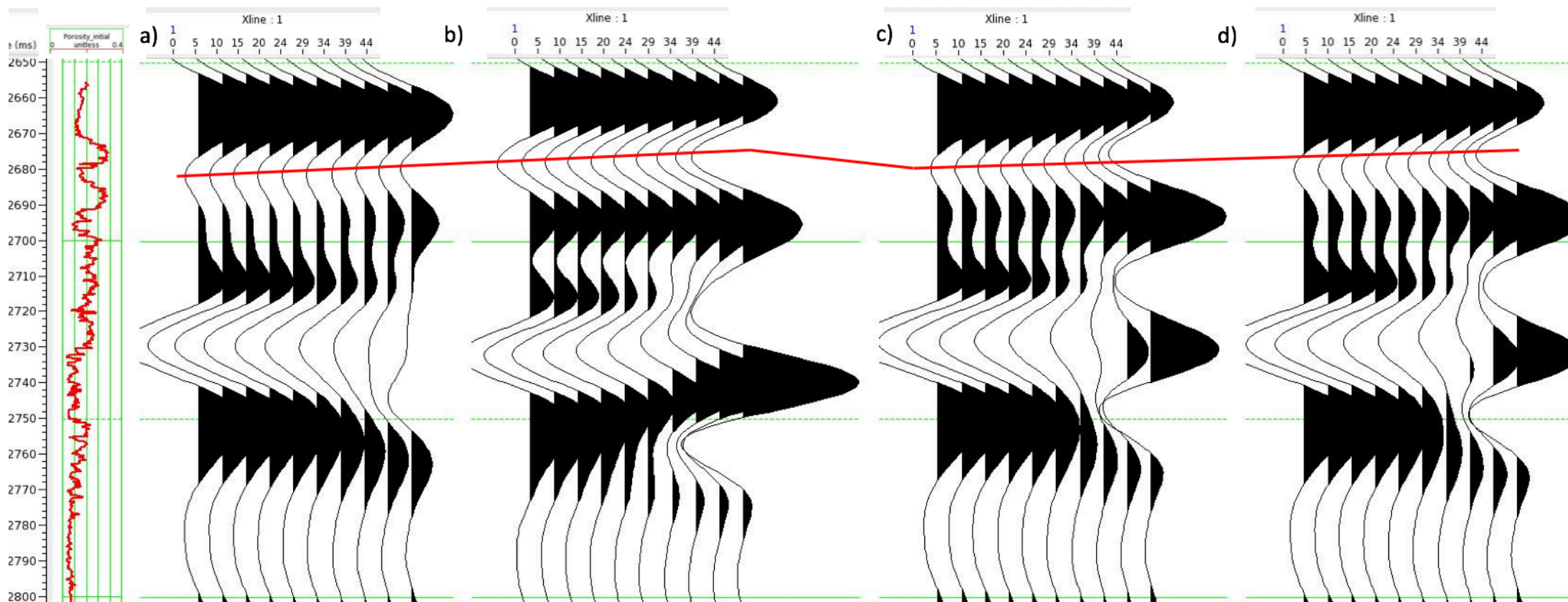


**Figure 6.49.** The figure shows the synthetic AVA gathers for scenario 3 (20 Hz wavelet), displaying the gather for a) brine saturated rock (S3.0), b) CO<sub>2</sub> saturated rock (S3.1), c) CO<sub>2</sub> saturated and precipitated rock (S3.2) and d) increased pore-pressure (S3.3). The red line represents the negative amplitude of which the gradient analysis is performed.

## 7 Discussion

The focus of this thesis has been to establish the seismic effect of geochemically induced alterations from rock-fluid interactions on a carbonate reservoir. This discussion will emphasize on the overall seismic trends caused by variations in rock properties and saturation effects. In addition, a brief discussion of the wavelet effect will be presented. Finally, a small evaluation of the reliability of the results are provided.

### 7.1 Saturation Effects on Seismic Properties

Modelling the effect of replacing brine with CO<sub>2</sub> using the Gassmann equation, reveals no surprises. Increasing the CO<sub>2</sub> saturation yields lower density and bulk modulus, while the shear modulus is unchanged (Figure 6.2). These effects will contribute to both reduced P-wave velocity and increased S-wave velocity. Consequently, the velocity ratio is lowered. These observations are reasonable considering the factors controlling the seismic velocities. The P-wave velocity is controlled by the bulk modulus and density of the fluid, whereas the S-wave velocity is only affected by the fluid density (Wang, 1997).

The effect of pore fluids on the seismic velocities is modelled using Gassmann theory. It is therefore assumed that the pores are fully connected. If they are not, the fluid effect might be lower than what is predicted in the provided results (Adam et al., 2006). Knowing that carbonate rocks can contain high concentrations of isolated inclusions, this assumption can be a source of modelling errors.

### 7.2 Effect of Porosity and Pore Shape on Seismic Properties

#### *The effect of altered pore geometries on the seismic properties*

Wang (1997) suggests that the pore geometry acts as an equally important contributor to velocity variations in carbonate rocks as the porosity. By increasing the concentration of cracks in the rock model, both P- and S-wave velocities are reduced compared to the initial CO<sub>2</sub> saturated rock (Figures 6.14b and 6.15b). Thin and flat pores will reduce the rock stiffness, making it easier to deform (Anselmetti and Eberli, 1997; Wang, 1997). This suggestion provides an explanation for the observed velocity reductions, as the reduced stiffness will affect the elastic properties. Thus, by including dissolution effects in the modelling, the velocity reductions as a response to fluid substitution are larger than what is predicted when considering

only the fluid effects. Similar observations have been presented by e.g. Grombacher et al. (2012).

The velocity ratio increase as cracks are introduced in the model (Figure 6.16c). It is suggested that by increasing the concentration of cracks, the rock exhibit fluid-like properties, consequently affecting the velocity ratio (Guéguen et al., 2009). The S-wave velocity is more sensitive to the introduction of cracks (Wilkens et al., 1984). Thus by introducing even small concentrations of cracks, the velocity ratio is predicted to display significantly increased values (Tatham, 1982).

### *The effect of altered pore volume on the seismic properties*

Velocity reductions following a 5% increment in porosity are displayed in Figures 6.27b and 6.28b. This result is in accordance with Wang (1997), suggesting that increasing the porosity induce lower seismic velocities. The density displays a reduction from loss of solid rock frame. From the definition of the seismic velocities (Eq.3.1 and 3.3), reduced density should correspond to a positive velocity variation. However, Wang (1997) suggests that the elastic properties usually are more affected by the altered porosity than the density is. The reductions in both bulk and shear modulus is presented in Figures 6.24b and 6.25b, and contribute to the observed velocity variations. Experimental results presented in Figure 4.1 by Vanorio et al. (2011) correspond well with the observations revealing the effect of increased porosity on the elastic properties.

Following a 5% reduction in porosity, the P-and S-wave velocities display a general increase compared to the initial brine and CO<sub>2</sub> saturated rock (Figures 6.40 and 6.41). Both these observations indicate a stiffening effect. However, the bulk modulus of the precipitated *and* CO<sub>2</sub> saturated rock is smaller than that of the brine saturated rock. The shear modulus displays a significant increase. These observations are supported by research results presented by Vanorio et al. (2011), indicating that the elastic properties respond differently to precipitation effects.

Anselmetti and Eberli (1997) reveal an inverse relationship between porosity and velocity ratio in the Maiella limestone. As limestone consist mostly of calcite, this is assumed to be a fair comparison for the dataset used in this thesis. The results of this study correspond well with these observations. Increased porosity induces reductions in velocity ratio, whereas porosity reductions displays increased velocity ratios compared to the initial CO<sub>2</sub> saturated rock model (Figures 6.29c and 6.42c respectively).



Weakening of the rock frame following rock-fluid interactions has been proposed as an explanation for the poor correlation between the calculated (based on Gassmann) and measured seismic velocities (Vialle and Vanorio, 2011). The modelled effect of these fabric alterations correspond well with various experimental results, displaying velocity variations larger than what is predicted by only considering the fluid effects (Grombacher et al., 2012; Vanorio et al., 2008; Vialle and Vanorio, 2011). These observations underline the large effect pore geometries and pore volume can display on the seismic properties. Failing to create a realistic rock model enhance the chances of misinterpreting provided seismic data. Thus, by including these effects in forward rock physics models one might be able to create a more accurate simulation of the expected fluid response.

### 7.3 Compaction Effects on the Seismic Properties

Reduced stiffness in the rock frame from dissolution leads to compaction and grain sliding, deforming the less compliant pores (Vanorio, 2015). As the reservoir is compacted mechanically, the pore-pressure increase following closing of pore throats, restricting the fluid flow (Thomas Hantschel and Kauerauf, 2009). In this study an overpressure of 11 MPa is included in the modelling. As the confining pressure is assumed constant, the effective pressure is reduced following the modelled pore-pressure alterations.

Batzle and Wang's (1992) equations describe the effect of increased pore-pressure on reservoir fluids. Results from experiments indicate that both the density and bulk modulus of the pore fluids should increase following overpressure (Walls and Dvorkin, 2005). The variations in CO<sub>2</sub> properties resulting from temperature and pore-pressure are described by Span and Wagner's (1996) equation of state. Figures 3.8 and 3.9 show the CO<sub>2</sub> and brine response to both pore-pressure and temperature. Here, the density and bulk modulus of both fluids demonstrate a proportional relationship to pore-pressure.

Increasing the pore-pressure is however believed to reduce the seismic properties of the dry rock (Siggins and Dewhurst, 2003). As a result, these factors will counteract one another. The modelling procedure only considers variations in fluid properties following pore-pressure alterations. Nevertheless, as the modelled pore-pressure increase, the effective pressure is reduced. The altered effective pressure will contribute to reductions in the seismic velocities of the rock frame (Avseth et al., 2005). Also, the modelled compaction effects altering the pore geometry will contribute to variations in the properties of the dry rock frame.

The effect of compacting the reservoir model already holding a high concentration of cracks induce reductions in both the P- and S-wave velocities (Figure 6.14c and 6.15c). As the pore geometry is altered following the compaction effects, it is difficult to distinguish between the effect of pore-pressure and pore geometry on the seismic properties.

Velocity reductions also follows the increased pore-pressure and compaction effects in the rock holding enhanced pore volume (Figure 6.27c and 6.28c.) As the velocities in both these cases are reduced, it can be concluded that the reduced stiffness of the rock frame overwrites the stiffening effect increased pore-pressure displays on the fluids.

The response of increased pore-pressure alone is displayed in Figures 6.40c and 6.41c (scenario 3). The P-wave velocity increase, whereas the S-wave velocity is slightly reduced. As the rock fabric is stiff (dominated by spherical pores), no alterations in pore geometry occurs as a response to compaction.

It is suggested by Christensen and Wang (1985), that the variations in seismic velocity following increased pore-pressure is related to the grain stiffness. Consequently, the velocity response will vary depending on the initial stiffness of the over-pressured reservoir. The discussed effects of compaction are not very large, and might not cause any significant anomalies in a seismic image.

#### **7.4 Amplitude Versus Angle Response**

Four AVA classes are observed in the intercept versus gradient cross plots of the well data (Figures 6.5, 6.17, 6.30 and 6.43). This observation agrees with Li et al.'s (2003) suggestion that all four classes are present in a carbonate rocks.

The effect of fluid substitution on AVA gradient- and reflectivity logs are presented in Figure 6.6. The P-wave reflectivity increase, making the amplitudes stronger following fluid substitution, whereas the gradient is reduced in positivity. These effects follow Equations 3.33 and 3.32, describing the calculated P-wave reflectivity and gradient. Considering the large reduction in both seismic velocity and density following fluid substitution, these results are reasonable. The alteration in gradient indicates that the AVA variation is more dominating in the brine saturated reservoir compared to the CO<sub>2</sub> saturated reservoir. Similar observations have been presented by other authors, evaluating the effect of CO<sub>2</sub> injections in subsurface reservoirs (Ma and Morozov, 2010; Ravazzoli and Gómez, 2014).

### ***The effect of pore geometry on the AVA response***

An interesting question is whether variations in rock fabric will display any significant effect on the AVA response. Liu et al. (2015) evaluated the effect of pore geometry on the AVA response of carbonate rocks. They suggest that the variation of amplitude is not only depending on the pore fluid or porosity, but also on the pore shape. Comparing the AVA responses at the top of the initial CO<sub>2</sub> saturated reservoir (red circle) and the CO<sub>2</sub> reservoir holding increased crack porosity reveal differences (Figures 6.18 and 6.19). Where the scenario only including the fluid effect displays a significantly less positive gradient compared to the brine saturated reservoir, the scenario including dissolution effects displays a much smaller gradient reduction. This reveals that a smaller AVA variation in the initial CO<sub>2</sub> reservoir is expected compared to the CO<sub>2</sub> bearing *and* crack dominated reservoir. As a result, the effect of including pore geometry alterations will induce a different result compared to the scenario only including the fluid effects. These variations in AVA response can be a possible source of misinterpretations if not accounted for.

### ***The effect of pore volume on the AVA response***

The effect of increased porosity on the AVA properties in the top reservoir (red circle) is displayed in Figures 6.31b and 6.32b. Following porosity increments in the CO<sub>2</sub> saturated reservoir, the gradient is more positive compared to the initial brine saturated rock. This effect is opposite of is that predicted evaluating only the fluid effects, where the gradient is reduced compared to the brine saturated reservoir. Consequently, by including the effect of fabric alterations, the fluid effect is different from the predicted Gassmann results.

The effect of reduced porosity on the AVA gradient is displayed in Figure 6.45b. Following porosity reductions in the top of the CO<sub>2</sub> saturated reservoir, the gradient displays a negative value. The AVA response of the top reservoir now categorize as class 2 (negative) or 3 responses, where the amplitudes will increase in negativity at increasing angles (Castagna and Swan, 1997). This effect is opposite of what predicted from fluid substitution of CO<sub>2</sub>, where the negative amplitude is reduced at increasing angle (class 4). The scenario including porosity reductions is the only scenario that generates a shift in AVA classes.

Nevertheless, using the porosity as an AVA parameter can be tricky, as the AVA response is controlled by the cause of the porosity change (Avseth et al., 2005). It is therefore difficult to establish a general relationship between porosity and AVA gradient and intercept.

By performing AVA modelling for various fabric scenarios, an obvious effect of pore geometry and pore volume is revealed. By comparing the synthetic gathers generated for each

scenario, the discussed observations are highlighted as the synthetic gathers display clear differences. The observations made, underline the potential value of performing forward AVA modeling, evaluating the effect of various fabric alterations.

### *The effect of compaction on the AVA response*

To evaluate the consequences of increasing pore-pressure on gradient and intercept values, the effect presented in scenario 3 is discussed. This scenario does not include any pore geometry alterations, as the pore geometry is assumed to be relatively stiff (dominated by spherical pores). Increased pore-pressure yields very little variation in AVA properties compared to the normal pressured rock (Figures 6.44c and 6.45c). Vuggy pores creates a relatively stiff rock frame, and increased pore-pressure will therefore display little effect on either gradient or intercept value (Ma and Morozov, 2010). Only small variations in gradient and intercept are observed as a response to increasing pore-pressure in the weaker rock frames. Similar studies, performed in carbonate reservoirs reveals that the pore-pressure should demonstrate some effect on the AVA gradient, but negligible effects on the intercept value (Ivanova et al., 2013).

The lacking AVA effect from increased pore-pressure presented in this study might be connected to the small effect pore-pressure displays on the velocity ratio in these models, as this parameter is related to the gradient (Castagna and Chopra, 2014). The results demonstrate that it can be challenging to distinguish between effects caused by increased pore-pressure through evaluations of the AVA response.

## **7.5 Wavelet Effect on Synthetic Seismic Data**

The modelling showed that applying different wavelets had an effect on both the resolution and the AVA response. As expected, higher frequencies yield better resolution (Figure 6.9 and 6.10). However, a 20 Hz wavelet resulted in a polarity change in the gradient between brine and CO<sub>2</sub> saturation, that was not observed using a 40 Hz frequency (Figure 6.7 and 6.8). In addition, the higher frequencies display the strongest gradients, indicating the largest amplitude variations versus angle sensitivity. It is obvious that the frequency of the wavelet will affect the modelling results.

## 7.6 Reliability of the Results

The results presented in this thesis are synthetic. Questions regarding the reliability of the data can therefore be raised. It is important to evaluate whether the presented results are representative for similar scenarios, or whether they are restricted to this specific study.

The validity of the applied rock physics models with respect to carbonate rocks have been evaluated in chapter 5. With the given limitations and assumptions related to these models, the results may not give an accurate presentation of the seismic response of a carbonate reservoir.

Also, as the synthetic data hold fluid saturations consisting of 100% brine or CO<sub>2</sub>, the fluid effects may be larger than what a mixed saturation result would present. This follows that the observed velocity variations from fluid effects depend on the compressibility contrast between the reservoir fluids (Wang et al., 1998).

However, the general trends of the seismic properties presented in this thesis agree with experimental results (e.g. Grombacher et al., 2012; Vanorio et al., 2011; Vialle and Vanorio, 2011) and fundamental theory presented by e.g. Wang (1997). With this information in mind, it is reasonable to think that the trends of the modelled results are comparable with similar scenarios.



## 8 Conclusions

Throughout this thesis I have performed forward rock physics and seismic modelling to evaluate the effect of various fabric alterations. These alterations result from CO<sub>2</sub> injections in carbonate rocks. The question has been whether these fabric variations will contribute to additional effects in the seismic properties other than what is caused by fluid substitution. Some concluding remarks will be provided in the following section.

### 8.1 Carbonate Rocks

- Carbonate rocks hold complex pore systems that can create large variations in the seismic velocities over the same porosity. As carbonate rocks are highly chemically reactive, they are prone to fabric alterations through diagenetic processes. These alterations will induce higher complexity in carbonate rocks.

### 8.2 Pore Fluid

- Increasing the concentration of CO<sub>2</sub> will reduce the P-wave velocity and increase the S-wave velocity. Consequently, the velocity ratio is lowered.
- Substituting brine with CO<sub>2</sub> will induce alterations in the AVA properties, where the amplitude variation versus angle is reduced.

### 8.3 Pore Geometry and Porosity

- Fabric alterations caused by rock-fluid interactions display an effect on the seismic velocity. Compared to altered pore geometries, changes in the pore volume display the largest effect on the seismic properties.
- Changes in pore geometry induce the largest effect on the AVA gradient compared to changes in the pore volume.

### 8.4 Pore-Pressure and Compaction

- Increasing the pore pressure results in velocity alterations. The effects of altering the rock fabric (as a response to compaction) dominates the effect of increasing the pore-pressure.
- Increasing the pore-pressure demonstrate little effect on the AVA response of the rock.

### 8.5 The Wavelet Effect

- Comparing the two synthetic AVA gathers demonstrate that the highest frequency gives a more detailed synthetic gather. Also, the AVA variations are lower for the low-frequency response compared to the high frequency response.

### 8.6 Further Work

Throughout this thesis, various seismic effects caused by geochemically induced fabric alterations have been evaluated. However, additional topics could be investigated further. The effect of pore pressure on different pore geometries could be an interesting topic to evaluate further. Although some aspects of this topic have been evaluated, a more systematic study could be performed to generalize some of the more fundamental relationships.

The effect of dissolution was only evaluated through increased porosities or altered pore geometries. However, it could be of interest to include the effect of altered mineralogy in the rock (for example reduced concentration of carbonate minerals) and altered pore fluid (increased concentrations of carbonate minerals in the pore fluids). These factors could contribute to an overall alteration in the elastic properties of both rock and fluid.

When performing the fluid substitution modelling, the fluids were fully replaced by the other. It could be interesting to evaluate the effect of different saturations, for example a mix of brine and CO<sub>2</sub> which is a more realistic presentation of the problem. Also, the nature of the saturation model could be evaluated. In this thesis, the saturation is assumed to be patchy. Therefore, a study on how the results for a homogeneous saturation would relate to those generated here would be of interest.

The effect of the wavelet used in the modelling was briefly evaluated. However, this topic could be further investigated to evaluate whether it could be a source of error when performing AVA analysis.

Finally, comparing the modelled results to real data would certainly be an interesting topic. This could be done in order to assess the validity of the modelled results.



## 9 References

- Adam, L., Batzle, M., Brevik, I.,** 2006. Gassmann's fluid substitution and shear modulus variability in carbonates at laboratory seismic and ultrasonic frequencies. *GEOPHYSICS* 71, F173–F183.
- Afif, O., Dvorkin, J.,** 2016. Building a rock physics model for a carbonate reservoir in Saudi Arabia: Case study. SEG Tech. Program Expand. Abstr. 2016, SEG Technical Program Expanded Abstracts 3277–3281.
- Ahr, W.M.,** 2008. *Geology of Carbonate Reservoirs: The Identification, Description, and Characterization of Hydrocarbon Reservoirs in Carbonate Rocks.* Wiley, New Jersey, USA.
- Akbar, M., Vissapragada, B., Alghamdi, A.H., Allen, D., Herron, M., Carnegie, A., Dutta, D., Olesen, J.R., Chourasiya, R., Logan, D., Stief, D., Netherwood, R., Duffy Russel, S., Saxena, K.,** 2000. A Snapshot of Carbonate Reservoir Evaluation. *Oilfield Rev.*
- André, L., Audigane, P., Azaroual, M., Menjot, A.,** 2007. Numerical modeling of fluid–rock chemical interactions at the supercritical CO<sub>2</sub>–liquid interface during CO<sub>2</sub> injection into a carbonate reservoir, the Dogger aquifer (Paris Basin, France). *Energy Convers. Manag., Geologic Carbon Sequestration and Methane Hydrates Research from the TOUGH Symposium 2006* 48, 1782–1797.
- Anselmetti, F.S., Eberli, G.P.,** 1997. Sonic Velocity in Carbonate Sediments and Rocks, in Palaz, I., Marfurt, K.J., (eds) *Carbonate Seismology.* Society of Exploration Geophysicists: Geophysical developments, USA.
- Avseth, P., Johansen, T., Bakhorji, A., Mustafa, H.,** 2014. Rock-physics modeling guided by depositional and burial history in low-to-intermediate-porosity sandstones. *GEOPHYSICS* 79, D115–D121.
- Avseth, P., Mukerji, T., Mavko, G.,** 2005. *Quantitative Seismic Interpretation: Applying Rock Physics Tools to Reduce Interpretation Risk.* Cambridge University Press.
- Avseth, P., Mukerji, T., Mavko, G., Dvorkin, J.,** 2010. Rock-physics diagnostics of depositional texture, diagenetic alterations, and reservoir heterogeneity in high-porosity siliciclastic sediments and rocks — A review of selected models and suggested work flows. *GEOPHYSICS* 75, 75A31–75A47. doi:10.1190/1.3483770
- Avseth, P.A., Odegaard, E.,** 2004. Well log and seismic data analysis using rock physics templates. *First Break* 22, 37–43.
- Baechle, G., Weger, R., Eberli, G., Massaferrro, J., Sun, Y.,** 2005. Changes of shear moduli in carbonate rocks: Implications for Gassmann applicability. *Lead. Edge* 24, 507–510.
- Batzle, M.L., Wang, Z.,** 1992. Seismic properties of pore fluids. *Geophysics* 57, 1396–1408.
- Berryman, J.G.,** 1999. Origin of Gassmann's equations. *Geophysics* 64, 1627–1629.

- Berryman, J.G.**, 1992. Single-scattering approximations for coefficients in Biot's equations of poroelasticity. *J. Acoust. Soc. Am.* 91, 551–571.
- Boggs Jr., S.**, 2014. *Principles of Sedimentology and Stratigraphy*, 5th ed. Pearson Education Limited, Essex, England.
- Brown, S., Bussod, G., Hagin, P.**, 2007. AVO monitoring of CO<sub>2</sub> sequestration: A benchtop-modeling study. *Lead. Edge* 26, 1576–1583.
- Burton, E.A.**, 1998. Carbonate carbonates compensation depth, in: *Geochemistry, Encyclopedia of Earth Science*. Springer Netherlands, pp. 73–73.
- Castagna, J., Swan, H., Foster, D.**, 1998. Framework for AVO gradient and intercept interpretation. *GEOPHYSICS* 63, 948–956.
- Castagna, J.P., Chopra, S.**, 2014. AVO. *Society of Exploration Geophysicists*.
- Castagna, J.P., Swan, H.W.**, 1997. Principles of AVO crossplotting. *Lead. Edge* 16, 337–342.
- Christensen, N., Wang, H.**, 1985. The Influence of pore pressure and confining pressure on dynamic elastic properties of Berea sandstone. *GEOPHYSICS* 50, 207–213.
- Dercourt, J., Paquet, J.**, 1985. Sedimentary Facies, in: *Geology Principles & Methods*. Springer Netherlands, pp. 195–206.
- Dvorkin, J., Nur, A.**, 2000. *Critical Porosity Models*.
- Dvorkin, J., Nur, A.**, 1996. Elasticity of high-porosity sandstones: Theory for two North Sea data sets. *GEOPHYSICS* 61, 1363–1370.
- Freund, P., Bachu, S., Simbeck, D., Thambimuthu, K., Gupta, M.**, 2003. Annex 1: Properties of CO<sub>2</sub> and carbon-based fuels. IPCC 385–398.
- Gassmann, F.**, 1951. Elastic waves through a packing of spheres. *GEOPHYSICS* 16, 673–685.
- Gelfand, V., Ng, P., Nguyen, H., Larner, K.**, 1988. Seismic Lithologic Modelling of Amplitude-Versus-Offset Data. *Explor. Geophys.* 19, 274–276.
- Gelius, L.-J., Johansen, T.A.**, 2012. *Petroleum Geophysics*, 2nd ed. UniGEO, Bergen.
- Grombacher, D., Vanorio, T., Ebert, Y.**, 2012. Time-lapse acoustic, transport, and NMR measurements to characterize microstructural changes of carbonate rocks during injection of CO<sub>2</sub>-rich water. *GEOPHYSICS* 77, WA169-WA179.
- Guéguen, Y., Palciauskas, V.**, 1994. *Introduction to The Physics of Rocks*. Princeton University Press, New Jersey.
- Guéguen, Y., Sarout, J., Fortin, J., Schubnel, A.**, 2009. Cracks in porous rocks: Tiny defects, strong effects. *Lead. Edge* 28, 40–47.

- Gunter, W.D., Wiwehar, B., Perkins, E.H.,** 1997. Aquifer disposal of CO<sub>2</sub>-rich greenhouse gases: Extension of the time scale of experiment for CO<sub>2</sub>-sequestering reactions by geochemical modelling. *Mineral. Petrol.* 59, 121–140.
- Harper, M.L.,** 1971. Approximate Geothermal Gradients in the North Sea Basin. *Nature* 230, 235–236.
- IEA,** 2016. World Energy Outlook 2016 (Executive summary).
- Ivanova, A., Bergmann, P., Kummerow, J., Yang, C., Lüth, S., Juhlin, C.,** 2013. Seismic Modeling of the AVO/AVA Response to CO<sub>2</sub> Injection at the Ketzin Site, Germany. *Energy Procedia, European Geosciences Union General Assembly 2013, EGUDivision Energy, Resources & the Environment, ERE 40,* 490–498.
- Japsen, P., Bruun, A., Fabricius, I.L., Rasmussen, R., Vejbæk, O.V., Pedersen, J.M., Mavko, G., Mogensen, C., Høier, C.,** 2004. Influence of porosity and pore fluid on acoustic properties of chalk: AVO response from oil, South Arne Field, North Sea. *Pet. Geosci.* 10, 319–330.
- Kearey, P., Brooks, M., Hill, I.,** 2002. *An Introduction to Geophysical Exploration*, 3rd ed. Blackwell Science, Oxford.
- Kumar, M., Han, D.,** 2005. Pore Shape Effect On Elastic Properties of Carbonate Rocks. Presented at the 2005 SEG Annual Meeting, Society of Exploration Geophysicists.
- Lacis, A.A., Schmidt, G.A., Rind, D., Ruedy, R.A.,** 2010. Atmospheric CO<sub>2</sub>: Principal Control Knob Governing Earth's Temperature. *Science* 330, 356–359.
- Li, Y., Downton, J., Goodway, B.,** 2003. Recent applications of AVO to carbonate reservoirs in the Western Canadian Sedimentary Basin. *Lead. Edge* 22, 670–674.
- Liu, W., Cao, S., Cui, Z.,** 2015. The effect of pore shape on the AVO response, in: *SEG Technical Program Expanded Abstracts 2015, SEG Technical Program Expanded Abstracts.* Society of Exploration Geophysicists, pp. 3197–3201.
- Lumley, D.,** 2010. 4D seismic monitoring of CO<sub>2</sub> sequestration. *Lead. Edge* 29, 150–155.
- Luquot, L., Gouze, P.,** 2009. Experimental determination of porosity and permeability changes induced by injection of CO<sub>2</sub> into carbonate rocks. *Chem. Geol., CO<sub>2</sub> geological storage: Integrating geochemical, hydrodynamical, mechanical and biological processes from the pore to the reservoir scale* 265, 148–159.
- Ma, J., Morozov, I.,** 2010. AVO modelling of pressure-saturation effects in Weyburn CO<sub>2</sub> sequestration. *Lead. Edge*.
- Mavko, G., Mukerji, T., Dvorkin, J.,** 2009. *The Rock Physics Handbook : Tools for Seismic Analysis of Porous Media, Second Edition.* ed. Cambridge University Press, New York, USA.
- Mavko, G., Vanorio, T., Benson, S., Luttge, A., Arvidson, R.,** 2015. Linking the Chemical and Physical Effects of CO<sub>2</sub> Injection to Geophysical Parameters.

- McCrank, J., Lawton, D.,** 2009. Seismic characterization of a CO<sub>2</sub> flood in the Ardley coals, Alberta, Canada. *Lead. Edge* 28, 820–825.
- Metz, B., Davidson, O., de Coninck, H., Loos, M., Meyer, L.,** 2005. IPCC Special Report on Carbon Dioxide Capture and Storage.
- Moore, C.H.,** 2001. Carbonate Reservoirs: Porosity, Evolution and Diagenesis in a Sequence Stratigraphic Framework. Elsevier, Oxford, UK.
- Nogues, J.P., Fitts, J.P., Celia, M.A., Peters, C.A.,** 2013. Permeability evolution due to dissolution and precipitation of carbonates using reactive transport modeling in pore networks. *Water Resour. Res.* 49, 6006–6021.
- Nordbotten, J.M., Celia, M.A., Bachu, S.,** 2005. Injection and Storage of CO<sub>2</sub> in Deep Saline Aquifers: Analytical Solution for CO<sub>2</sub> Plume Evolution During Injection. *Transp. Porous Media* 58, 339–360.
- Oldenburg, C.M., Rinaldi, A.P.,** 2011. Buoyancy Effects on Upward Brine Displacement Caused by CO<sub>2</sub> Injection. *Transp. Porous Media* 87, 525–540.
- Palaz, I., Marfurt, K.J.,** 1997. Carbonate Seismology: An Overview, in Palaz, I., Marfurt, K.J., (eds) Carbonate Seismology, Geophysical developments series; no 6. Society of Exploration Geophysicists: Geophysical developments, USA.
- Pan, J., Wang, H., Li, C., Zhao, J.,** 2015. Effect of pore structure on seismic rock-physics characteristics of dense carbonates. *Appl. Geophys.* Dordr. 12, 1–10.
- Pruess, K.,** 2004. Numerical Simulation of CO<sub>2</sub> Leakage From a Geologic Disposal Reservoir, Including Transitions From Super- to Subcritical Conditions, and Boiling of Liquid CO<sub>2</sub>. *SPE J.* 9, 237–248.
- Ravazzoli, C.L., Gómez, J.L.,** 2014. Seismic Reflectivity in Carbon Dioxide Accumulations: A Review.
- Rayner-Canham, G., Overton, T.,** 2010. Descriptive Inorganic Chemistry, 5th ed. W.H. Freeman and Company, New York, USA.
- Rossebø, Ø.H., Brevik, I., Ahmadi, G.R., Adam, L.,** 2005. Modeling of Acoustic Properties In Carbonate Rocks. Presented at the 2005 SEG Annual Meeting, Society of Exploration Geophysicists.
- Russel, B.H., Smith, T.,** 2007. The relationship between dry rock bulk modulus and porosity. *CREWES Res. Rep.* 19, 1–14.
- Rutherford, S.R., Williams, R.H.,** 1989. Amplitude-versus-offset variations in gas sands. *Geophysics* 54, 680–688.
- Siggins, A.F., Dewhurst, D.N.,** 2003. Saturation, pore pressure and effective stress from sandstone acoustic properties. *Geophys. Res. Lett.* 30, 1089.

- Smith, T.M., Sondergeld, C.H., Rai, C.S., 2003.** Gassmann fluid substitutions: A tutorial. *Geophysics* 68, 430–440.
- Sørnes, A., Brevik, I., 2000.** Fluid substitution in carbonate rocks: Scattering vs Gassmann theory, in: *SEG Technical Program Expanded Abstracts 2000*, SEG Technical Program Expanded Abstracts. Society of Exploration Geophysicists, pp. 1907–1910.
- Span, R., Wagner, W., 1996.** A New Equation of State for Carbon Dioxide Covering the Fluid Region from the Triple-Point Temperature to 1100 K at Pressures up to 800 Mpa. *J. Phys. Chem. Ref. Data* 25.
- Tatham, R.H., 1982.**  $V_p/V_s$  and lithology. *GEOPHYSICS* 47, 336–344.
- Thomas Hantschel, Kauerauf, A.I., 2009. *Fundamentals of Basin and Petroleum Systems Modeling*. Springer, Berlin.
- Tucker, M.E., Wright, V.P., 2009.** *Carbonate Sedimentology (1)*. Wiley-Blackwell, Hoboken, GB.
- Vanorio, T., 2015.** Recent advances in time-lapse, laboratory rock physics for the characterization and monitoring of fluid-rock interactions. *Geophysics* 80, WA49-WA59.
- Vanorio, T., Nur, A., Ebert, Y., 2011.** Rock physics analysis and time-lapse rock imaging of geochemical effects due to the injection of CO<sub>2</sub> into reservoir rocks. *Geophysics* 76, O23–O33.
- Vanorio, T., Scotellaro, C., Mavko, G., 2008.** The effect of chemical and physical processes on the acoustic properties of carbonate rocks. *Lead. Edge* 27, 1040–1048.
- Vega, S., Berteussen, K., Sun, Y., Sultan, A., 2007.** Is Gassmann the best model for fluid substitution in heterogeneous carbonates?, in: *SEG Technical Program Expanded Abstracts 2007*, SEG Technical Program Expanded Abstracts. Society of Exploration Geophysicists, pp. 1575–1578.
- Vialle, S., Vanorio, T., 2011.** Laboratory measurements of elastic properties of carbonate rocks during injection of reactive CO<sub>2</sub>-saturated water. *Geophys. Res. Lett.* 38, L01302.
- Walls, J., Dvorkin, J., 2005.** Effects of pore fluid properties at high pressure and temperature on seismic response.
- Wang, Z., 2001.** Fundamentals of seismic rock physics. *GEOPHYSICS* 66, 398–412.
- Wang, Z., 1997.** Seismic Properties of Carbonate rocks, in Palaz, I., Marfurt, K.J., (eds) *Carbonate Seismology*. Society of Exploration Geophysicists: Geophysical developments.
- Wang, Z., Cates, M., Langan, R., 1998.** Seismic monitoring of a CO<sub>2</sub> flood in a carbonate reservoir: A rock physics study. *GEOPHYSICS* 63, 1604–1617.
- Wilkins, R., Simmons, G., Caruso, L., 1984.** The ratio  $V_p/V_s$  as a discriminant of composition for siliceous limestones. *GEOPHYSICS* 49, 1850–1860.

**Wilson, J.L.**, 1997. Carbonate Depositional Environments and Diagenesis, in Palaz, I., Marfurt, K.J., (eds) Carbonate Seismology, 6th ed. Society of Exploration Geophysicists: Geophysical developments.

**Wilson, J.L.**, 1975. Carbonate Facies in Geologic History. Springer-Verlag, Berlin.

**Xu, S., Payne, M.**, 2009. Modeling elastic properties in carbonate rocks. Lead. Edge 28, 66–74.

**Zhang, C., Dehoff, K., Hess, N., Oostrom, M., Wietsma, T.W., Valocchi, A.J., Fouke, B.W., Werth, C.J.**, 2010. Pore-Scale Study of Transverse Mixing Induced CaCO<sub>3</sub> Precipitation and Permeability Reduction in a Model Subsurface Sedimentary System. Environ. Sci. Technol. 44, 7833–7838.

## Appendix A

### DEM: definition of $P^*$ and $Q^*$

Inclusion shape	$P^*$	$Q^*$
Spheres	$\frac{K_m + \frac{4\mu_m}{3}}{K_i + \frac{4\mu_m}{3}}$	$\frac{\mu_m + \zeta_m}{\mu_i + \zeta_m}$
Needles	$\frac{K_m + \mu_m + \frac{\mu_i}{3}}{K_i + \mu_m + \frac{\mu_i}{3}}$	$\frac{1}{5} \left( \frac{4\mu_m}{\mu_m + \mu_i} + 2 \frac{\mu_m + \gamma_m}{\mu_i + \gamma_m} + \frac{K_i + \frac{4\mu_m}{3}}{K_i + \mu_m + \frac{\mu_i}{3}} \right)$
Disks	$\frac{K_m + \frac{4\mu_i}{3}}{K_i + \frac{4\mu_i}{3}}$	$\frac{\mu_m + \zeta_i}{\mu_i + \zeta_i}$
Penny cracks	$\frac{K_m + \frac{4\mu_i}{3}}{K_i + \frac{4\mu_i}{3} + \pi\alpha\beta_m}$	$\frac{1}{5} \left[ 1 + \frac{8\mu_m}{4\mu_i + \pi\alpha(\mu_m + 2\beta_m)} + 2 \frac{K_i + \frac{2}{3}(\mu_i + \mu_m)}{K_i + \frac{4\mu_i}{3} + \pi\alpha\beta_m} \right]$

**Table A1.** Defining  $P^*$  and  $Q^*$  for various pore shapes. Modified from Mavko et al. (2009). The subscripts  $m$  and  $i$  refer to the background and inclusion material respectively. The shear modulus is defined as  $\mu$  and  $K$  is the bulk modulus. Also  $\beta = \frac{3K+\mu}{3K+4\mu}$ ,  $\gamma = \mu \frac{3K+\mu}{3K+7\mu}$ ,  $\zeta = \frac{\mu(9K+8\mu)}{6(K+2\mu)}$  and  $\alpha$  is the aspect ratio.

### CCT: definition of $S_n$ and $S_\tau$

Normal grain contact stiffness  $S_n$  (Mavko et al., 2009):

$$S_n = A_n b^2 + B_n b + C_n,$$

$$A_n = -0.024153 \Lambda_n^{-1.3646},$$

$$B_n = 0.020405\Lambda_n^{-0.89008},$$

$$C_n = 0.00024649\Lambda_n^{-1.9864},$$

$$\Lambda_n = \frac{2\mu_c(1-v_s)(1-v_c)}{\pi\mu_s(1-2v_c)},$$

where  $v_c$  is the Poisson's ratio of the cement and grains respectively,  $\mu_s$  is the shear modulus of the grains and  $\mu_c$  is the shear modulus of the cement.

The amount of cement is described by the parameter  $b$ . When the contact cement is pore filling and located at the pore contacts only, then

$$b = 2 \left[ \frac{S_c \phi_0}{3C_0(1-\phi_0)} \right]^{0.25},$$

where  $S_c$  is the total volume of pore space cement,  $\phi_0$  the critical porosity and  $C_0$  is the coordination number .

When the cement is pore filling and located all around the pore wall, but not making a cement to cement contact at the grain interface, then

$$b = \left[ \frac{2S_c \phi_0}{3(1-\phi_0)} \right]^{0.50}.$$

Tangential contact grain stiffness  $S_n$  (Gelius and Johansen, 2012):

$$S_\tau = A_\tau b^2 + B_\tau b + C_\tau,$$

$$A_\tau = -10^{-2}(2.26v_s^2 + 2.07v_s + 2.3)\Lambda_\tau^{0.079v_s^2+0.175v_s-1.342},$$

$$B_\tau = (0.0573v_s^2 + 0.0937v_s + 0.202)\Lambda_\tau^{0.01867v_s^2+0.0529v_s-0.8765},$$

$$C_\tau = -10^{-4}(9.654v_s^2 + 4.945v_s + 3.1)\Lambda_\tau^{0.01867v_s^2+0.4011v_s-1.8186},$$

$$\Lambda_n = \frac{\mu_c}{\pi S},$$